Exploring Flow Characteristics and Geometry of Heavy ion Collisions using Simulation Models and Machine Learning

To be submitted in the partial fulfilment for the degree of
DOCTOR OF PHILOSOPHY IN PHYSICS

BY

ABHISEK SAHA
17PHPH12

Under the supervision of
Dr. SOMA SANYAL

School of Physics
University of Hyderabad
Hyderabad 500 046, INDIA

March 2023

DECLARATION

I hereby declare that, this thesis titled **Exploring Flow Characteristics and Geometry of Heavy ion Collisions using Simulation Models and Machine Learning** submitted by me, under the guidance and supervision of **Dr. Soma Sanyal**, is a bonafide research work and is free from plagiarism. I also declare that it has not been submitted previously, in part or in full to this University or any other University or Institution, for the award of any degree or diploma. I hereby agree that my thesis can be deposited in Shodhganga/INFLIBNET.

A report on plagiarism statistics from the University Librarian is enclosed.

Abhisek Saha

Hyderabad
Date: 10/03/2023

(Abhisek Saha)
Reg. No.: 17PHPH12

CERTIFICATE

This is to certify that the thesis entitled **Exploring Flow Characteristics and Geometry of Heavy ion Collisions using Simulation Models and Machine Learning** submitted by Abhisek Saha bearing registration number 17PHPH12 in partial fulfilment of the requirements for award of Doctor of Philosophy in the School of Physics is a bonafide work carried out by him under my supervision and guidance.

This thesis is free from plagiarism and has not been submitted previously in part or in full to this or any other University or Institution for award of any degree or diploma.

Further, the student has the following publications before the submission of the thesis for adjudication.

1) Abhisek Saha and Soma Sanyal, International Journal of Modern Physics E **29**, 01, 2050001 (2020), (ISSN No: 1793-6608 (online)), Chapter 2.

2) Abhisek Saha and Soma Sanyal, The European Physical Journal Plus **137**, 1074 (2022), (ISSN No: 2190-5444 (online)), Chapter 3.

3) Abhisek Saha and Soma Sanyal, Modern Physics Letters A **36**, 22, 2150152 (2021), (ISSN No: 1793-6632 (online)), Chapter 4.

4) Abhisek Saha, Debasis Dan and Soma Sanyal, Physical Review C **106**, 014901 (2022), (ISSN No. 2469-9993 (online)), Chapter 5.

Further, the student has passed the following courses towards fulfilment of coursework requirement for Ph.D:

Course Code	Name	Credits	Pass/Fail
PY801	Research Methodology	4	Pass
PY802	Advanced Quantum Mechanics	4	Pass
PY803	Advanced Experimental Techniques	4	Pass
PY804	Advanced Condensed Matter Physics	4	Pass

Dr. Soma Sanyal
Thesis Supervisor
School of Physics
University of Hyderabad

Date: 10.3.2023.

Dr. SOMA SANYAL
Associate Professor
School of Physics
University of Hyderabad
Hyderabad-500046, India.

10-3-2023

Prof. James Raju K.C.
Dean
School of Physics
University of Hyderabad

DEAN
School of Physics
University of Hyderabad
HYDERABAD - 500 046

Acknowledgements

It is an incredible journey of learning and exploration that has been not only a challenge but also a pleasure. As much as I am proud to have completed my Ph.D. thesis, it would not have been possible without the help and support of many people.

First and foremost, I would like to express my utmost gratitude to my supervisor, Dr. Soma Sanyal, for her guidance, support, and encouragement throughout my Ph.D. journey. She has been an invaluable source of support, expertise, guidance, and encouragement throughout this journey. She not only provided me with invaluable advice and resources but also believed in me and my research, which allowed me to remain focused and motivated. I was uncertain about my capabilities when I started the Ph.D. My advisor recognized my potential right from the beginning. She helped me understand how I could improve and learn new skills. She always encouraged me to present our research work at various national and international conferences so that I could improve my presentation and communication skills. I feel that obtaining a Ph.D. is not a straightforward journey and that each student builds their own path. There were times during these five years when I felt completely lost and could not come up with anything for months. I always found my supervisor beside me in all these situations. She consistently reminded me of my potential and continued to believe in me even when things were not going well. She has been an incredible mentor and has always been available to answer my questions and provide guidance. Her enthusiasm for my research and continued support have been instrumental in my success. I am deeply thankful for her support and willingness to help me achieve my goals.

I thank my doctoral committee members, Prof. Rukmani Mohanta and Dr. Barilang Mawlong, for their fruitful suggestions during the meetings. I thank Prof. E.Harikumar for all his suggestions. I also want to thank you all for the guidance and mentorship you have provided me during my time as a student at the School of Physics. I acknowledge Dr. Soma Sanyal, Prof. Rukmani Mohanta, and Prof. E.Harikumar for the time and effort that you invested in crafting all the insightful recommendation letters for my postdoc applications. I also thank other high-energy physics faculty members, Prof. Bindu A. Bambah and Prof. P.K. Suresh, for their encouragement.

I thank the Dean School of Physics, Prof. K. C. James Raju, and former deans Prof. Ashok Chatterjee, Prof. Seshu Bai. V and Prof. Bindu A. Bambah for their cooperation and for providing me with all the facilities. I express my thanks to Prof. G.

Vaitheeswaran for guiding me and encouraging me. I'd also like to thank all the other faculties and the non-teaching staff of the School of Physics for their assistance and support.

I have received great support from all the non-teaching staff of our school and also from some administration staff of HCU. I thank Sashikala Ma'am, Sudarshan Sir, Deepika Ma'am, Shailaja Ma'am, Narshima Sir, and Mr. Mahesh from the School of Physics, who have helped me on several occasions. I am thankful to Mr. Sainath Sir and Madhvi Ma'am for helping me process my fellowship.

I must also express my deepest gratitude to my parents for their unwavering support and faith in me. I can not forget my father traveled with me to Kolkata at least ten times when I started college, which was 700 km away from our home. I don't know whether anyone else has done this for their child or if it was feasible for any other father to leave all his work behind. My father has rarely been unable to accompany me to the train station or airport. He says that the time we spend together while traveling is very valuable. I consider myself really blessed to have parents like them. They always tried to keep me stay stress-free and not feel too pressured, which was especially difficult during this point in my life when everyone expected me to take on a lot of responsibilities. They have always been willing to help me in any way they can and have given me the freedom to pursue my dreams. My journey would not have been possible without their help.

I would also like to thank my sister, Puja, for being my rock and my sounding board throughout this entire process. She has always been there to listen, encourage, and offer advice. I am truly grateful for her unconditional love and support.

I come from a large joint family in which all my cousins grew up together, and their influence on my life has been enormous. I want to express my love to my two cousin sisters, Tonki and Megha. I don't know how to repay them for their unconditional love and respect. They are an integral part of my life and will always remain so. I want to thank my cousin brother, Jeet, as well. I have known for a long time how talented he is. He always idolizes me for his success, which has inspired me to do better, stay motivated, and set a good example. I am also grateful to my other family members who have supported me throughout this journey.

I'd like to thank my girlfriend, Pritha, for being an integral part of my journey. Thank you for being a part of my happiness, sadness, success, failure, and everything in between.

I want to thank all my friends who have been a part of my journey in some way or another. They have offered me love and encouragement and have been a source of strength and inspiration. Although it's not always possible to talk about everyone's contribution, I will still try to mention some. Suman, Sovan, Susmita, and Soumen, you all have been my backbone throughout. I can't really tell how much time we've spent together in the last five years or how many difficulties we've shared and solved. Whenever I have faced difficult times or felt low, I have come to you, and you have supported me, given me advice, and cheered me up every time. It would be inappropriate for me to quantify how much help and support I have got from all of you. All I want is the bond I share with each of you to remain unbreakable and eternal. Nurul, Mitesh, and Debika, we started this journey together. I received various kinds of help from you at different stages of the journey. Sovan and Nurul, I cannot forget how much you helped me when I was admitted to the health center. I want to express my heartfelt gratitude to all of you. There are many more people whom I have had by my side throughout the years, including Dilip, Vishnu, Samir, Supratik, Subhasree, Dipanjan, Somnath, Dinesh, Priya, Papia, Mainur, Devaparna, Abinash, Rudra, Akshay, Aishwarya, Debomita. Mitesh and Priya have helped me a lot in searching for postdoc applications. I am grateful to all of them for their support and presence in my life. I also want to thank my seniors, Soutrick Das, Avisek Das, Manojit Ghosh, Subham Debnath, and Kuntal Bhattacharya, who has provided me with a lot of help and advice.

I want to thank all of my collaborators who were involved with my work and with whom I have had extensive discussions regarding the research. I thank Dr. Debasis Dan for your valuable input in our machine learning paper. I'd like to Dr. Sidharth Kumar Prasad, Abhi Modak, Debjani Banerjee, and Prottoy Das for teaching me about PMD detector and jet physics-related work and for all the hospitality you provided to me during my stay at the Bose Institute. I also thank Prof. Tapan Nayak for all the discussions and advice. I thank Dr. Partha Pratim Bhaduri for your encouragement and willingness to help me. I also want to thank Dr. Chitrasen Jena for all your help and encouragement.

I acknowledge the Department of Science and Technology, Government of India, for providing me with financial support through the INSPIRE fellowship. I also acknowledge the Institute of Eminence, University of Hyderabad, for providing financial support. I would like to acknowledge the Center for Modelling, Simulation and Design (CMSD) at the University of Hyderabad for providing computational infrastructure.

Finally, I would like to thank everyone who has helped me along the journey, from those who have offered advice and assistance to those who have taken the time to read and review my work. Your contributions have been invaluable, and I am sincerely grateful for all of your assistance and support.

In conclusion, I would like to thank everyone who has made this journey possible. I am deeply humbled and appreciative of all the support and guidance I have received. I am truly fortunate to have so many wonderful people in my life. Thank you.

Dedicated to my parents

Abstract

We know from the time-temperature history of the universe, at times 10 microseconds after the Big Bang, with temperature $T \geq 200$ MeV, the universe was in the state of Quark Gluon Plasma (QGP). QGP is a state of matter where elementary colored particles(e.g., quarks and gluons) that make up the hadronic matter are deconfined and can move freely over nuclear distances under extremely high densities and temperatures. The study of the QGP is important because it can provide insights into the fundamental nature of matter and the strong nuclear force. In the modern era, we try to recreate this state of matter in the laboratory for a short period of time by colliding two relativistic heavy ions in heavy-ion colliders, namely the Relativistic Heavy-Ion Collider (RHIC) at the Brookhaven National Laboratory and the Large Hadron Collider (LHC) at CERN. Several theories are developed to describe the QCD phase diagram, which represents the phase transition from confined and color singlet hadron state to the deconfined QGP state, namely the QCD phase transition. The lattice QCD predictions show a crossover transition around $T \approx 150 - 170$ MeV for an infinitesimal value of μ_B. There are models which indicate a first-order phase transition at finite μ_B with different transition temperatures. The first-order transition line meets the crossover region at the critical point whose existence is not established experimentally. As the exact boundaries separating the two phases are unknown, these experiments play a vital role in describing the QCD phase diagram. The SPS and ongoing BES(Beam Energy Scan) program at RHIC, as well as the lower-energy facilities, namely Facility for Antiproton and Ion Research (FAIR) at GSI and Nuclotron-based Ion Collider fAcility (NICA) at JINR, are developed to map out the QCD phase diagram at finite μ_B.

The study of the rotational properties of the QGP system is important for understanding the fundamental nature of the QGP. One of the key properties of interest is the vorticity of the QGP. The study of vorticity in heavy ion collisions has gained significant attention in recent years, as it is believed to play a crucial role in the generation of the observed spin polarization. The vorticity of the QGP can also provide insights into the QGP's transport properties, such as its viscosity and thermal conductivity. Vorticity can affect the collective flow of particles in the QGP and can also induce magnetic fields.

We study the vorticity patterns in relativistic heavy ion collisions with respect to the collision energy. The collision energy is related to the chemical potential used in the thermal-statistical models that assume approximate chemical equilibrium after the relativistic collision. We use the multiphase transport model (AMPT) to study the vorticity in the initial parton phase as well as the final hadronic phase of the relativistic heavy ion

collision. Our results indicate that the viscosity plays a greater role at higher chemical potential and lower collision energies.

Fluctuation studies play a crucial role in the search for the QCD critical point. Fluctuations in conserved quantities, such as net baryon number, net strangeness, and net charge, are sensitive probes of the QGP's properties. The theory predicts that fluctuations in these conserved quantities will be enhanced at the QCD critical point due to the long-range correlations that develop in the system. Therefore, fluctuation studies are important in heavy ion collision experiments to obtain information about the QGP's properties and to search for the QCD critical point.

We study temperature fluctuations in the initial stages of the relativistic heavy ion collision using the AMPT model. We use the non-extensive Tsallis statistics to find the entropic index in the partonic stages of the relativistic heavy ion collisions. We find that the temperature and the entropic index have a linear relationship during the partonic stages of the heavy ion collision. We performed a detailed analysis of the dependence of the entropic index on the system parameters and compared it with the entropic index obtained from the fitting of transverse momentum spectra.

Signs of turbulence have been observed at the relativistic heavy-ion collision at high collision energies. We study the signatures of turbulence in this system and find that there are significant departures from isotropic turbulence in the initial and the pre-equilibrium stages of the collision. The geometrical anisotropy is reflected in the anisotropic turbulence generated in the rotating plasma, and we find that the scaling exponent is different in the two planes. We also obtain the temperature spectrum in the pre-equilibrium stages. The spectrum deviates from the Gaussian spectra expected for isotropic turbulence.

We use supervised Machine Learning (ML) models to predict three important properties that determine the initial geometry of the heavy-ion collision (HIC) experiments. These properties are the impact parameter, the eccentricity, and the participant eccentricity. We study multiple ML algorithms, their error spectrum, and sampling methods using exhaustive parameter scans and ablation studies to determine a combination of efficient algorithms and tuned training set that gives a multi-fold improvement in accuracy for three different heavy-ion collision models. The three models chosen are a transport model, a hydrodynamic model, and a hybrid model. The motivation for using three different heavy-ion collision models was to show that even if the model is trained using a transport model, it gives accurate results for a hydrodynamic model as well as a hybrid model. We also show how sampling techniques can improve the accuracy of impact parameter and eccentricity prediction.

Contents

List of Figures

List of Tables

Chapter 1

Introduction

Heavy ion collisions (HIC) are an essential approach for studying the characteristics of the quark-gluon plasma (QGP), a deconfined state of matter that interacts strongly and is believed to be created in such collisions. In these experiments, two heavy ions (atoms with more than one proton and neutron) are accelerated to very high energies and they are made to collide. These collisions cause the particles within the ions such as quarks and gluons, to interact with each other and create new particles. This allows us to study the behavior of subatomic particles and the interactions between them. These experiments are important for understanding the fundamental nature of matter and energy, as well as the nature of our universe. The QGP exists in extreme conditions of high temperatures and densities. Thus, these experiments allow us to study how matter behaves in extreme conditions. They also provide us with data that can be used to understand the dynamics of the strong nuclear force, which governs the interactions between particles in the nucleus. This also helps us understand the QCD phase transition. Additionally, as the QGP state is believed to be present in the early universe, these experiments help us understand the behavior of matter in conditions that cannot be recreated in a laboratory, such as the initial stages of the universe.

The collision energy and species of the colliding ions specify the system's initial state, while the properties of the particles created by the collision determine the system's final state. In these experiments, several initial state and final state variables or observables are essential for understanding the dynamics of the system. We study several flow-related characteristics of the QGP system at different phases of system evolution. Flow is the collective motion of the particles produced in collisions, and it is one of the major observable to study the QGP properties. Fluctuations measure the deviations from the average behavior of particles and can be used to learn the system dynamics and the initial

conditions. The study of fluctuation can also help us locate the critical point (CP) in the QCD phase transition diagram, as these are likely to diverge close to CP. That is why various thermodynamic properties, which depend on the fluctuations, are studied in this area of research. Vorticity is another important phenomenon related to fluid motion, and this can be used to study the characteristics of the rotating system and the collective behavior of the particles. Vorticity measures the rotation of the system produced in the collision, and its strength is used to characterize the degree of its turbulence. We also study turbulence spectra for velocity and temperature fluctuations. This helps us understand the energy deposition at different length scales and planes in the collision region. Furthermore, we use several machine-learning techniques to estimate the initial state variables of HIC experiments. Before going into the details of our study, let us start with some of the basic understanding of these experiments.

1.0.1 Units and conventions

In high-energy physics, we consider natural units of measurement that are based on physical constants. In natural units, we consider the Plank's constant and speed of light to be one, $c = \hbar = 1$. The units of electric charge are also redefined. The energy E is measured in electronvolt (eV, KeV, MeV, GeV, TeV) unit. As mass and momentum are related to E by the mass-energy relation, one can get their units.

$$E^2 = p^2c^2 + m^2c^4 \tag{1.1}$$

Thus, units of momentum is eV/c, and mass is eV/c^2. Considering $c = 1$, mass and momentum have units of energy. The mass of a proton and neutron is nearly 1 GeV. Length and time have units of 1/Energy, which can be deduced from $E = h\nu$ and from $\Delta x \Delta p \geq 1$, the uncertainty principle. The radius of a proton or neutron is approximately 1 fm= $10^{-15}m \approx 1/(200\ MeV)$. The temperature is also expressed in energy units ($1eV \approx 10^4 K$).

The four-dimensional space-time coordinates are used to describe the positions. This consists one time dimension t and three spatial dimensions x, y, z, and can be expressed as $x^\mu = (t, x, y, z)$, also referred as contravariant 4-vector. It can be transformed to a covariant vector $x_\mu = (t, -x, -y, -z) = (t, -r)$ by the action of a metric tensor. Here, we use the Minkowski metric tensor,

$$g_{\mu\nu} = g^{\mu\nu} = diag(1, -1, -1, -1) \tag{1.2}$$

Hence $x_\mu = g_{\mu\nu}x^\nu$

Invariant variables play a crucial role in HIC studies. This allows us to measure quantities in a frame-independent framework. It is important to work with invariant variables while working with relativistic velocities, as it allows us to understand how things behave from the perspective of different observers, i.e., under different frames of reference. The inner product of any four-vector is invariant (e.g., $x_\mu x^\mu = x^2$). The four-momentum is denoted by $p^\mu = (p^0, \mathbf{p}) = (E, \mathbf{p})$, where $\mathbf{p}$ is 3-momentum(p_x, p_y, p_z), and p^0 is the particle energy,

$$p^0 = E = \sqrt{\mathbf{p}^2 + m^2} \tag{1.3}$$

The inner product of momentum $p^\mu p_\mu = p^2 = m^2 = E^2 - \mathbf{p}^2$ is normalized to the rest mass of the particle. The 3-momentum can be segmented into two components: p_z along the beam direction (z-axis) and the transverse momentum $p_T = \sqrt{x^2 + y^2}$ which is on the plane perpendicular to the z-axis. The four velocity is defined as $u^\mu = (\gamma, -\gamma\mathbf{v})$. Here γ is the Lorentz factor $\gamma = 1/\sqrt{1 - \mathbf{v}^2}$. The four-velocity is normalized to 1: $u^\mu u_\mu = 1$. $\mathbf{v}$ is the velocity vector in 3 dimensions.

We define a new parameter known as rapidity, which is a generalization of the velocity vector. It is defined as,

$$y = arcth(v_z) = arcth(\frac{p_z}{p_0}) = \frac{1}{2}ln\frac{p_z + p_0}{p_z - p_0} \tag{1.4}$$

For small velocities it is similar to v_z, i.e., $y \approx v_z$. The reason behind using this new parameter is it is additive in nature under Lorentz transformation. As a result, under Lorentz boosts, the particle rapidity distribution is unaffected. Additionally, the difference in the two particle's rapidity is invariant under Lorentz boosts in the beam axis. However, rapidity is hard to determine in experiments; thus, a new parameter is introduced known as pseudorapidity:

$$\eta = \frac{1}{2}ln\frac{|\mathbf{p}| + p_z}{|\mathbf{p}| - p_z} = ln(cot(\frac{\theta}{2})) \tag{1.5}$$

Pseudorapidity provides an extra advantage working with relativistic velocities. As it only depends on one variable, the particle's polar angle θ, it can be measured directly in the experiments. Most particles' momentum in high-energy experiments is significantly greater than their rest mass. In that case $E \approx |\mathbf{p}|$ which means, $y \approx \eta$.

1.0.2 Elementary forces in Nature

Gravitation, electromagnetism, the weak nuclear force, and the strong nuclear force are the four fundamental forces of nature. The interactions among the elementary particles are governed by these four forces. Except for gravity, all of these interactions have a microscopic quantum formulation in the form of local gauge theories. The elementary matter fields are spin-1/2 fermions that interact through the exchange of spin-1 bosons. The Higgs spin-0 boson, the single fundamental scalar particle in the standard model, plays a specific role in this paradigm by providing all other fields with a mass proportional to their coupling to the Higgs [1]. All predictions made by the standard model have so far been validated by the 2012 finding of the Higgs boson at the Large Hadron Collider at CERN by the ATLAS, and CMS experiments [2]. The classical field theory of gravity (general relativity) has been experimentally verified with a high degree of precision. The most recent of these verifications was the observation of gravitational waves produced by the merger of massive compact objects, such as black holes or neutron stars [3]. However, a theory of quantum gravity is still a challenge.

1.0.3 The Theory of Quantum Chromodynamics

QCD was proposed by Gell-mann and Zweig in 1963. It is the theory which governs strong interactions, liable for the strong force. The EM force describes the interaction between electric charges and is called quantum electrodynamics (QED). It is mediated by a boson known as the photon. There are lots of similarities between QCD and QED. QED has two degrees of freedom, e.g., positive and negative charges, and QCD has three degrees of freedom called color charges, red, green, and blue. In QED, the overall system can be charge-neutral if there are same number of positive and negative charges. Likewise, we only get color-neutral particles in normal conditions (low temperature and density). They are known as mesons and baryons. A crucial difference between QCD and QED is confinement, due to which there are no free quarks and gluons in nature, unlike electric charges and photons. When a color charge is combined with an anticolor charge of the same type, it forms a color-neutral state. This bound state is a type of meson. A color-neutral state can also be generated if three different color charges are combined together with equal proportions, and the bound state is known as a baryon. Antimatter particles have opposite charges compared to their matter particles. The same is true for color charges. The charges for antimatter are antired, antiblue, and antigreen. The strong force is mediated by a gauge boson called the gluon. This is analogous to photons from QED with the difference that gluons carry color charge, unlike photons that are chargeless.

There are six flavors of quarks, e.g., up, down, strange, charm, bottom, and top. This is in the sequence of mass ordering, where the top quark has the highest mass. It is 175 times more massive than the proton. The up and down quarks are the lightest and most abundant. To get the correct electric charges of the mesons and the baryons, the up, down, and strange quarks are given a charge of $+2/3e$, and the down, strange and bottom quarks are given a charge of $-1/3e$.

QED belongs to the U(1) group and the photon that serves as the group's generator. With eight different types of gluons acting as generators, QCD belongs to the SU(3) group. QED is an Abelian gauge theory, and QCD is a non-Abelian gauge theory.

1.0.4 Confinement

The non-Abelian characteristic of QCD emerges physically as confinement. In QED, photons mediate forces between particles with an electric charge. Similarly, gluons in QCD transmit forces between particles with color charge. So gluon is the QCD force carrier. Gluons themselves, however, carry a color charge. Because it has no charge, the photon has no interactions with photons. This implies that the interaction between two charged particles weakens with increasing distance. The intensity drops with increasing distance r because photons spread at all angles.

$$V \propto 1/r^2 \tag{1.6}$$

In QCD, as the distance between two quarks increases, the gluons connecting them interact. As a result, a "color flux tube" is formed. Imagine the quarks are joined by intense field lines that form a string to gain a qualitative understanding of this. A color flux tube with a uniform cross-sectional area and fixed energy density are used to describe the string. This tube has the function of keeping the force between the quarks constant regardless of distance. The separation of two quarks would theoretically take an endless amount of force. In reality, though, the flux tube will split and produces a pair of quark-antiquark once it has enough energy (See the illustration in Fig. 1.1). The Cornell potential is used to analytically explain confinement. It was introduced in 1970 to account for the relationship between the hadron's mass and angular momentum as well as to explain the masses of quarkonium states [4, 5]. The potential appears as follows:

$$V_{Cornell} = -\frac{4}{3}\frac{\alpha_s}{r} + \sigma r \tag{1.7}$$

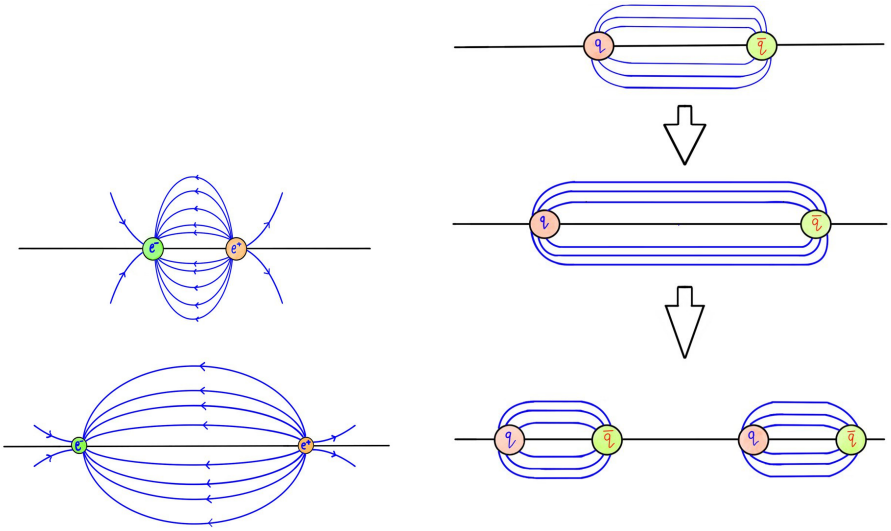

FIGURE 1.1: a) Electric field lines spread out as the electric charge separated; b) Color force lines collimated into a tube-like shape and do not spread out as the quarks are separated

where r is the separation between the quarks, σ is the string tension, and α_s is the strong coupling constant. With a varied coupling strength, the first term resembles the Coulomb potential from classical electrodynamics. The second term, which is in charge of confinement, originates from the non-Abelian portion of QCD. It can be thought of as the potential energy held within the string, which becomes larger with increasing distance due to the constant energy density. That is why, for significant quark separation, the linear part of the potential dominates, and the quarks can never go free. When the quark separation is relatively small, the Coulomb part leads, and the theory becomes essentially identical to QED.

1.0.5 Asymptotic Freedom

Analogous to QED, there is a coupling constant in QCD, which is denoted as α_s. But it is not a constant in QCD. The intensity of α_s decreases with the decrease in separation between interacting quarks. Because of the charge screening produced by the virtual particle's vacuum fluctuation, the coupling constant, α in QED, decreases with distance. This is referred to as the running coupling constant. Similar events take place in QCD; however, gluon self-interaction modifies α_s's behavior. It is also accurate to argue that the intensity of the coupling constant reduces with energy because examining the interaction at small distances demands more energy. For strong interactions, the four momentum transfer (Q^2) dependence of α_s is very strong. This is because the field

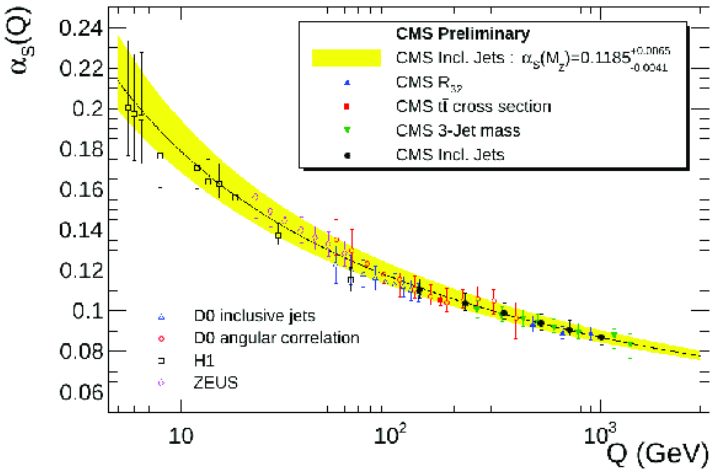

FIGURE 1.2: Strong intraction coupling constant [7]

mediator gluons themselves carry color charges and can couple with one another. At very large Q^2, a first order pQCD gives,

$$\alpha_s(Q^2) = \frac{12\pi}{(22 - 2n_f).ln(Q^2/\Lambda^2_{QCD})} \tag{1.8}$$

Here, the number of quark flavors, $n_f = 6$, and Λ_{QCD} is the scale parameter of QCD. The distance between quarks in space is expressed as $\lambda = \frac{\hbar}{\sqrt{Q^2}}$. Therefore, the inter-quark coupling weakens and asymptotically vanishes for very short distances and high values of Q^2. This is referred to as asymptotic freedom and is a perturbative-QCD prediction. Asymptotic freedom was described by Politzer, Gross, and Wilczek in 1973 (Nobel Prize 2004). The fact that QCD is non-Abelian contributes to asymptotic freedom as well. In fact, any asymptotically free renormalizable quantum field theory requires non-Abelian gauge fields [6].

1.0.6 QCD Lagrangian

Although there are similarities in the Lagrangian of QCD and QED, the QCD Lagrangian is much more complicated. It can be expressed as,

$$\mathcal{L}_{QCD} = \sum_q \left(\bar{\psi_{qi}} i\gamma^\mu \left[\delta_{ij}\partial_\mu + ig(G^\alpha_\mu t_\alpha)_{ij}\right] \psi_{qj} - m_q \bar{\psi_{qi}}\psi_{qi}\right) - \frac{1}{4} G^\alpha_{\mu\nu} G^{\mu\nu}_\alpha \tag{1.9}$$

Here $G^\alpha_{\mu\nu} = \partial_\mu G^\alpha_\nu - \partial_\nu G^\alpha_\mu - g f^{\alpha\beta\gamma} G^\beta_\mu G^\gamma_\nu$, is the color field tensor. G^μ_α is the four potential gluon field, t_α are 3×3 Gell-Mann matrices that are the generators of the SU(3) group,

$f^{\alpha\beta\gamma}$ is the structure constants of the SU(3) group (not there in QED), ψ_i is the Dirac spinor of the quark field where i represent the color charges (red, green, and blue), and $g = \sqrt{4\pi\alpha_s}$. The Gell-Mann matrices serve the same purpose in QCD as the Pauli spin matrices in QED.

A three-dimensional vector space is formed by three color states. A vector in this space represents the general color state of a quark. The 3×3 unitary matrices can rotate a color state. The Lie group SU(3) consists of all such unitary transformations with a unit determinant.

The QED Lagrangian is very similar to the QCD Lagrangian

$$\mathcal{L}_{QED} = \bar{\psi_e} i\gamma^\mu \left[\partial_\mu + ieA_\mu\right] \psi_e - m_e \bar{\psi_e} \psi_e - \frac{1}{4} F_{\mu\nu} F^{\mu\nu} \tag{1.10}$$

with $F^{\mu\nu} = \partial^\mu A^\nu - \partial^\nu A^\mu$. A crucial difference between the QED and QCD fields is that there is an additional term in the gluon field tensor $G_\alpha^{\mu\nu}$ which represents the interaction between the color-charged gluons. This is because the photons do not interact with one another.

The helicity is preserved by the QCD Lagrangian for massless quarks. In fact, the handedness or chirality of a massless quark is independent of the Lorentz frame used for the study because it moves at the speed of light. The mass term expressly breaks the chiral symmetry,

$$m_q \bar{\psi_q} \psi_q = m_q \bar{\psi_{qL}} \psi_{qR} + m_q \bar{\psi_{qR}} \psi_{qL} \tag{1.11}$$

However, the primary cause of the chiral symmetry breaking may be explained in terms of the gluon condensate and quark condensate produced by the non-perturbative action of the QCD. There is a spontaneous symmetry breaking for the QCD-vacuum state and it is realized by the non-vanishing chiral condensate,

$$\langle \bar{\psi_{qL}} \psi_{qR} \rangle \propto \Lambda_{QCD} \neq 0 \tag{1.12}$$

Effectively, in the chiral phase transition, the chirality is restored in the quark phase. It is associated with changes in the vacuum expectation values of quark condensates, which are order parameters for spontaneous chiral symmetry breaking. At high temperatures and densities, the quark condensate melts, restoring the chiral symmetries of the theory. This transition is believed to be a key feature of the QCD phase diagram.

1.0.7 The quark gluon plasma

Matter is composed of protons, neutrons, and electrons at low energy densities. The system may experience thermal excitation if it is heated. This can produce light-mass highly interacting particles like the pion. Quarks and gluons are found inside protons, neutrons, and other strongly interacting particles. If the energy density is high enough, protons, nucleons, and other particles can be compressed so tightly that they can move over a larger distance without being contained by hadrons [8]. As there is a deconfinement at these extreme conditions, the system is referred to as quark-gluon plasma. The quark-gluon interaction weakens as the energy density increases. As the strong interaction shows asymptotic freedom behavior, the interactions become weak at close ranges.

The QGP is supposed to have been formed at the Big Bang. Quantum gravity is significant when temperatures are of the order $T \sim 10^{19}$GeV. Possibly, there is a grand unification of all the forces, except for gravity, at slightly lower temperatures. At this temperature scale of universe evolution, the baryon number is believed to be produced. Electroweak symmetry breakdown occurs at $T \sim 100$ GeV, which is significantly lower. The universe's baryon imbalance might have been formed in this epoch. Hadrons are formed from quarks and gluons when the temperature is below 1 GeV (around $T \sim 200$ MeV). The collider experiments at RHIC and the LHC operate to produce matter in this temperature range. The light elements are created at $T \sim 1$ MeV. When the temperature of the universe reaches one electronvolt, it changes from an ionized gas to an atom-filled gas under lower pressure. This energy corresponds to the electron's binding energy in atoms. At this temperature, structures like stars are formed.

At energy densities of the order of 1 GeV/fm^3, the QGP is created. The cores of neutron stars likely contain matter with such energy concentrations. Neutron stars are objects with exceptionally high energy density materials with a radius of about 10 km. The energy density typically ranges from 1 GeV/fm^3 in the core to almost nothing at the surface. In contrast to the energy of the matter in the Big Bang, this matter is cold and has a very low temperature. At lower densities, it transforms into a cold gas of nucleons.

1.0.8 QCD Phase Diagram

At roughly the same energy density as the matter inside a proton, a QGP state should start to form. Given that a proton's size is approximately 1 fm and its rest mass energy is about 1 GeV, it has an energy density of around $1GeV/fm^3$. People in the late 1970s

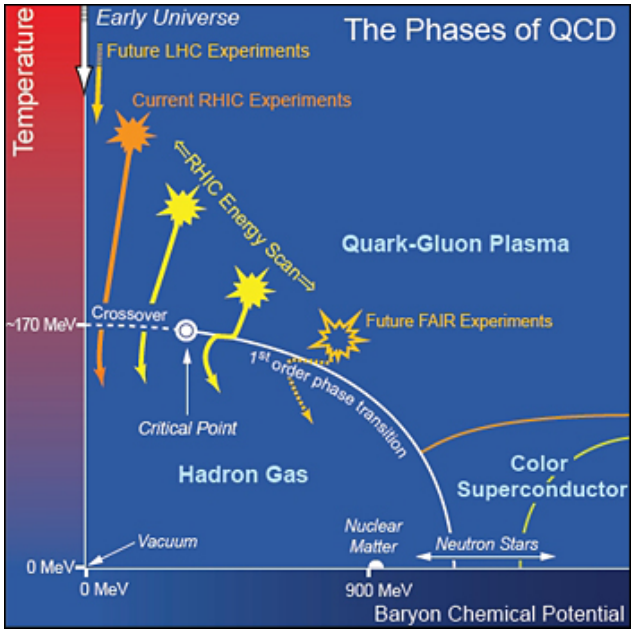

FIGURE 1.3: The diagram of QCD phase transition with various QCD matter states. Adapted from Ref. [9]

speculated that there exists a phase transition between the hadronic phase and a QGP phase as a result of all such observations. The effects of quark masses could not be adequately accounted for in the early lattice Monte-Carlo calculations. A true phase transition does not occur for realistic values of quark masses, according to arguments that began to arise around the middle of the 1980s. Instead, there is an abrupt but continuous change in the system's characteristics at a particular temperature and baryon chemical potential.

In modern times, we expect that there is a first-order phase transition line in the temperature and μ_B plane (Ref. Fig. 1.3). The only feasible phase at a high enough temperature is QGP, as the phase no longer depends on μ_B. Lattice calculations predict a smooth transition between the hadron gas phase and the QGP phase with a transition temperature in the range of $160 - 170$ MeV for zero baryon chemical potential, $\mu_B = 0$ [10–15]. High energy heavy-ion collision systems are extremely close to vanishing μ_B [10]. The phase relies on both the temperature and μ_B at temperatures below the critical temperature. There are models which indicate a first-order phase transition at finite μ_B with different transition temperatures. Therefore, we expect a critical point where the crossover region and the first-order transition line meet whose existence is not established experimentally. Quarks and gluons will combine into hadrons and take the phase of a hadron gas for low, but non-zero μ_B, below the phase transition line.

Increasing μ_B is proportional to increasing density. At very low temperatures and when μ_B is close to the nucleon mass ($\sim$ 1 GeV), a point is shown in the QCD phase diagram representing the transition to nuclear matter. The density exceeds that of nuclear matter for μ_B larger than 1 GeV, and a color superconducting state is formed, which may possibly exist in the neutron star core. If there is enough center of mass energy in the collisions, the system will be driven non-adiabatically to a region in the QGP phase. As collision energy grows, the temperature of this initial state rises, whereas μ_B falls as collision energy increases.

After the initial QGP state is created in heavy-ion collisions, the system cools and expands. It follows an isentropic expansion with a trajectory $\frac{d\mu_B}{dS} = const.$, where S is the entropy. Till the system experiences a phase transition and hadronizes, both the temperature and μ_B decrease. In the hadronic phase, the system continues to cool isentropically.

1.0.9 Relativistic heavy-ion collision experiments

1.0.9.1 Overview

The program for HIC experiments was started with the intention of studying a novel sort of matter known as the quark-gluon plasma, which is otherwise only seen soon after the big bang. The confinement transition occurred in the early universe's history when it was only a few microseconds old ($T \approx 100 - 200$ MeV). But as far as we can tell, this does not have any remnants that are currently detectable by astronomical observations. The concept of colliding heavy nuclei to create nuclear matter with a high temperature and density in a laboratory setting, maybe enough to reach and cross the critical line, first surfaced in the early 1980s. Following that, other operations have dedicated all or a portion of their science curriculum to studying heavy ion collisions such as AGS (Alternating Gradient Synchrotron) since 1960 at Brookhaven National Laboratory, U.S, SPS (Super Proton Synchrotron) since 1976 at CERN.

The Relativistic Heavy-Ion Collider (RHIC) at Brookhaven National Laboratory (BNL) in New York and the Large Hadron Collider (LHC) run by the European Organization for Nuclear Research (CERN) close to Geneva are now the principal locations for relativistic heavy-ion collision investigations. Atomic nuclei that have a mass number of more than three are referred to as "heavy ions".

At the CERN SPS, which collided heavy ions at a center of mass energy of 17 GeV, the first experimental hints of a deconfinement transition were seen [17]. In the subsequent experimental programs at higher energies (RHIC, LHC), the attention has moved from evaluating the production of a quark-gluon plasma towards quantifying some of its properties [18–31].

In the so-called interaction regions, two beams that are moving anti-parallel to one another at relativistic speeds (RHIC: $v > 99\%c$; LHC: $v > 99.9\%c$) around the accelerator ring are brought to contact. Detectors are incorporated into such contact zones. RHIC and LHC both contain several detectors. Each detector is a complex engineering work of art that is built, run, and managed by a huge team of engineers and physicists.

The nucleons of the two heavy nuclei are broken when they collide. For a limited duration, their constituents, the quarks and gluons flood out and create a new type of matter called quark-gluon matter. The quarks and gluons rapidly recombine into hadrons while traveling towards the detectors, meaning that this matter can only exist for a very brief period of time ($10^{-10} - 10^{-15}$ second) before it hadronizes.

Proton-proton collisions can also breach the strong interaction boundary to release the quarks and gluons at high enough energies, breaking nucleons into quarks and gluons. In all such collisions, the quark-gluon matter is produced. One interesting property related to the QGP matter is it can equilibrate. This means that the particles in the QGP matter can reach a local thermal equilibrium. Hence it is possible to find the probability density of finding quarks and gluons with a specific energy. This creates a locally thermalized QGP state.

In order to understand the characteristics of the QGP, the data on the emitted particles can be processed to create observables, which will then be compared with various theoretical test results. The detectors are used to determine a particle's species, as well as to calculate its energy and momentum. The resolution of the measurement is far lesser than the real scale of the collision area. Thus, from the detector's point of view, every collision is point-like and instantaneous. As a result, we do not know the particle's production times or decay locations. What we know is different types of observables in terms of particle distribution in the phase space. One class of observables of special importance is the anisotropy of the particle emission distribution in the transverse direction referred to by anisotropic flows v_n. These are obtained from the harmonic Fourier coefficients of the particle distribution.

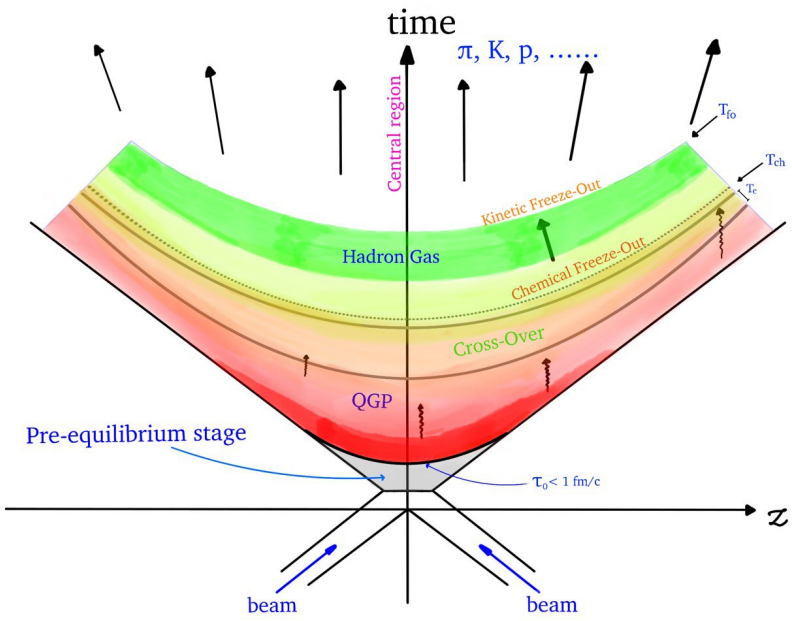

FIGURE 1.4: Heavy ion collision system evolution diagram

1.0.9.2 System Evolution

Figure 1.4 illustrates the progression of a nucleon-nucleon collision during a HIC experiment [32]. Here y-axis is the time axis, and the X-axis represents the longitudinal expansion. The two approaching nuclei in the diagram approach one another and meet at $t = 0$. As t increases, the system grows in size, and the temperature falls. It is expected that the state of matter we are looking for will happen immediately following pre-equilibrium but before the hadronization.

Hard processes like fragmentation, quark pair generation, and jet creation take center stage during the first few fm/c time of a heavy-ion collision. The system develops local thermal equilibrium through the process of hard scatterings, and a strongly interacting QGP phase is created. Due to its high temperature and density, the QGP phase expands and cools very quickly. The QGP hadronizes into hadron gas when the system approaches the phase transition temperature. This process is termed chemical freeze-out, and temperature is called chemical freeze-out temperature (T_{ch}). For the majority of the energies investigated in the HIC experiments, the shift from QGP to hadron gas is a smooth crossover. Hence, it should be remembered that various regions of the medium experience phase transitions at various times. This indicates that there is a stage in the system's evolution when the QGP matter is enclosed by a hadron gas.

The particles continue to communicate kinetically after a chemical freeze-out, and the created hadrons will disperse off one another elastically. During this stage of the system, some of the released hadrons will be unstable and decay. When the system reaches kinetic freeze-out, the elastic scattering stops. Due to the larger volume, the particles stop interacting. This temperature is known as the kinetic freeze-out temperature (T_{fo}). The created particles flow into the detectors after the final freeze-out. Their masses, charges, energy, and other attributes are then determined. We can only access the final state data from the detectors. Therefore any knowledge about the system's past states must be deduced from the particle spectra.

1.0.9.3 Geometry of collision

In heavy ion collisions, geometry is crucial to the analysis of the experimental data. The outcome of the experiments is highly correlated with the initial state particle distribution. That is why knowing the geometry parameters to analyze the observables efficiently is very important.

The impact parameter is one of the most important geometry parameters for studying heavy ion collision observables. It is a measure of the centrality of a collision event and is not known a priori. It is the distance between the center of the two colliding nuclei on a plane perpendicular to the beam axis. The z direction is usually taken as the beam direction. So, the impact parameter b is calculated on the $x-y$ plane along the x direction. When the collision between the two nuclei is exactly a head-on collision, in that case, the impact parameter $b = 0$ fm. We refer to this type of collision as a central collision. As the impact parameter becomes larger, we describe those collisions as peripheral collisions. This can be as large as the diameter of the colliding nuclei. In the case of Au nuclei, most peripheral collisions can have impact parameters of 14 fm because 7 fm is roughly the radius of a gold nucleus.

Consider a collision shown in Fig. 1.5(a) that is non-central between two identical spherical nuclei moving in opposing directions along and opposite to the Z axis. In this figure, AB is the impact parameter along the X axis. Z is the longitudinal direction. The $X-Y$ plane is the transverse plane (also known as the azimuthal plane) which is perpendicular to the beam direction (Z-axis). The plane made by the $X-Z$ axis represents the reaction plane, and the azimuthal angle of the particle is denoted by ϕ. The overlap region is shown by the shaded area. In a real experiment, the impact parameter vector's magnitude and direction are unknown and vary from event to event (Fig. 1.5(b)). In

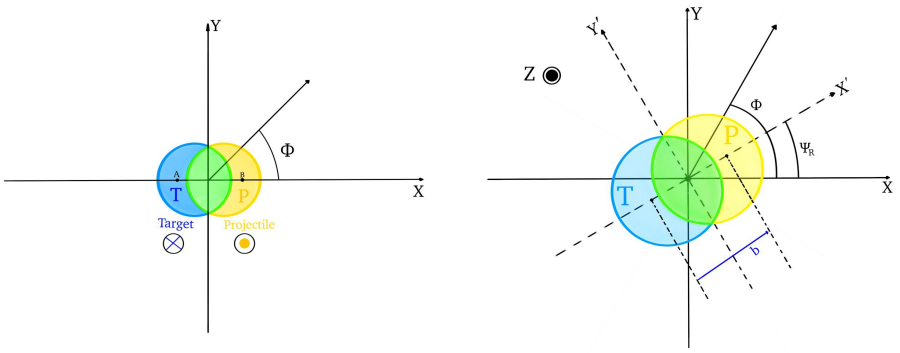

FIGURE 1.5: Schematic diagram of system geometry of HIC experiments

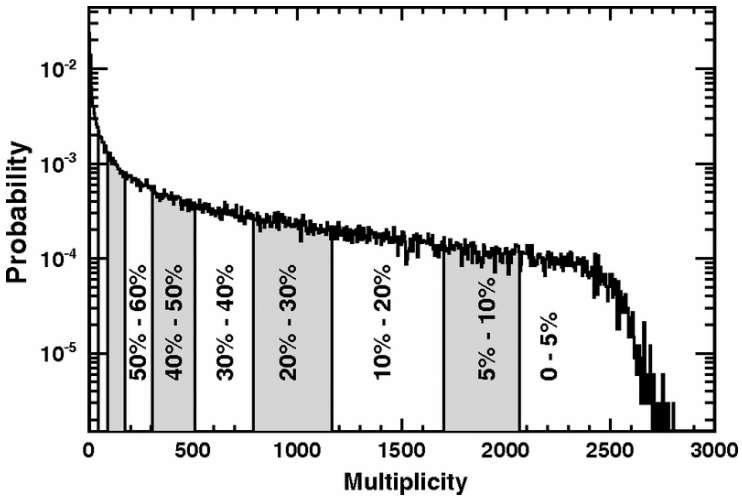

FIGURE 1.6: Centrality dependence charged particle multiplicity of produced hadrons in Pb-Pb collision at $\sqrt{s_{NN}} = 2.76$ TeV, ref. [34]

Fig. 1.5(b), a random event is shown. Here, XYZ is the lab-fixed axis. The impact parameter of the event is making an angle Φ_R with the lab X axis. If $\Phi_R \neq 0$, we call the xz plane the participant plane. This is analogous to the reaction plane when there is no event-by-event fluctuation.

The distribution of particles in the end state, in particular in the transverse plane, may be impacted by the initial configuration. Experimentally, it is assumed that more central collisions have greater multiplicities, and the collision centrality for an event is calculated using the event's multiplicity. The centrality dependence of charged particle multiplicity is shown in Fig. 1.6 for Pb-Pb collisions at $\sqrt{s_{NN}} = 2.76$ TeV. Glauber Monte-Carlo simulations are performed and fitted to the experimental data to determine the relationship between observed multiplicities and estimated centralities.

1.0.9.4 Main Observables

Here we have shown some of the main observables of RHICE.

- **Transverse Momentum Spectra:**
  When examining the QGP state and formation of QGP matter at large energy densities, spectrum analysis is a crucial resource. Transverse mass spectra provide information about the created particle's energy and momentum distribution. The spectra carry details about the system at kinetic freeze-out. Fig. 1.7 shows the p_T spectra of various hadrons of Au-Au collision at $\sqrt{s_{NN}} = 62.4$ GeV. The lines in each figure show the fitting to the experimental data of different centrality bins from top to bottom, $0-5\%$, $5-10\%$, $10-20\%$, $20-30\%$, $30-40\%$, $40-50\%$, $50-60\%$, $60-70\%$, and $70-80\%$. The greater part of the particles is generated at low-p_T ($p_T < 1GeV/c$) region [35].

  The transverse momentum spectra of various particles have both collective and random characteristics. The random component can be used to get the kinetic freeze-out temperature. Examining particle spectra in this region also enables the extraction of bulk properties, e.g., the system's collectivity and thermalization. These bulk properties arise due to the density gradient in the initial state from the center to the edge of the fireball. This is also one of the primary reasons for the collective flow generation. The equation of state of the expanding QGP system has an impact on this collective flow. In Fig. 1.7, the fits shown are used to extract the model parameters characterizing the collective component defined by the radial flow velocity (β_T) and the random component represented by the kinetic freeze-out temperature T_{f0} of the system.

- **Particle Ratios:**

  The hadron yield ratios of central Au+Au collisions measured by STAR are compared to statistical model fits in Fig. 1.8. Under the assumption that there exists a thermal and chemical equilibrium at that point, the observed ratios are used to estimate the values of system temperature and baryon chemical potential during chemical freeze-out.

  The temperature derived from the fits approaches the Hagedorn limit for a hadron-resonance gas, which was predicted without taking into account quark and gluon degrees of freedom. It is roughly comparable to the crucial value of temperature for a QGP-to-hadron-gas transition indicated by lattice QCD. The inferred value

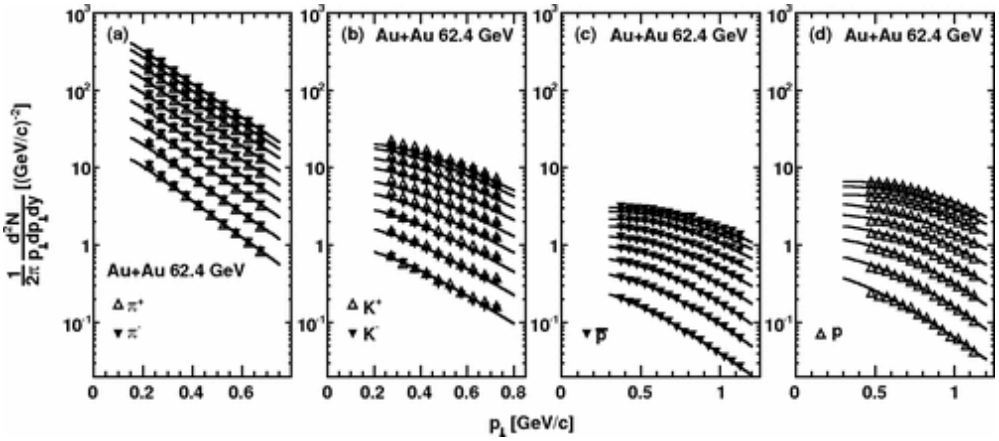

FIGURE 1.7: Midrapidity ($|y| < 0.1$) identified particle spectra in Au+Au collisions at 62.4 GeV [36].

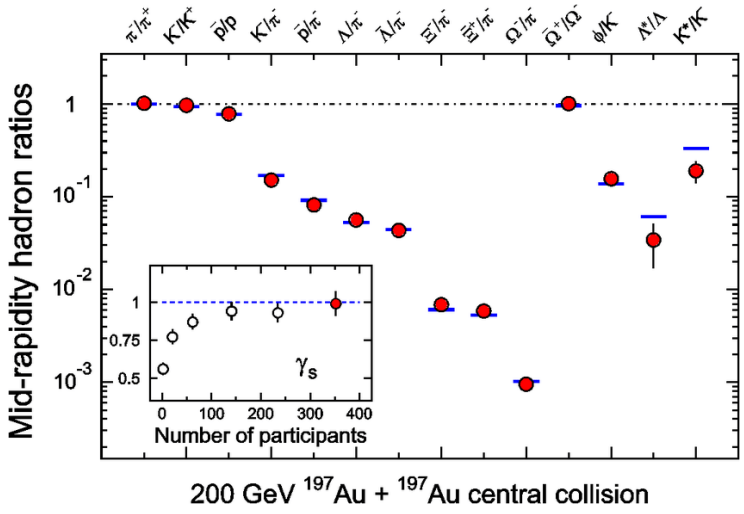

FIGURE 1.8: Ratios of p_T-integrated mid-rapidity yields for different hadron species measured in STAR for central Au + Au collisions at $\sqrt{s_{NN}} = 200$ GeV [37].

of T_{ch} serves as a lower bound on the thermalization temperature, assuming that the bulk matter does actually reach thermalization before chemical freeze-out.

- **The Signatures of QGP:** There are various ways to examine the material produced in a heavy-ion collision. Some of them are given below:

  - **Correlations and fluctuations** Fluctuations are reactive to the degrees of freedom of the system in concern. The degrees of freedom are higher in the QGP phase than in the hadronic phase. As a consequence, the signature of QGP formation could be found by observing the changes in conserved variables, like charge, energy, temperature, or transverse momentum, around the transition temperature [38]. In the proximity of the critical point, these fluctuations ought to be extremely strong. Likewise, a deconfined QGP phase

may also be characterized by the correlation of charges and their corresponding anti-charge generated in later-stage hadronization [39]. As fluctuations are related to the thesis topic, we have talked more about fluctuations in the later chapters.

- **Photon and dilepton measurements** The strong interaction between the dileptons and photons with the QGP medium is nearly zero. As a result, they emerge from the medium unaffected by the expanding fireball retaining knowledge of the originating state. Thermal photons might be used as a temperature probe, and the reconstructed spectral densities of vector mesons, such as the ρ-meson, might suggest that chiral symmetry has been restored [40].
- **Hard probes, jet quenching** A jet is created when a parton from one nucleon scatters off of a parton from another nucleon and generates a parton shower. The partons are then hadronized and produce a collimated spray of hadrons. It is possible to estimate jet production from collisions with a high enough momentum transfer using perturbative theories. In a process known as jet quenching, partons on their way interact with the quark-gluon plasma created in high-energy heavy-ion collisions, and in the process, they may lose energy before the generation of the final hadrons. Recently, there has been a lot of interest in the jet quenching phenomena as this is one of the direct evidence of QGP formation [41].
- **Strangeness Enhancement** The generation of thermal $s\bar{s}$ pair can happen at a temperature of more than 300 MeV. So, it is most likely to be created in a deconfined phase where the temperature is such that a sufficient number of s-quarks can be produced. Hence the formation of a QGP matter can enhance the generation of multi-strange particles, which is observed experimentally [42].
- **The J/ψ particle production** It was first thought that color screening hinders $c\bar{c}$ binding, which would explain why the generation of J/ψ, which is a $c\bar{c}$ bound state, is inhibited in the QGP state [43]. In fact, the J/ψ diffuses in the QGP stage. This suggests rapid formation and quick annihilation. Conversely, according to lattice calculations, the J/ψ can withstand temperatures higher than the QGP critical temperature, and because the LHC produces a huge number of c-quarks, its production may potentially be improved at high collision energies [44].

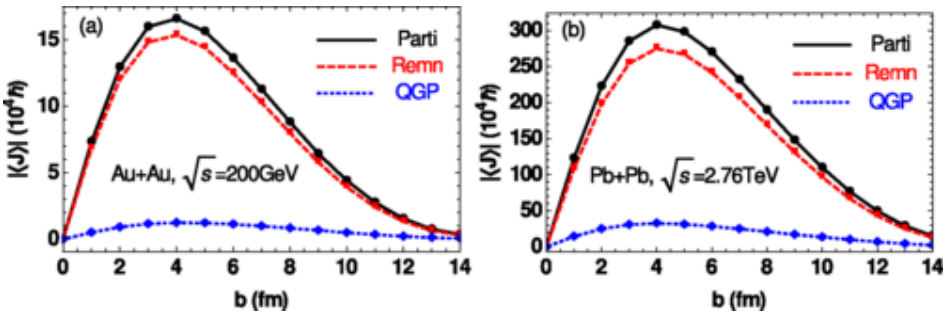

FIGURE 1.9: impact parameter dependence of the angular momenta [12]

1.0.10 Motivation of the Thesis

1.0.10.1 The study of vorticity

The system created in heavy ion collisions exhibits strong collective effects for a significant portion of its lifetime that can be explained by relativistic hydrodynamics. A strong elliptic flow is seen in such collisions, which indicates that the produced quasi-macroscopic system is strongly coupled and has an incredibly low viscosity to entropy density ratio [45]. This indicates that the system may have an extremely high vorticity, possibly the highest ever created. Peripheral collisions generate huge orbital angular momenta J_0 orthogonal to the reaction plane [12, 46]. For instance, the total initial angular momentum $J_0 \propto b\sqrt{s_{NN}}$ for a non-central collision, where b is the impact parameter. Therefore, J_0 can be as high as 10^5 in an Au-Au collision at RHIC energies with $\sqrt{s_{NN}} = 200$ GeV and 10^7 for $b = 5$ fm Pb-Pb collisions at energies of 5.5 TeV at the LHC (Ref. Fig. 1.9) [48].

After the impact, the spectators fly rapidly far from the collision area, carrying a chunk of J_0 with them. The rest are carried by the QGP matter produced in the collision. This part of J_0 can produce a longitudinal momentum density. Particles with spin can become polarised due to spin-orbit coupling as the system has global longitudinal momenta. The spin-orbit coupling in microscopic particle interactions can lead to the spin-vorticity coupling in a fluid. This is true when we calculate an ensemble average across randomized incoming momenta of colliding particles in a locally thermalized fluid [49]. In this manner, the fluid's spin polarisation and vorticity field are connected. The term "global polarisation" refers to this particular kind of spin polarisation with respect to the reaction plane [50].

Global spin polarisation investigations of Λ and $\bar{\Lambda}$ have been performed for Pb+Pb collisions at 5.06 TeV and 2.76 TeV[51] by the ALICE collaboration and for Au+Au

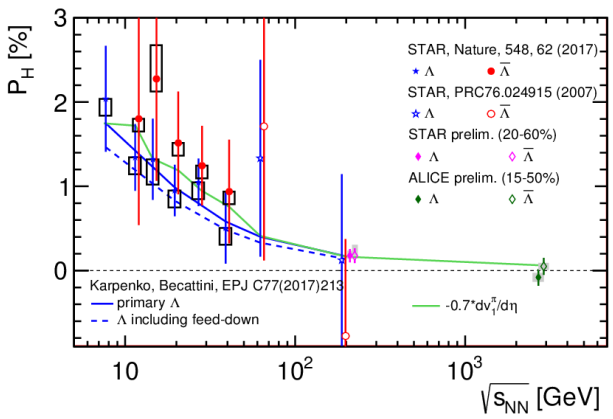

FIGURE 1.10: Average polarization(global) of Λ hyperons with collision energy $\sqrt{s}$.

collisions by the STAR collaboration throughout a broad range of collision energy, $\sqrt{s_{NN}}$ = 7.7GeV−200 GeV [32, 33]. The average global polarization for Λ particles as a function of collision energy is shown in Fig. 1.10. The global spin polarization is around 2% at the lowest RHIC energy, falls to approximately 0.3% at the highest RHIC energy (200 GeV), and nearly disappears at higher energy ranges. Thus, looking at the local vorticity distribution at different stages of system evolution becomes very important. As viscous characteristics of the medium also affect the vorticity distribution and average vorticity patterns, it is also interesting to see how these two effects are correlated. It is also compelling to observe how these two effects influence the QGP medium at different stages of system evolution.

1.0.10.2 Study of anisotropy through power spectrum

The produced initial medium featured inhomogeneities in the transverse plane because of the randomness in the phase space distribution of the nucleons in the colliding nuclei. It was commonly recognized that there are uncertainties resulting from the errors in specifying the angle of the event-plane. As a result of all these variabilities, certain variables, such as anisotropic flow coefficients $(v_2, v_3, ...)$ in a non-central collision encounter event-by-event fluctuations [54–57]. In previous studies, the power spectrum of the flow coefficients is calculated keeping in mind that it can retain the signs of the fluctuations in the initial stage [58, 59]. It was also noticed that these initial fluctuations could cause these flow coefficients to have tiny nonzero values even in central collisions.

This is quite similar to the analysis of the power spectrum of anisotropies produced by fluctuations in the early inflationary universe found in the CMBR (Cosmic Microwave

Background Radiation). In fact, when discussing HIC, it is sometimes stated in simpler terms that attempts to comprehend the early cosmos from studies of the cosmic microwave background radiation are akin to attempts to understand the early phases of QGP matter from observations of finally produced hadrons. The freezeout surface in heavy ion collisions can therefore be compared to the final scattering surface for CMBR. The final scattering surface depicts the universe's neutrality when protons and electrons have recombined, and photons are free to stream through space. Such qualitative assertions were elaborated in refs. [60, 61] to a more in-depth level of connection between flow fluctuations in heavy ion collisions and the CMBR disturbances in the universe. As the power spectrum study of CMBR anisotropy was successful in giving critical details on first inflationary density fluctuations, power spectrum analysis can become a very efficient tool for probing the fluctuations in the initial stage.

The existence of vorticity suggests the presence of anisotropic flow components, which indicates a deviation from the laminar-like flow. The fluctuations in the flow can be studied in terms of turbulence spectra. The plasma created in these collisions has a very high Reynolds number, creating an imbalance in the inertial and viscous forces in the plasma. This makes the fluctuations sustainable, and the Kolmogorov spectra can be obtained in such cases. In 1941, Kolmogorov hypothesized that real turbulent flows, despite their inhomogeneities and anisotropy at larger scales, are essentially locally homogenous and isotropic on small scales. The phenomenological theory K41, which is regarded as one of the most successful theories of turbulence, is built on the foundation of the Kolmogorov hypothesis (KH) [62–64]. Because spectral analysis makes it simple to distinguish between various spatial scales, it is crucial for solving the turbulence problem. This has been discussed in more detail in chapter III, where we used different planes to study the turbulence spectra and look for the non-uniformity over the planes that suggest the anisotropy in the plasma.

1.0.10.3 Study of temperature fluctuation using Tsallis Statistics

As already discussed, all interactions stop at kinetic freeze-out, and the particle ratios and the spectra of the created particles remain unaltered. Therefore, one of the fundamental measurements to determine the kinetic freeze-out phase of the systems generated in high-energy collisions is the p_T spectra of the produced particles. A number of different classical statistical models like Boltzmann-Gibbs (BG), Fermi-Dirac, m_T-exponential distribution, Tsallis distribution, and Erlang distribution are often used to characterize the p_T spectra and extract physical parameters. In understanding the thermodynamic features of various physical systems, the BG statistical model has had great success.

The BG model, however, is insufficient to explain the large transverse momentum range, which is primarily characterized by the inverse power-law behavior. With the thermal blast-wave model, the same is true. Historically, the p_T spectra of heavy-ion collisions have been fitted using the blast-wave model. [65][66–70]. This model makes the basic assumption that the collision medium freezes out kinetically at temperature T_{kin} and that particles are traveling at a uniform collective radial flow velocity (β_r). However, the spectra at mid to high-p_T ranges cannot be described by the blast-wave approach. It has been demonstrated that the p_T spectrum is best described by the non-extensive Tsallis statistics not only in pp collisions but also for heavy ion collisions [71, 72]. Like other distribution fittings, one can acquire the Tsallis fit parameters, q, which represents the level of departure from the equilibrium state and T stands for the effective temperature. The dependencies of these tuning parameters on the system variables can be studied.

There is another aspect of this story that we are particularly interested in. As has been discussed earlier, although it is highly probable to attain a local thermal equilibrium after a certain time in QGP evolution, there are temperature fluctuations in the plasma in the earlier stage and in the pre-equilibrium state. For systems with temperature fluctuations or varying energy dissipation, the non-additivity condition of the Tsallis entropies in non-extensive statistical theory has a clear and concise physical meaning [73–76]. For a system that can be described formally by a fluctuating β (inverse of temperature), where β is χ^2 distributed, the integration over all possible fluctuating inverse temperatures results in the generalized distribution functions of non-extensive statistics. Our motivation is to see whether the temperature states in HIC systems could be fitted with a χ^2 distribution. If so, then what would be the behavioral changes of the q parameter found from these temperature fluctuations in the partonic phase, q being the non-extensive parameter. In chapter IV, we have addressed this in detail, where we showed how the fitting parameters q and effective temperature T in the partonic stage vary with system parameters like $\sqrt{s_{NN}}$, system size, and centrality. We will also discuss the similarities of our results with the experimental observations.

1.0.10.4 Obtain Initial state parameters using machine learning

The understanding of various results obtained in HIC experiments is strongly influenced by the initial geometry overlap zone of two colliding ions. Several parameters are developed to define initial stage properties like eccentricity, event plane angles, etc. The impact parameter is one such parameter that plays a crucial role in interpreting the results, as it is a representation of collision centrality. However, it is practically impossible to asses these parameter values from experiments as the QGP is created for a very short

period of time, and almost instantaneously, it hadronizes and produces hadronic matter. Another reason is that the system created in such collisions is so tiny with dimensions in fm, that any kind of external probing is impossible. However, theoretical methods have been designed that allow us to determine such initial state parameters based on outcomes. One such formalism is the Glauber model, which uses experimental data and multiple nucleon scattering in nuclear targets to predict impact parameters and the number of participant nuclei [77–79].

The impact parameter has been calculated using various machine learning (ML) techniques for several years [80–85]. In high energy collisions, ML approaches are generally employed for problems including classification, clustering, and regression. To predict the initial state parameters, one needs to use supervised regression models, where the target variable is a finite numerical value for every set of input data. Each dataset corresponds to the observables from the final state of a single heavy-ion collision event. An event generator like AMPT, UrQMD, etc., can be used to create the events. The models learn from the data and estimate the target variable for every new event dataset.

The use of these ML models in heavy ion collision experiments has two significant limitations. The first one is the training is extremely sensitive to the training data. That is why it is essential to generate events that are as similar to the experimental data as possible. Otherwise, the ML model will not perform well while testing experimental data. This motivates us to try out several different types of heavy ion collision simulation models to train an ML model and see whether it is capable of predicting target variables for the test data of a different model.

The second issue is related to the distribution of training data with respect to the target variable. The event distribution is not uniform throughout the range of target variables, leading to an imbalance in the data. As a result, the prediction accuracy gets largely affected in certain regions. This inspired us to employ various sampling techniques in order to create a uniform data distribution and improve prediction accuracy. The details of our study are given in chapter V.

Bibliography

[1] S.L. Glashow Nucl. Phys. 22 (4) , 579 (1961); S. Weinberg, Phys. Rev. Lett. **19**, 1264 (1967); A. Salam N. Svartholm (Ed.), Proceedings of the Eighth Nobel Symposium, Almqvist & Wiksell (1968), 367 (1968); G. 't Hooft, M. Veltman, Nucl. Phys. B **44**, 189 (1972).

[2] G. Aad et al. (ATLAS Collaboration), Phys. Lett. B **716**, 1, 1-29 (2012).

[3] B.P. Abbott et al. (LIGO Scientific Collaboration and Virgo Collaboration), Phys. Rev. Lett. **116**, 061102 (2016).

[4] E. Eichten, K. Gottfried, T. Kinoshita, J. Kogut, K. D. Lane, and T. -M. Yan, Phys. Rev. Lett. **34**, 369 (1975).

[5] E. Eichten, K. Gottfried, T. Kinoshita, K. D. Lane, and T. -M. Yan Phys. Rev. D. **17**, 3090 (1978).

[6] Sidney Coleman and David J. Gross. Price of asymptotic freedom. Phys. Rev. Lett. **31**, 851–854, (1973).

[7] The European Physical Journal Conferences **95**, 04015 (2015).

[8] J. C. Collins and M. J. Perry, Phys. Rev. Lett. **34**, 1353 (1975).

[9] STAR Collaboration, Studying the Phase Diagram of QCD Matter at RHIC, https://drupal.star.bnl.gov/STAR/files/BES_WPII_ver6.9_Cover.pdf

[10] A. Bazavovi et al., Phys. Rev. D **85**, 054503, (2012).

[11] C. Bernard, T. Burch, C. DeTar et al., Phys. Rev. D **71**, 034504, (2005).

[12] Y. Aoki, G. Endrődi, Z. Fodor et al., Nature **443**, 675–678 (2006).

[13] M. Cheng et al., Phys. Rev. D **79**, 074505, (2009).

[14] A. M. Halasz et al., Phys. Rev. D **58**, 096007, (1998).

[15] J. Berges and K. Rajagopal, Nucl. Phys. B **538**, 215–232, (1999).

[16] J. Cleymans, H. Oeschler, K. Redlich et al., Phys. Rev. C **73**, 034905, (2006).

[17] M.C. Abreu et al., Phys. Lett. B **477**, 28–36, (2000).

[18] John Adams et al., Nucl. Phys. A **757**, 102–183, (2005).

[19] K. Adcox et al. Nucl. Phys. A **757**, 184–283, (2005).

[20] I. Arsene et al., Nucl. Phys. A **757**, 1–27, (2005).

[21] B.B. Back et al., Nucl. Phys. A **757**, 28–101, (2005).

[22] K Aamodt et al. Phys. Rev. Lett. **105**, 252302, (2010).

[23] K. Aamodt et al. Phys. Lett. B **696**, 30-39, (2011).

[24] K. Aamodt et al. Phys. Rev. Lett. **107**, 032301, (2011).

[25] Betty Abelev et al. Phys. Lett. B **719**, 29-41, (2013).

[26] Georges Aad et al. Phys. Rev. Lett. **105**, 252303, (2010).

[27] Georges Aad et al. Phys. Rev. C **86**, 014907, (2012).

[28] Georges Aad et al. Phys. Rev. Lett. **110**, 182302, (2013).

[29] Vardan Khachatryan et al. JHEP **09**, 091, (2010).

[30] Serguei Chatrchyan et al. Phys. Rev. C **84**, 024906, (2011).

[31] Serguei Chatrchyan et al. Phys. Lett. B **718**, 795-814, (2013).

[32] H. Satz, Nucl. Phys. A **715**, 3 (2003)

[33] Rajeev S. Bhalerao, arXiv:1404.3294.

[34] K. Aamodt et al. (ALICE Collaboration) Phys. Rev. Lett. **105**, 252302 (2010).

[35] Proc. Indian Natn. Sci. Acad. **72**, No.3, 153-158 (2006).

[36] B. I. Abelev et al. (STAR Collaboration), Phys. Rev. C **79**, 034909 (2009).

[37] I. Arsene et al. Nuclear Physics A **757**, (1-2), 1-27 (2005).

[38] S. Jeon and V. Koch, arXiv:hep-ph/0304012.

[39] S. A. Bass, P. Danielewicz and S. Pratt, Phys. Rev. Lett. **85**, 2689 (2000).

[40] R. Rapp and J. Wambach, Adv. Nucl. Phys. **25**, 1 (2000).

[41] Christine Nattrass 2017 J. Phys.: Conf. Ser. **832**, 012001 (2017).

[42] E. Andersen et al. [WA97 Collaboration], Phys. Lett. B **449**, 401 (1999).

[43] T. Matsui and H. Satz, Phys. Lett. B **178**, 416 (1986).

[44] A. Andronic, P. Braun-Munzinger, K. Redlich and J. Stachel, Nucl. Phys. A **789**, 334 (2007)

[45] K. Aamodt et al. (ALICE Collaboration), Phys. Rev. Lett. **105**, 252302 (2010).

[46] Z. T. Liang and X. N. Wang, Phys. Rev. Lett. **94**, 102301 (2005)

[47] Wei-Tian Deng and Xu-Guang Huang, Phys. Rev. C **93**, 064907 (2016).

[48] F. Becattini, F. Piccinini, and J. Rizzo, Phys. Rev. C **77**, 024906 (2008).

[49] J. j. Zhang, R. h. Fang, Q. Wang and X. N. Wang, Phys. Rev. C **100**, 064904 (2019)

[50] F. Becattini, L. P. Csernai, and D. J. Wang Phys. Rev. C **88**, 034905 (2013).

[51] S. Acharya et al. [ALICE], Phys. Rev. C **101**, 044611 (2020)

[52] L. Adamczyk et al. [STAR], Nature **548**, 62-65 (2017)

[53] J. Adam et al. [STAR], Phys. Rev. C **98**, 014910 (2018)

[54] P. Sorensen (for the STAR collaboration), J. Phys. G **34**, S897 (2007)

[55] S. Manly et al. (for PHOBOS collaboration), arXiv:nucl-ex/0702029

[56] R. S. Hollis et al. (for PHOBOS collaboration), arXiv:nucl-ex/0707.0125

[57] H. Sorge, Phys. Rev. Lett. **82**, 2048 (1999).

[58] Shreyansh S. Dave, P. S. Saumia, Ajit M. Srivastava, The European Physical Journal Special Topics **230**, 673–688 (2021).

[59] M. Machado, P. H. Damgaard, J. J. Gaardhøje, and C. Bourjau Phys. Rev. C **99**, 054910 (2019).

[60] A.P. Mishra, R.K. Mohapatra, P.S. Saumia, A.M. Srivastava, Phys. Rev. C **77**, 064902 (2008).

[61] A.P. Mishra, R.K. Mohapatra, P.S. Saumia, A.M. Srivastava, Phys. Rev. C **81**, 034903 (2010).

[62] Zi-Ju Liao and Wei-Dong Su; Physics of Fluids **27**, 041701 (2015)

[63] A. N. Kolmogorov, C. R. Acad. Sci. URSS **30**, 301–305 (1941).

[64] U. Frisch, Turbulence: The Legacy of A.N. Kolmogorov (Cambridge University Press, 1995).

[65] E. Schnedermann, J. Sollfrank, U.W. Heinz, Phys. Rev. C **48**, 2462 (1993)

[66] B. Abelev et al., STAR Collaboration. Phys. Rev. C **79**, 034909 (2009)

[67] L. Adamczyk et al., STAR Collaboration. Phys. Rev. C **96**, 044904 (2017)

[68] J. Adam et al., STAR Collaboration. Phys. Rev. C **101**, 024905 (2020)

[69] B. Abelev et al., ALICE Collaboration. Phys. Rev. C **88**, 044910 (2013)

[70] S. Acharya et al., ALICE Collaboration. Phys. Rev. C **101**, 044907 (2020)

[71] C. Tsallis, J. Stat. Phys. **52**, 479 (1988)

[72] C. Tsallis et al., Physica A **261**, 534 (1998)

[73] C. Beck, G.S. Lewis and H.L. Swinney, Phys. Rev. E **63**, 035303(R) (2001)

[74] I. Bediaga, E.M.F. Curado, and J. Miranda, Physica A **286**, (1-2), 156-163 (2000)

[75] C. Beck, Physica A **286**, (1-2), 164-180 (2000)

[76] G. Wilk and Z. Wlodarczyk, Phys. Rev. Lett. **84**, 2770 (2000)

[77] M. L. Miller, K. Reygers, S. J. Sanders, and P. Steinberg, Annu. Rev. Nucl. Part. Sci. **57**, 205 (2007).

[78] C. Loizides, Phys. Rev. C **94**, 024914 (2016).

[79] R. J. Glauber and G. Matthiae, Nucl. Phys. B **21**, 135 (1970).

[80] S. A. Bass, A. Bischoff, C. Hartnack, J. A. Maruhn, J. Reinhardt, H. Stoecker, and W. Greiner, J. Phys. G **20**, L21 (1994).

[81] F. Li, Y. Wang, H. Lü, P. Li, Q. Li, and F. Liu, J. Phys. G **47**, 115104 (2020).

[82] C. David, M. Freslier, and J. Aichelin, Phys. Rev. C **51**, 1453 (1995).

[83] S. A. Bass, A. Bischoff, J. A. Maruhn, H. Stoecker, and W. Greiner, Phys. Rev. C **53**, 2358 (1996).

[84] F. Haddad, K. Hagel, J. Li, N. Mdeiwayeh, J. B. Natowitz, R. Wada, B. Xiao, C. David, M. Freslier, and J. Aichelin, Phys. Rev. C **55**, 1371 (1997).

[85] J. De Sanctis, M. Masotti, M. Bruno, M. D'Agostino, E. Geraci, G. Vannini, and A. Bonasera, J. Phys. G **36**, 015101 (2009).

Chapter 2

Vorticity distribution and flow characteristics in relativistic HIC system

2.1 Introduction

The rotating characteristics of QGP collective motion and the effects it generates have garnered a lot of curiosity in recent times. In the peripheral collisions, the collision of heavy ions produce a significant amount of angular momentum. After the initial collision, the spectator nuclei carry the bulk of this total angular momentum with them, but a sizeable portion is retained in the generated QGP. This shows a nonzero rotating motion in the system. This encouraged research on the vorticity in HIC systems. It is observed that the total angular momentum is proportional to the centrality of the collision and the collision energy ($\sqrt{s_{NN}}$) [1],

$$j \propto b\sqrt{s_{NN}} \tag{2.1}$$

Here impact parameter is represented as b.. While the vorticity contributes to the study of the fluid's viscous characteristics, it has also been hypothesised that it may result in a number of anomalous phenomena. Anomalous transport effects can result from the presence of a strong electromagnetic field in the background that can connect to parity or charge odd regions in the plasma and generate currents. This phenomena is popularly known as chiral magnetic effect (CME) [2]. The chiral vortical effect (CVE) [3], which is the vortical equivalent of the CME and denotes the creation of vector and axial currents along the vorticity, is comparable to this effect. Recent observations by the

STAR Collaboration at RHIC [4] and the ALICE Collaboration at the LHC [5] revealed characteristics associated with these various effects. Several groups have studied the observational evidence of the polarisation of Λ hyperons caused by vorticity [6, 7]. In this chapter, we do not, however, examine polarisation. We instead study the viscous effects of QGP.

Although shear stress does not directly contribute to the creation of the plasma vorticity, it does influence how the vorticity evolves when it interacts with the plasma. The chemical potential μ_B (or baryon density) of the plasma affects the shear viscosity, according to the hadronic resonance gas (HRG) model. We are interested in assessing how shear viscosity affects the vorticity patterns observed in the QGP since this determines how vorticity patterns evolve in a viscous fluid. Therefore, we conduct a systematic analysis of the vorticity produced in heavy ion collisions at various collision energies. The chemical potential and thus the baryon density are connected to different $\sqrt{s_{NN}}$. We study the average vorticity for various cases by using different definitions of vorticity. In every situation, as the collision energy rises, the average vorticity changes. The values of shear viscosity for various collision energies are then calculated using the HRG models. It is shown that the shear viscosity does not depend heavily on the collision energy and the chemical potential.

The vorticity is the same as the rotational angular velocity in the case of a rigid-body rotation with a global angular velocity around an axis. Of course, a rotating fluid differs greatly from a rigid body, and the vorticity field generally does not remain constant throughout the fluid. The relationship between angular momentum and vorticity is generally somewhat complex. There are numerous possible reasons of angular momentum generation. An example of a potential reason for nonzero angular momentum is an inhomogeneous distribution of energy density and mass of the fluid which is measured as the inertia. If we take a scenario where the entire system is flowing at the same speed but more matter is concentrated on one side than the other, the angular momentum will not be zero even in the absence of vorticity. However, the angular momentum associated with a nonzero vorticity is what we are particularly interested in. It would be interesting to see how the interplay between viscosity and angular momentum affects the nature of vorticity distribution across the collision energy range.

In section II, we address dissipative hydrodynamics and the reaction plane vorticity. We go through shear viscosity and the hadron resonance gas models in section III. We present the shear viscosity computation from the HRG model, and also demonstrate that it is comparable to other calculations that have been given by the hydrodynamic models in the past. We give the details of our simulations in Section IV, and in Section

V, we give the results and go over the significance of them. Finally, in section VI, we talk about our conclusions.

2.2 Different definitions of vorticity

Dissipative hydrodynamics has attracted a lot of attention recently as a result of the development of several experimental results at lower collision energies [8]. A number of simulation codes, including ECHO - QGP [9], VISHNU [10, 11] etc., have been used to analyze it. Multiple types of vorticity have been described, and different aspects of dissipative dynamics have been examined. Here, we analyze the vorticity patterns in relation to the fluid's baryon density that was created after the collisions. A study with regard to the collision energy would entail a study with regard to the baryon chemical potential since, as we will describe later, the μ_B is correlated to the collision energy.

Vorticity in classical fluid dynamics is the curl of the velocity field $\mathbf{v}$. This net vorticity travels with the fluid and is static for an ideal fluid. The fluid's rotating motion is largely reflected by the vorticity. The rotational motion will also produce viscous stress between the fluid layers for a viscous fluid. Since there are no boundary conditions in heavy ion collisions, the viscous stress in the layers of the rotating fluid will cause the local vorticity patterns to form. In several investigations of vorticity, the fluid has been described by the moment of inertia tensor to give an explanation for the rotating mass. Other times, the vorticity has been described using relativistic hydrodynamics. However, there are other approaches to describe vorticities in relativistic hydrodynamics [9]. In our present simulations, we explore the classical vorticity, the kinematical vorticity, and the thermal vorticity with the proper weights.

Based on the momentum of the particles involved in the heavy ion collision, we want to quantify the amount of vorticity they produce. The system's high Reynolds number is one of the factors used to compute the vorticity using momentum. The fluid in a heavy ion collision has an extremely high Reynolds number [12, 13]. In these conditions, the majority of the fluid is subject to relatively low viscous stresses. The vorticity's impact is then restricted to the thin layers of the rotating fluid. Thus, we will have local vorticity due to the momentum of the particles. Although vorticity is a three-dimensional object described by $\omega_i = \epsilon_{i,j,k}\frac{\partial v_k}{\partial x_j}$, it has been demonstrated in a number of earlier simulations that the angular momentum in the y-direction (or out of plane axis) is significantly bigger than the angular momentum in the other directions. We first compute the vorticity in all three dimensions for a given $\sqrt{s_{NN}}$. We discover that the y-direction component of vorticity is significantly larger than the x and z direction components. Therefore, we only compute the vorticity in the reaction plane for all other collision energies. The

classical vorticity in the reaction plane is given by,

$$\omega_y = \omega_{xz} = \frac{1}{2}(\partial_z v_x - \partial_x v_z) \tag{2.2}$$

The three velocity components in this case are v_x, v_y, v_z, and factor 1/2 is added to provide for symmetrization. Though the velocities in these collisions are relativistic, we have performed the computations for a classical vorticity considering the low fluctuation scenarios. The general nature is also the same for both the classical and relativistic instances, as demonstrated in ref. [27]. As a result, we handle both the classical and relativistic cases.

The vorticity in the relativistic condition is determined by

$$\omega_{\mu\nu} = \frac{1}{2}(\partial_\nu u_\mu - \partial_\mu u_\nu) \tag{2.3}$$

where, $\partial_\mu = (\partial_0, \partial_x, \partial_y, \partial_z)$ and $u_\mu = \gamma(1, -v_x, -v_y, -v_z)$. As a result, in the reaction plane, we would obtain,

$$\omega_{xz} = \frac{1}{2}\gamma(\partial_z v_x - \partial_x v_z) + \frac{1}{2}(v_x \partial_z \gamma - v_z \partial_x \gamma) \tag{2.4}$$

We would like to talk more in-depth about the relativistic vorticity before getting into the specifics of the simulation and the outcomes. The relativistic vorticity is always larger than the classical vorticity [27] due to the presence of the γ coefficient. Therefore, comparing the sizes of the classical and relativistic vorticities is challenging. If they are given different weights, as was done in ref. [27], one may be able to compare them. In reality, we realized that adding some weight function is crucial to get the final vorticities. So, we consider energy when calculating weight. Both the classical and relativistic velocities have an average vorticity of,

$$< \omega_{xz} > \;\; = \;\; \frac{\sum \epsilon_{ij} \omega_{xz}^{ij}}{\sum \epsilon_{ij}} \tag{2.5}$$

The energy density of the cells on the $x - z$ plane is represented by the $\epsilon_{i,j}$, where i stands for the x coordinate and j for the z coordinate. The thermal vorticity, in addition to the kinetic vorticity, is crucial in heavy ion collisions. It is intimately connected to the particle polarisation. The thermal vorticity is defined by,

$$\omega_{\mu\nu}^T \;\; = \;\; \frac{1}{2}(\partial_\nu \beta_\mu - \partial_\mu \beta_\nu) \tag{2.6}$$

In this case, $\beta_\mu = \frac{u_\mu}{T}$. Here, T is the local temperature. The energy is used as the weight factor to extract $< \omega_{\mu\nu}^T >$. The local vorticity changes as the velocity distribution does

as it is dependent on the velocity field at a specific moment. The average vorticities are obtained and their relationships to collision energy are plotted.

2.3 Coefficient of Shear viscosity

As previously stated, shear viscosity plays a significant role in viscous flows. The coefficient of shear viscosity can be obtained from the hadron resonance gas models. The thermodynamic potential in these models is represented by,

$$log(Z, \beta, \mu_B) = \int dm(\rho_b(m) log Z_b(\beta, \mu_B) + (\rho_f(m) log Z_f(\beta, \mu_B)) \tag{2.7}$$

Here, the hadronic gas occupies volume V at chemical potential μ_B and temperature β^{-1}. The partition functions of bosons and fermions with mass m are Z_b and Z_f, respectively, and the densities of the bosons and fermions are ρ_b and ρ_f. For low temperatures, these models exhibit an excellent agreement with lattice QCD predictions. This has been shown in a number of models, including the Nambu-Jona-Lasinio model [15], the quasi particle model [16], and the chiral perturbation theory [17]. The viscosity co-efficients of the hadron resonance gas model were recently generalised by Kadam and Mishra to include finite chemical potential effects [18]. They suggest that the shear viscosity is determined by,

$$\eta = \frac{5}{64\sqrt{8}r^2} \Sigma_i < |p| > \frac{n_i}{n} \tag{2.8}$$

Here, r is the radius of the particles in question, and n_i is the number density of the i-th particle. We can distinguish between the various particles generated in the AMPT simulations. We determine the shear viscosity for the neutrons and the protons separately rather than taking all the particles. Additionally, we independently determine the shear viscosity of various other particles, such as pions and Λ hyperons. The general characteristics of the shear viscosity change are the same for all of the different particles. Since the quantity of particles varies greatly, the only difference is the magnitude. The most widely studied transport coefficient in heavy ion collisions is the coefficient of shear viscosity. It may have effects on the elliptic flow velocity because it is largely responsible for stabilizing the momentum anisotropy. We examine the elliptic flow velocity at various collision energies. The change in shear viscosity will be reflected in the elliptic flow velocity. Shear viscosity and its relationship with other transport coefficients play a significant impact here, as we can see from the earlier studies [19].

At various collision energies, the coefficient of shear viscosity is obtained. The chemical potential can be associated to the various collision energies. It is possible to parameterize

the energy dependence of the baryon chemical potential by the relation [10],

$$\mu_B(\sqrt{s}) = \frac{d}{(1 + e\sqrt{s})} \tag{2.9}$$

having $e = 0.273 \pm 0.008\ GeV^{-1}$ and $d = 1.308 \pm 0.028\ GeV$. This parameterization is built on observations from numerous groups across a wide range of energies. Since we are not utilising this equation to fit any data, we believe it to be adequate for our needs. Understanding how viscous stress contributes to the formation of vorticity patterns in the partonic fluid is our primary motivation. This will mostly include a qualitative explanation rather than a quantitative one of the relationship between the collision energy and the baryon chemical potential.

There have been other studies of shear viscosities which have been used to show the dependence of viscosity on the baryon chemical potential (μ_B). However, in these cases, μ_B is an input parameter [21]. It is difficult to calculate the chemical potential μ_B, unless we use Eq. 2.9. Since as mentioned before the relationship between the collision energy and the baryon chemical potential is not so rigorous, we prefer to calculate the viscosity coefficient from the particle velocities. The particle velocities for the individual particles are easily available as an output of the AMPT model.

2.4 Simulations

We employ the free open source AMPT model [22], to generate our initial condition. This model has been widely used to look into different heavy ion collision transport properties [23]. The choice of this model was made since it includes both the hadronic and partonic phases. Both the hadronic and partonic aspects of the particle flow's vorticity are of importance to us. Along with the default version, the AMPT model also features a string melting (SM) version. After studying both variants, only the SM version's results have been presented. The settings that we employ in our computations have already been applied to the AMPT model to investigate the vorticity in the $(x-\eta)$ plane [1]. The parameters were employed in a study that successfully replicated the yields, transverse momentum spectra, and elliptic flow for low-p_T pions and kaons in central and mid-central $Au + Au$ collisions at collision energies of 200 GeV [24]. We get the data from the AMPT and construct a velocity field since we are interested in the implications of vorticity. This is achieved by selecting an acceptable volume and segmenting it into smaller cells. Each cell then constitutes a volume of fluid, and the fluid's average momentum is determined by the mean momentum of the particles within each cell. As a result, the velocity field across the selected volume is smooth.

In ref. [1, 13], this approach of determining vorticity from AMPT has been applied previously. We created 10^4 events to obtain the results for each collision energy.

We focus on the partonic phase first. In the AMPT model, the incoming nucleus is centred at $x = b/2 > 0 (x = -b/2 < 0)$ for positive (negative) longitudinal momentum where b in the impact parameter. The impact parameter axis is the x-axis and the beam axis is the z-axis. This indicates that the y-direction is primarily where the initial total angular momentum is concentrated. As previously stated, this is the reason we are just focusing on the angular momentum component in the reaction plane. Thousands of particles are produced by an event in the AMPT simulation, but this number is insufficient to produce a smooth momentum distribution. A smooth distribution is crucial to us since we want to calculate the vorticity. We must produce a huge number of events with the same parameters in order to calculate an average.

The grid or cell size is yet another critical component of our simulation. We must select the cell size so that there are a lot of particles inside each cell. We start our analysis with a fixed impact parameter of $b = 7$ fm and a cell size of 0.5 fm in each direction. The average momentum and energy for each cell is calculated, and then the velocity is obtained from these two quantities by $\frac{\langle \vec{p} \rangle}{\langle \epsilon \rangle}$. Reference [1] employed a similar approach.

2.5 Results and Discussion

2.5.1 The initial partonic stage

We measured the vorticity patterns in the reaction plane $(x - z)$ at collision energies ranging from 20 GeV to 200 GeV. We analyse the vorticity patterns at $t = 1$ fm/c. We pick this instant because it was demonstrated in [1] that the averaged vorticity peaked about this time. To demonstrate the differences in the patterns in the low energy collisions, we provide a few vorticity patterns in this collision energy range. Fig. 2.1 and Fig. 2.2 represent the vorticity patterns at 200 GeV and 100 GeV, respectively. The vorticity in both plots ranges from -0.06 to 0.08. But as we can see, the vortex lines show distinct contours surrounding the developed vortices. The vorticity pattern at 20 GeV is shown in Fig. 2.3. In comparison to the previous two figures, the contours are much more evenly spread out here.

According to equation 2.9, the chemical potential μ_B rises as $\sqrt{s_{NN}}$ decreases. If the angular momentum is larger, the vorticity that forms has a tendency to be circular. The vortices have a tendency to spread out and take on an oval shape when the strain resulting from the bulk viscous pressure around the fluid grows. Although one should

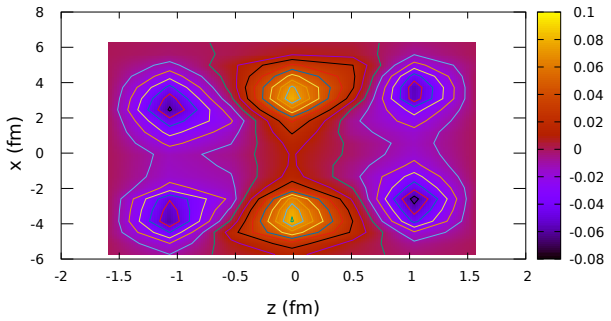

FIGURE 2.1: Vorticity distribution in the reaction $(x - z)$ plane at a collision energy of 200 GeV for partons according to the non-relativistic definition of vorticity. Both x and z axes are in units of fm

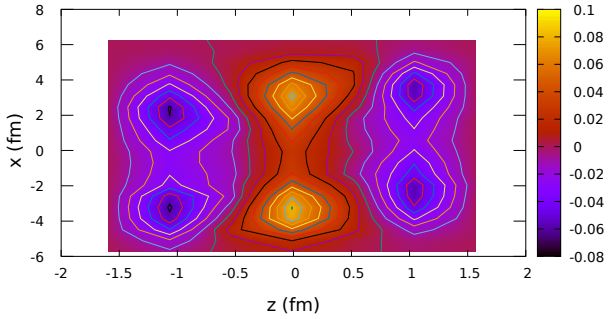

FIGURE 2.2: Vorticity distribution in the reaction $(x - z)$ plane at a collision energy of 100 GeV for partons according to the non-relativistic definition of vorticity.

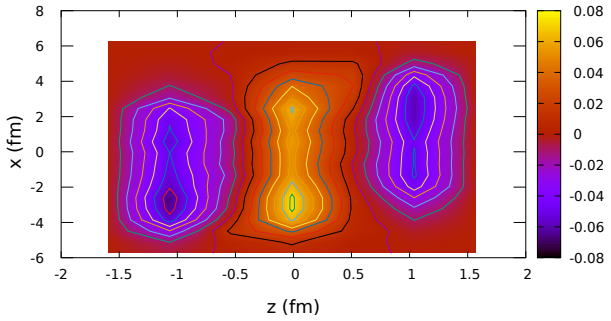

FIGURE 2.3: Vorticity distribution in the reaction $(x - z)$ plane at a collision energy of 20 GeV for partons according to the non-relativistic definition of vorticity.

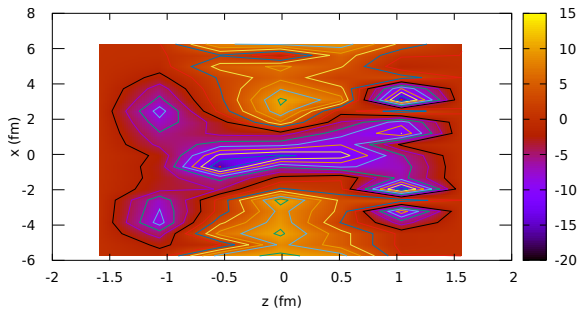

FIGURE 2.4: Kinetic vorticity distribution in the reaction $(x-z)$ plane at an collision energy of 200 GeV for relativistic partons.

be cautious when drawing inferences about angular momentum from the vorticity plots even though the vorticity is meant to be proportional to it. Though the vorticity drops with increasing $\sqrt{s_{NN}}$, it has been demonstrated in [12] that the angular momentum increases with increasing $\sqrt{s_{NN}}$. The moment of inertia is what causes this mismatch. According to [1], the moment of inertia is what largely determines how much angular momentum is there. As a result, it seems that the vorticity and angular momentum are inversely related. We find very low vorticity values at nearly $x = 0$ and $z = 0$. This is comparable to earlier vorticity research by [1] and [12]. In the regions of lower and higher rapidity, the distribution pattern of vorticity reveals a flipping of the vorticity direction. Csernai et al. [27] observed flipping of the vorticity in the $x-z$ plane, at finite rapidities at later times $t = 3.56 fm/c$ after QGP formation. Their data show that the vorticity has far larger fluctuations at later time. The underlying radial velocity profile and the vorticity profile significantly differ, as can be seen in ref. [1] (Fig. 6 and 10). This indicates that the angular momentum in the low and high rapidity regions may not have changed directions only because the vorticity's sign has changed. We observe a similar decrease in magnitude in the vorticity displayed in the $(x-y)$ plane in a recent work, ref. [26]. In our analysis, we only considered the magnitude of vorticity. In regions of finite rapidity, the magnitude of the vorticity decreases and goes to negative values, but because the moment of inertia is high in these regions, the angular momentum may still be positive. Our vorticity patterns cannot be used to interpret the angular momentum distribution since the moment of inertia has never been taken into account in our computations.

The same energies are then analyzed for the relativistic vorticity. The patterns of the relativistic vorticity are shown in Figures 2.4, 2.5 and 2.6 for the values of $\sqrt{s_{NN}}$ = 200, 100, and 20 accordingly. The relativistic γ factor causes the values of the vorticity to be significantly greater than the vorticity obtained previously. The relativistic γ factor is typically of the order of 10^2 as the particles move at speeds close to the speed of light.

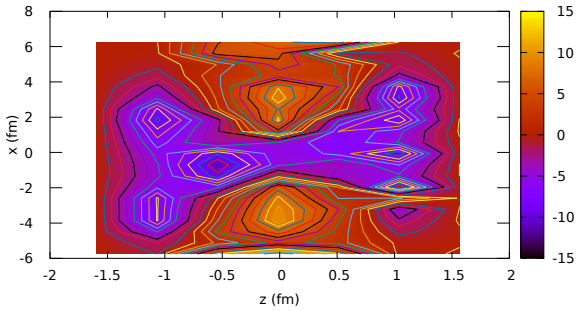

FIGURE 2.5: Kinetic vorticity distribution in the reaction $(x - z)$ plane at a collision energy of 100 GeV for relativistic partons.

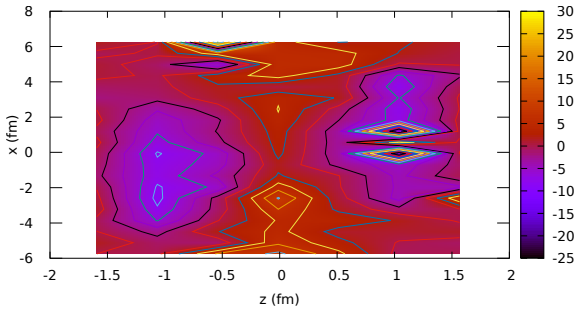

FIGURE 2.6: Kinetic vorticity distribution in the reaction $(x - z)$ plane at a collision energy of 20 GeV for relativistic partons.

The vorticity patterns are broadly similar, but there are also a number of differences. The centre of the pattern is where the greatest significant difference may be seen. The differences are more pronounced at lower collision energy. The relativistic vorticity is what causes the fluctuations to be more in this context. Similar results are shown in ref. [27] for different condition. Larger velocities result in bigger velocity fluctuations. Next, we display some patterns for the thermal vorticity for the same $\sqrt{s_{NN}}$ values in Fig. 2.7, 2.8 and 2.9. To examine the spin-polarisation of the particles, thermal vorticity is essential. As we move to lower and lower collision energy, we notice that the vorticity spreads out in all of the cases. Therefore, it can be inferred that the vorticity pattern becomes increasingly diffuse as collision energies decrease.

The non-relativistic pattern and the relativistic pattern differ in a few areas. At larger collision energy in the non-relativistic case, the core region has nearly zero vorticity. The core region has significant fluctuations and finite vorticity in the relativistic case. This occurs for collisions with higher energies. The relativistic and non-relativistic patterns appear to be comparable for the collision energy of 20 GeV, but they have substantially different magnitudes, with the relativistic one having significantly more

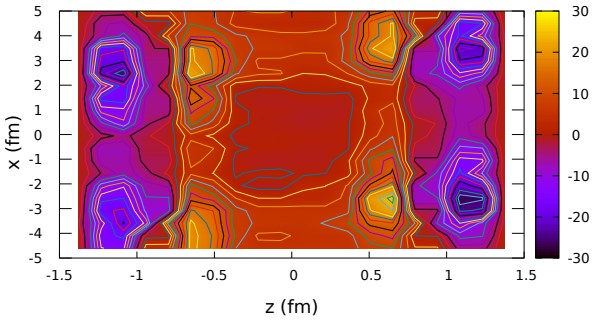

FIGURE 2.7: Thermal vorticity distribution in the reaction $(x-z)$ plane at a collision energy of 200 GeV for partons.

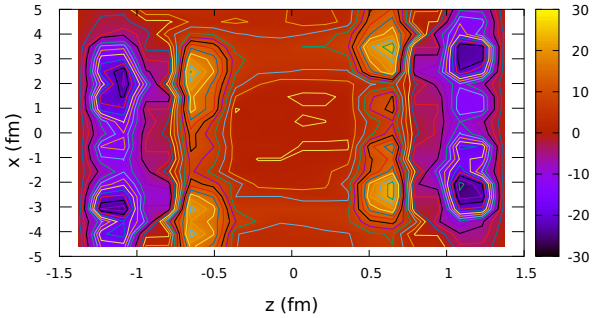

FIGURE 2.8: Thermal vorticity distribution in the reaction $(x-z)$ plane at a collision energy of 100 GeV for partons.

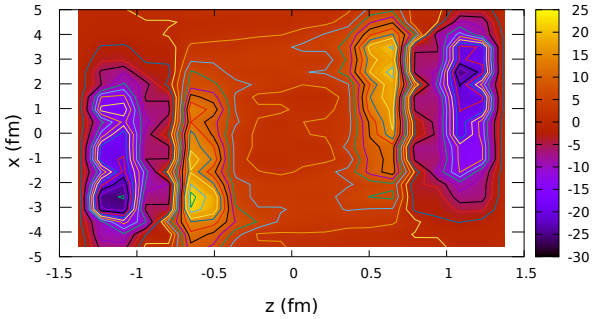

FIGURE 2.9: Thermal vorticity distribution in the reaction $(x-z)$ plane at a collision energy of 20 GeV for partons.

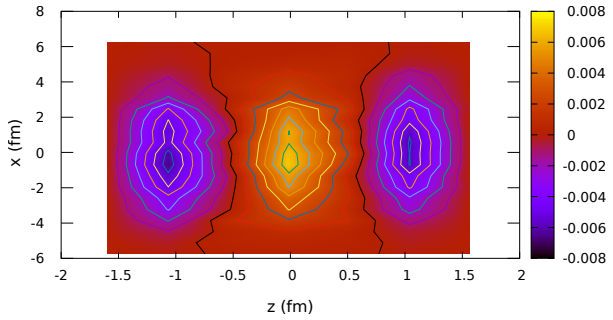

FIGURE 2.10: Vorticity distribution in the reaction $(x-z)$ plane at a collision energy of 200 GeV for the hadronic phase

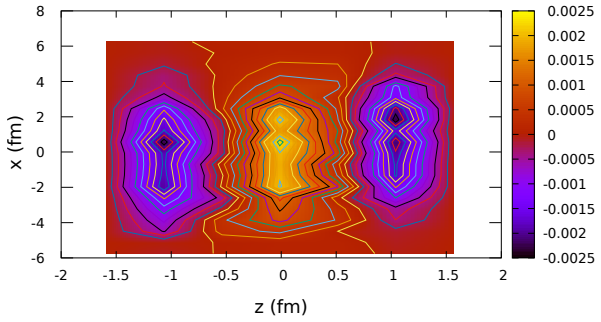

FIGURE 2.11: Vorticity distribution in the reaction $(x-z)$ plane at a collision energy of 20 GeV for the hadronic phase

fluctuations than the non-relativistic one. The patterns for the thermal vorticity are similar to those in the non-relativistic situation, but there are more fluctuations. Due to the wider range of velocities, even little deviations in velocities cause fluctuations to rise. The general pattern, however, that the vortices are diffused with lower collision energies is also evident in this instance.

2.5.2 The final hadronic stage

The net vorticity is less in the hadronic stage than in the partonic stage. Given that the initial fireball made up of partons has a higher angular momentum, this is to be expected. After the partons stop interacting, the hadronization takes place using a quark coalescence model in SM version of AMPT model. Although the three momenta are conserved, hadrons will be heavier than partons. As a result, the hadrons' net vorticity decreases.

Compared to the vorticity patterns for the partons, the vorticity pattern that we see here is spread out at $\sqrt{s_{NN}} = 200$ GeV (Fig. 2.10). Although the spread at 20 GeV(Fig.

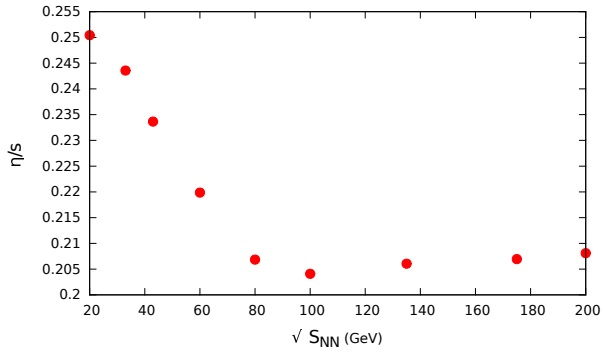

FIGURE 2.12: The specific shear viscosity at different collision energies for neutrons, protons and their antiparticles.

2.11) and at 200 GeV differ from one another, the difference is not as noticeable as it is at the partonic stage. However, the vorticity's size has significantly reduced. The fluctuations are quite enormous and there is no recognizable regularity in the relativistic situation.

2.5.3 Shear viscosity dependence on the collision energy

It has been observed in the past that the shear viscosity affects the vorticity patterns in relativistic heavy ion collisions [27]. With rising baryon chemical potential, the specific shear viscosity usually stays constant. For different collision energies we determine and plot the coefficient of shear viscosity. We employ the shear viscosity in the equation 2.8. Despite the fact that it is mentioned across all particles, we perform the calculations separately for different particles. As the right-hand side is a summation, unless the magnitude differ significantly from one another, the average over all of the particles would be of the same order as the individual particles. We determine the specific shear viscosity for neutrons, protons, and pions. When determining the magnitude of the viscosity, the particle's radius is essential. We use the particle data book's standard radius information. The viscosity of neutrons and protons is depicted in Figure 2.12. Using the values of r based on the limits provided by the particle data group, we find that the general nature of the graph and the order of magnitude stay the same. The specific shear viscosity has also been studied in ref.[28]. While we used the definition from the HRG models, they used the kinetic definition of shear viscosity. They have analyzed it for higher temperatures than we have, despite the fact that their overall tendency is fairly similar to ours and ours is for lower temperatures.

The graph (Fig. 2.12) shows that at lower collision energies, which relate to higher baryon chemical potentials, the specific shear viscosity is at its maximum. Beyond 80

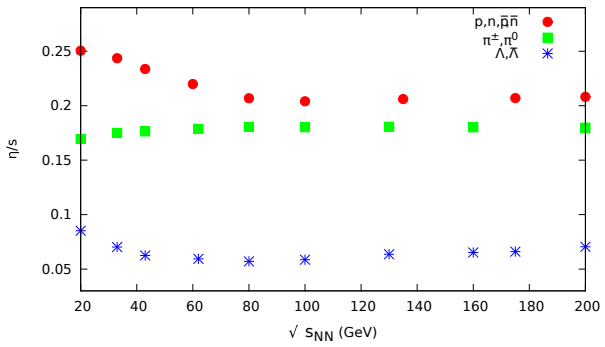

FIGURE 2.13: The specific shear viscosity at different collision energies for neutrons and protons, pions, Λ hyperons and their antiparticles.

GeV, it becomes almost constant. The viscosity coefficient for pions and Λ hyperons is also plotted in Fig. 2.13, which further illustrates this.

The pions exhibit a distinct trend compared to the neutron, protons, and Λ hyperons, as is evident. Because more pions are created than neutrons, protons, and Λ hyperons at all energies. At lower collision energies, the generated pions also differ by an order of magnitude compared to higher collision energies. This is not noticed in other particles. The number of neutrons, protons, and Λ hyperons largely stays the same over the spectrum of collision energy we have observed. Due to this, the shear viscosity of pions below 80 GeV changes very little, whereas that of neutrons, protons and Λ hyperons show a slightly higher change. The sensitivity of η/s to baryon chemical potential has been discussed in earlier works [29]. It is predicted that the physical value of η/s should rise at lower collision energy because it depends on chemical potential and has a minimum at zero chemical potential. The effective value of shear viscosity employed to characterise the experimental data at various collision energies is shown in Figure No. 12 of ref. [29]. At decreasing collision energy, the shear viscosity's uncertainty rises. Additionally, as described in [30, 31], the negative bulk viscous pressure in the expanding fireball suppresses the grow of the radial flow. Elliptic flow and higher flow harmonics are typically suppressed by viscosity. It has already been demonstrated that the composition of the hadronic fireball has a significant impact on how the total momentum anisotropy is distributed across the various hadrons. The viscosity from the HRG model also relies on the momentum distribution of the various hadrons. In fact, this distribution heavily depends on the pion elliptic flow at freeze-out temperature. Although we have not done it yet, we intend to thoroughly study this.

We are aware that viscous strains cause vorticity to spread across the fluid. Therefore, the spreading out of the vorticity patterns suggests that for low collision energies and high baryon chemical potential, the bulk viscous pressure contributes more to the viscous

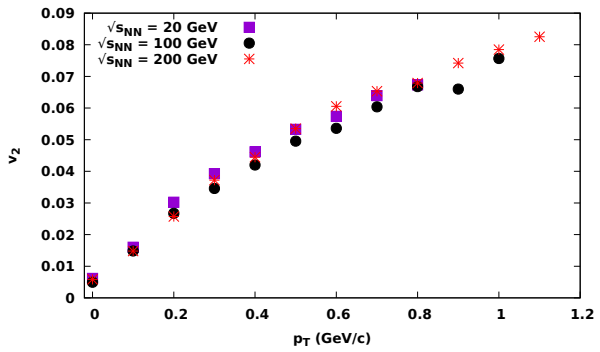

FIGURE 2.14: Change of v_2 with p_T for different collision energies

diffusion of the vortices. We also examine the impact of lower $\sqrt{s_{NN}}$ on the elliptic flow to better comprehend this.

2.5.4 The elliptic flow

From earlier studies, it is widely recognized that the elliptic flow is a reliable indicator of shear viscosities [32]. In comparison to an ideal fluid, the elliptic flow is suppressed in a viscous non-ideal fluid. We derive the elliptic flow from the hadronic data and compare it to the publically available data from the STAR collaboration [33] since we are analysing how collision energy affects shear viscosities.

We obtain elliptic flow by using the following equation.

$$v_2 = \frac{\langle p_x^2 - p_y^2 \rangle}{\langle p_x^2 + p_y^2 \rangle} \tag{2.10}$$

It is widely known that the elliptic flow (v_2) depends on the transverse momentum (p_T). We plot the v_2 vs. p_T for several different collision energies since we are curious to know if the nature of the elliptic flow varies with change in $\sqrt{s_{NN}}$. The graphs representing the range of collision energies that we have examined are shown in Fig. 2.14. We observe that at lower p_T, the overall p_T suppression is greater for lower collision energies, however the higher p_T range does not allow for the drawing of such a conclusion. In ref. [28], a more thorough investigation of the flow coefficients was conducted. Our results are in agreement with their results for the range value that we have tested. They have also estimated the higher harmonics at high p_T and high $\sqrt{s_{NN}}$ but we are more focused in the vorticity distribution.

For a collision energy of 19.6 GeV, we also plot v_2 vs. p_T. The STAR collaboration has published data for v_2 vs. p_T. In Fig. 2.15, we present this data along with our own estimate of v_2 vs. p_T for 19.6 GeV. The elliptic flow results from the AMPT simulations

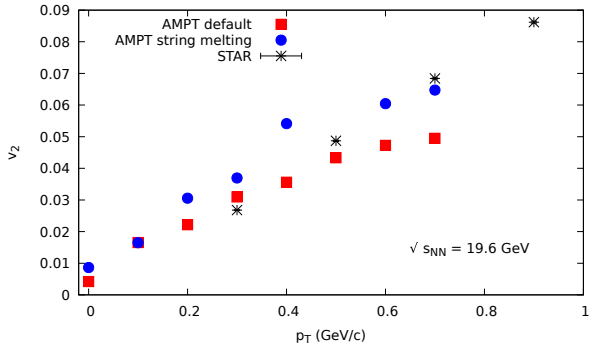

FIGURE 2.15: v_2 with p_T at 19.6 GeV from the simulation and from data from the STAR collaboration. The data is for the 20%-30% centrality of charged particles.

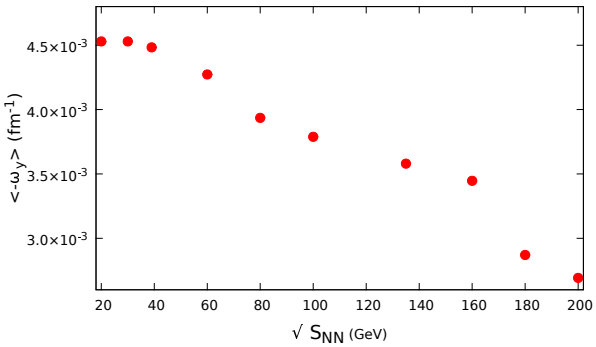

FIGURE 2.16: Average vorticity $\langle\omega_{xz}\rangle \equiv \langle\omega_y\rangle$ at different collision energies ($\sqrt{s_{NN}}$) at a fixed impact parameter of $b = 7$ fm

seem to be rather close to the data produced by the STAR collaborations at a higher range of p_T. Although recent study has indicated that there may be changes when light nuclei are considered, there did not seem to be a major difference between the various hadrons and mesons in the collision energy ranges we have considered [34].

The v_2 vs. p_T graph does not significantly change for $\sqrt{s_{NN}}$ between 7.7 GeV and 39 GeV, according to the STAR data. Collision energies are higher in our simulation. The v_2 vs. p_T plot, even for 200 GeV, does not differ noticeably from the 20 GeV plot. Therefore, shear viscosity does not vary considerably when the baryon chemical potential increases, even if shear viscosity does play a significant part in creating the elliptic flow. This seems to be consistent with our plot of $\frac{\eta}{s}$ vs $\sqrt{s_{NN}}$.

2.5.5 Average vorticity dependence on the collision energy

Our final results indicate how the average vorticity depends on collision energy. At various collision energies, we determine the average vorticity indicated by $\langle\omega_{xz}\rangle$.

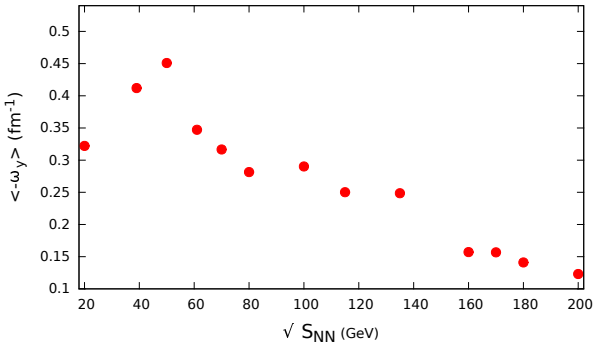

FIGURE 2.17: Average vorticity $\langle\omega_{xz}\rangle \equiv \langle\omega_y\rangle$ with the relativistic definition of velocities, at different collision energies ($\sqrt{s_{NN}}$) at a fixed impact parameter of $b = 7$ fm

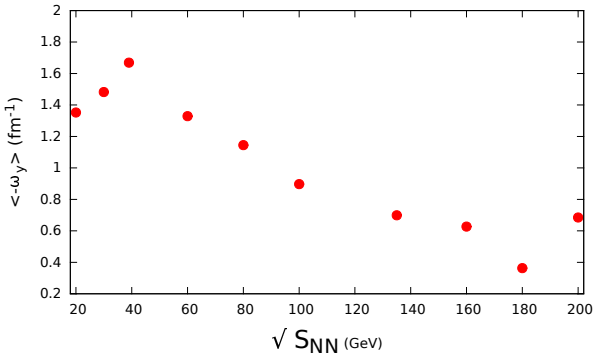

FIGURE 2.18: Average thermal vorticity $\langle\omega_{xz}\rangle \equiv \langle\omega_y\rangle$ at different collision energies ($\sqrt{s_{NN}}$) at a fixed impact parameter of $b = 7$ fm

We find that when collision energy increases, the average kinetic vorticity drops (Fig. 2.16). Our vorticity results appear to be in agreement with ref.[12]. The thermal and relativistic vorticities give similar plots (Fig. 2.17, 2.18). The vorticity pattern exhibits significant fluctuations in the relativistic scenario, calculating the average velocity is therefore very challenging.

However, we have made an effort to compile averages throughout the same span of collision energy. We can draw the same conclusions as before because the overall nature is unchanged from the non-relativistic situation. The average vorticity has a slight decrease below 40 GeV, which is the sole variation for the thermal and relativistic cases that can be seen.

At $\sqrt{s_{NN}}$ greater than 50 GeV, the average vorticity has been studied as a function of $\sqrt{s_{NN}}$ [12]. The moment of inertia is the main factor in the calculation of the average vorticity. It is responsible for the average vorticity to decrease gradually even while the angular momentum increases. The average vorticity is therefore trending in the opposite direction from angular momentum. Our findings appear to suggest that at lower energy,

angular momentum can also play a substantial role. This will result in the dip that is seen below 40 GeV. We do not believe that the pattern, which is highly noticeable in both thermal and relativistic vorticities, is purely the result of fluctuations. Although fluctuations do have an impact, the clear pattern suggests that a closer examination of the experiment results at lower collision energy is required.

Our graphs show that lower collision energies are better for studying the evolution of the vorticity pattern because there, both kinetic and thermal vorticity average values are higher. When compared to the change in the vorticity patterns, the change in shear viscosity is quite minor. Therefore, it appears that further research on bulk viscosity is necessary.

2.6 Summary

We have used a hybrid transport model to conduct an in-depth study of viscous effects on vorticity patterns at various collision energies. We studied the viscous effects and vorticity structures at lower collision energy. A finite baryon chemical potential is one of the reasons why lower collision energy are investigated experimentally. At finite baryon chemical potentials, the quark-gluon plasma has been modelled using hadron resonance gas models. We are curious to see if these models can explain the vorticity patterns identified using the hybrid transport models. The coefficient of shear viscosity serves as our link between these two vastly dissimilar models.

We have analysed two definitions of vorticity, the kinetic vorticity and the thermal vorticity. We show that the local vorticity patterns are circular and clearly characterised at high collision energy. They seem stretched and elliptical at lower collision energy. The chemical potential is large at lower collision energies, which causes the viscous tension to be high as well. These results are shown in the figures as stretched elliptical vortices. It's interesting to note that the local vorticity has significantly more fluctuations in the relativistic situation, and the patterns during collisions with greater energies differ between the classical and the relativistic cases. The classical and relativistic cases, however, exhibit comparable patterns at lower impact energies but with differing magnitudes.

To get the average vorticity at various collision energies, we weighted the vorticity. We observe that when collision energies increase, the average vorticity decreases. The change in average vorticity with increasing collision energy is opposite to the change in angular momentum. Although it is anticipated that angular momentum may cause vorticity, it appears that other factors dominate the average vorticity at high collision energies. However, for relativistic and thermal vorticity, there is a dip at lower collision energies.

Another significant result is the estimation of the coefficient of shear viscosity. We estimated the results at various collision energies using the shear viscosity definition from the HRG models. The particle momentum affects the coefficient of shear viscosity. When we change the collision energy, we observe that the change in shear viscosity is very small at higher collision energies. At lower collision energies, there is a sharp change, but after that, the change is stagnant. The study of elliptic flow, which is connected to the fluid's shear viscosity, also leads to the same result. We see that the elliptic flow is suppressed at low collision energies, suggesting the effects of viscosity. This is also evident by the analysis of the STAR data. All these indicate that both angular momentum, viscosity, and inertia of the fluid play significant roles in the generation of vorticity in heavy ion collision plasma.

Additionally, we are aware that at these velocities, the Reynolds number is exceedingly high. As a result, many elements of viscous flow, especially whether or not turbulence emerges, remain unclear based on our simulations. We will analyse these and other possibilities in the next chapter in order to comprehend the characteristics of the viscous quark gluon plasma produced in heavy ion collisions. We anticipate that this research will direct additional study on the vorticity patterns at lower collision energies. This could help us understand the transport characteristics of the QGP at finite chemical potentials.

Bibliography

[1] Yin Jiang, Zi-Wei Lin, and Jinfeng Liao, Phys. Rev. C **94**, 044910 (2016).

[2] D. E. Kharzeev, L. D. McLerran, and H. J. Warringa, Nucl. Phys. A **803**, 227 (2008).K. Fukushima, D. E. Kharzeev, and H. J. Warringa, Phys. Rev. D **78**, 074033 (2008).

[3] N. Banerjee, J. Bhattacharya, S. Bhattacharyya, S. Dutta, R.Loganayagam, and P. Surówka, J. High Energy Phys. **01** 094 (2011); D. T. Son and P. Surowka, Phys. Rev. Lett. **103**, 191601 (2009).

[4] B. I. Abelev et al. (STAR Collaboration), Phys. Rev. Lett. **103**, 251601 (2009); B. I. Abelev et al. (STAR Collaboration), Phys. Rev. C **81**, 054908 (2010); G. Wang (STAR Collaboration), Nucl. Phys. A **904-905**, 248c (2013); L. Adamczyk et al. (STAR Collaboration), Phys. Rev. Lett. **113**, 052302 (2014); L. Adamczyk et al. (STAR Collaboration), Phys. Rev. Lett. **114**, 252302 (2015).

[5] B. Abelev et al. (ALICE Collaboration), Phys. Rev. Lett. **110**, 012301 (2013); J. Adam et al. (ALICE Collaboration), Phys. Rev. C **93**, 044903 (2016).

[6] Y.Xie, R.C.Glastad and L.P.Csernai, Phys.Rev.C **92**, 064901 (2015); Y. L. Xie, M. Bleicher, H. Stöcker, D. J. Wang and L. P. Csernai, Phys.Rev.C **94**, 054907 (2016) ; Y.Xie, Dujuan Wang and L.P. Csernai, Phys. Rev. C **95**, 031901(R) (2017).

[7] F. Becattini, L. P. Csernai, and D. J. Wang, Phys. Rev. C **88**, 034905 (2013); F.Becattini, I.Karpenko, M.Lisa, I.Upsal and S.Voloshin, Phys.Rev. C **95**, 054902 (2017); I.Karpenko and F. Becattini, Eur.Phys.J.C **77**, no.4, 213 (2017); I.Karpenko and F.Becattini, J.Phys.Conf.Ser. **779**, no.1, 012068 (2017).

[8] P. Romatschke and U. Romatschke, Phys. Rev. Lett. **99**, 172301 (2007); R. Baier, P. Romatschke, and U. Wiedemann, Nucl. Phys.A **782**, 313 (2007); R. Baier and P. Romatschke, Eur. Phys.J. C **51**, 677 (2007).

[9] F. Becattini et. al, Eur. Phys. J. C **75**, 406 (2015).

[10] Song, H., Bass, S. A., Heinz, U., Hirano, T., and Shen, C. Phys. Rev. Lett., **106** (19), 192301 (2011);

[11] H Song, S A Bass, U Heinz, T Hirano and C Shen, Phys. Rev. C **83**, 054910 (2011); Erratum, ibid. C **86**, 059903 (2012); Chun Shen, Zhi Qiu, Huichao Song, J. Bernhard, S. Bass, U. Heinz, Comput. Phys. Commun. **199**, 61-85 (2016).

[12] Wei-Tian Deng and Xu-Guang Huang, Phys. Rev. C **93**, 064907 (2016).

[13] B.Singh, J. R. Bhatt and H. Mishra, Phys. Rev. D **100**, 014016 (2019).

[14] L. P. Csernai, V. K. Magas, and D. J. Wang, Phys. Rev. C **87**, 034906 (2013).

[15] C. Sasaki, K. Redlich, Nucl. Phys. A **832**, 62 (2010).

[16] C. Sasaki, K. Redlich, Phys. Rev. C **79**, 055207 (2009).

[17] A. Dobado, J.M. Torres-Rincon, Phys. Rev. D **86**, 074021 (2012).

[18] G.P. Kadam and H. Mishra, Nucl. Phys. A **934**, 133-147 (2015).

[19] T. Schäfer and D. Teaney, Rep. Prog. Phys. **72**, 126001 (2009).

[20] J. Cleymans, H. Oeschler, K. Redlich, S. Wheaton, Phys. Rev. C **73**, 034905 (2006).

[21] J. Xu and C. M. Ko, Phys. Rev. C **83**, 034904 (2011).

[22] Z. W. Lin, C.M. Ko, Bao-An Li, B. Zhang and S. Pal Physical Review C **72** 064901 (2005); L.-W. Chen, V. Greco, C.-M. Ko, and P. F. Kolb, Phys. Lett. B **605**, 95 (2005).

[23] Yifeng Sun, Che Ming Ko, and Feng Li, Physical Review C **94**, 045204 (2016).

[24] Z. W. Lin, Phys. Rev. C **90**, 014904 (2014).

[25] Li, H., Pang, L. G., Wang, Q., and Xia, X. L., Phys. Rev. C **96**, 054908 (2017).

[26] De-Xian Wei,Wei-Tian Deng and Xu-Guang Huang, Phys. Rev. C **99**, 014905 (2019).

[27] Becattini, F., Inghirami, G., Rolando, V. et al. Eur. Phys. J. C **75**, 406 (2015).

[28] D. Solanki, P.Sorensen, S. Basu, R. Raniwala and T.K Nayak, Phys.Lett. B **720**, 352-357 (2013).

[29] I. A. Karpenko, P. Huovinen, H. Petersen and M. Bleicher, Phys. Rev. C **91**, 064901 (2015).

[30] H. Song and U. Heinz, Phys. Rev. C **81**, 024905 (2010).

[31] T. Schafer, Annual Review of Nuclear and Particle Science **64**, 125-148, (2014).

[32] H. Song, U. W. Heinz, J. Phys. G **36**, 064033, (2009).

[33] L. Adamczyk et al. (STAR Collaboration), Phys. Rev. C **86**, 054908 (2012).

[34] X. Gong (PHENIX collaboration) J. Phys. G **38**,124146 (2012); Md. Rihan Haque, C. Jena, and B. Mohanty, Advances in High Energy Physics **2017**, Article ID 1248563, (2017).

Chapter 3

Anisotropic turbulence in relativistic plasmas

3.1 Introduction

There are a significant amount of fluctuations present in the initial stages after the heavy ion collision. These fluctuations can be produced at various length scales. There are number density fluctuations, energy density fluctuations, temperature fluctuations, and several other types of fluctuations [2]. These fluctuations can develop irregularities in the flow. There are various origins for the creation of these fluctuations. The authors of reference [2–4] have demonstrated how the chromo-Weibel instability can develop in the QGP in the existence of a momentum anisotropy. Because of the presence of momentum anisotropy, the Weibel instability can be observed in plasma that is homogeneous or nearly homogeneous. The electromagnetic fluctuation of two beams that are moving opposite to one another can potentially induce this instability. The production of turbulent color fields in relativistic plasma is addressed in ref [5, 6]. In reference [7], the development of turbulence and its dependency on fluctuations have also been explored. Here, the authors relate a set of re-scaled coordinates for a non-relativistic Navier Stokes equation to the relativistic dynamics of fluctuations. As a result, the authors were able to characterize the flow in the relativistic heavy ion collision using the principles of non-relativistic turbulence. The authors suggested that the Kolmogorov spectrum for the correlation functions in the relativistic heavy ion system may not be anticipated, but the emergence of turbulence can lead to a power law behavior similar to that obtained for non-relativistic systems.

In heavy ion collision experiments, the collective dynamics of the produced particles indicate the system's fluid nature. There are models based on the hydrodynamic equations that can effectively represent the outcomes of these experiments. At the LHC and RHIC, we observe similarities in the pattern of elliptic flows and other higher-order collective flows, which is in line with the predictions of the viscous hydrodynamic models [8–14]. In reality, as shown in ref. [15–18], the ideal fluid dynamics can also explain the experimental results quite well. Because of the low shear viscosity to entropy density ratio η/s, the fluid generated is regarded as the most ideal fluid. The value of $\eta/s \approx \frac{1}{8\pi}$ was adversely addressed by the RHIC data from the top energies [19, 20].

The transition from the initial state to the equilibrium state is an intriguing area of study. The system seeks to attain thermal equilibrium as it evolves. The system expands during this process, and the temperature of the system drops over time until equilibrium is established. A lot of energy is dissipated in the system. As was already said, the QGP's collective behavior points to the system's fluid dynamics. The flow instabilities may cause the plasma to behave like a turbulent flow. By examining the energy dissipation spectrum of the turbulent system, it is possible to comprehend that the energy dissipation can occur at various turbulent flow length scales. By studying the temperature and velocity distribution in the collision region, we are interested in analyzing the spectra of the initial instabilities. We only examine temperature fluctuations in the pre-equilibrium stage, where the temperature can be described using the energy density, and one can assume the local thermal equilibrium in the corresponding length scales.

Both the transport models and the kinetic theory models are capable of describing collective flows. The final stage hadron scatterings are also incorporated in some transport models, which provides a more favorable fit to the data [21, 22]. One such kinetic theory-based model that is effective in simulating experimentally observed collective flows is the AMPT model [23]. The details about this model is already discussed in Chapter I. In this work, we analyze the fluid turbulence anisotropies in the initial and pre-equilibrium stages of the heavy ion collision using the AMPT model. Here, the state of the system immediately following the collision and prior to parton scattering is referred to as the initial stage. Pre-equilibrium stage refers to the system's condition following parton scattering but before it reaches an equilibrium state. Since we are employing a grid-based simulation, the local thermal equilibrium is assumed at the length-scales determined by the grid size in the pre-equilibrium stage.

Section 2 describes the general overview of the turbulence spectra for the heavy ion collision system. Section 3 discusses the formulation of the turbulence energy spectra and the length scales of the system. Here we have shown the range of eddies we can get and the range of wave numbers associated with the eddy sizes. We display the outcomes of the numerical simulations in section 4. We have presented the longitudinal and transverse energy spectra at various initial conditions. We discuss the power spectrum of temperature fluctuations obtained for the turbulent system in section 5. In section 6, we present a summary of the results.

3.1.1 Spectral analysis for heavy ion collision system

The geometry of a heavy ion collision is such that a significant amount of angular momentum is produced in the system. In the early stages of the plasma, this angular momentum may cause the formation of vortices [24–27]. A substantial proportion of the incoming nuclei energy is carried by these vortices. Thus, a turbulent flow may develop. The fluid in a turbulent flow consists of continuously interacting swirls forming eddies or vortices. The size of these eddies can vary. Their length scales can range from as little as the size of the nuclei to as large as meters at times. Turbulence is characterized as instabilities in the velocity field in a laminar flow. The field of instabilities has the potential to rapidly isotropize the system and, as a result, reach equilibrium. This also implies that the turbulent flow is diffusive, meaning that both energy and momentum are dispersed throughout the fluid. Additionally, it is dissipative, which means that it eventually fades away with time. When there is an active energy source present in the momentum space, a driven stationary turbulence develops. However, we do not have a continuous energy source in heavy ion collisions. As a result, we obtain a freely propagating energy cascade, often known as free turbulence.

Scalar field theories [28–31] and Quantum Chromo Dynamics [32–34] are two fields that have involved the study of turbulent flow in recent times. Most of the time, it is considered that the turbulence produced in the relativistic heavy ion collision experiments is isotropic in nature [35]. Some theories suggest that turbulence develops here by an entropy cascade instead of an energy cascade [36]. They are likewise explored under the presumptions of homogeneity and isotropy. In contrast to the non-relativistic scenario, it has been demonstrated that a completely relativistic turbulence has richer dynamics. Investigations have been done for the tensor-driven turbulent flow in an isotropic, relativistic fluid. The suggested patterns, however, are challenging to reconstruct in the real environment. The system in heavy ion collision has anisotropy in its momentum space

and is also rotating. We are interested in studying the anisotropies produced in turbulence in this chapter. Since there is a large momentum anisotropy in different planes, we utilize the same planes to analyze the anisotropy in the turbulence spectra. Considering x as the axis of the impact parameter and z as the beam axis, we find various scaling exponents of turbulence spectra in both the transverse $(x-y)$ and longitudinal $(x-z)$ planes. For different planes, we obtain a different exponent. The exponent is closer to the Kolmogorov convective range in only one plane. For the non-relativistic context, the exact scaling relation of the Kolmogorov type typically holds. Even though many studies have suggested that the conventional interpretation of the energy cascade in the Kolmogorov case may be misleading, it has been demonstrated that precise scaling outcomes are possible for relativistic turbulence, which limits to the Kolmogorov relation for lower velocities [37]. A recent study confirmed the classical definition of a relativistic energy cascade [38]. This suggests that the energy cascade model can also be used to study relativistic turbulence.

Kolmogorov proposed the hypothesis that energy in turbulent flows, carried by eddies of diameter D, tend to gravitate toward $D^{5/3}$ [39]. However, this is true only in the inertial subrange, which is a particular set of length scales. Kolmogorov spectra have a power-law character in this sub-range where the kinetic energy can be expressed as,

$$E(k) \approx k^{\nu} \approx k^{-5/3} \tag{3.1}$$

The transfer of energy from low to high momenta exhibits a power-law behavior with the exponent $\nu = -5/3$, as indicated by the Color Glass Condensate (CGC) lattice simulation in ref. [40, 41]. The range of acceptability of the exponent ν is generally rather broad. In the case of classically scale invariant renormalizable interactions in QCD, ν has been determined to be $-5/3$ and $-4/3$ for energy and particle cascade, respectively [42].

The distribution of relativistic velocities of the particles produced after the collision is specified by the AMPT model. The output velocities provided by the simulation can be used to determine the velocity correlations. Here, we have employed velocity correlation to extract the initial energy spectrum from AMPT simulation. Since it is known that the initial geometry distribution is anisotropic, we have used the energy cascade to study anisotropic turbulence. Although the tensor degrees of freedom sometimes exhibit distinct characteristics for relativistic and non-relativistic velocities, we do not examine these higher degrees of freedom in this work.

The temperature fluctuations of a turbulent fluid can also be used to examine anisotropic turbulence. The temperature at a specific location in a laminar flow is constant during a steady state. The heat transfer and temperature at a point are both functions of time in a turbulent flow. Heat flow is comparable to the transfer of momentum in a turbulent flow where the velocity is time-dependent. So, in a turbulent flow, temperature fluctuations occur along with velocity fluctuations. In this scenario, there will be an extended momentum and heat transfer in the availability of these fluctuating components. Ref. [43] discusses the temperature spectrum of a turbulent fluid. The temperature fluctuation spectrum for isotropic turbulence is observed to be Gaussian. If anisotropies exist in the turbulent system, it is indicated by deviations from the Gaussian spectrum. However, the temperature fluctuation spectrum has not been addressed in any turbulence analysis in heavy ion collisions. This temperature spectrum can provide information about the system's thermal length scales. The diameter of the smallest eddies is correlated with the smallest length scale associated with this spectrum. We study this during the pre-equilibrium phase of HIC. This is because we derive the temperature from the energy density keeping the condition of local thermal equilibrium at various places in the system. Since we can describe the spectrum in three dimensions entirely in this case, we will take the entire spectrum into account for all temperature fluctuations. This is different from the velocity fluctuations. In order to determine whether there is any major departure from the Gaussian distribution in the case of the heavy ion collision, we attempt to obtain a similar Gaussian spectrum. The shortest length scale of the eddies in the turbulent flow is determined using the spectrum. We are interested to see how collision energy affects the temperature fluctuation spectrum.

3.2 The turbulence spectra and length scales

The geometry of heavy ion collision makes the velocity flow irregular. In the early stages, this causes turbulence in the velocity field. In turbulent flow, eddies of varying sizes may be seen. We must isolate the laminar component from the particle velocity to obtain the turbulent component of the velocity field. The turbulent component is obtained by dividing the actual velocity into the laminar flow and the fluctuating component as,

$$\vec{u}(\vec{x}) = \vec{U}(\vec{x}) + \vec{u}^{'}(\vec{x}) \tag{3.2}$$

Here, the laminar component is given by $\vec{U} = \langle \vec{u} \rangle$ and the turbulent component is $\vec{u}^{'} = \vec{u} - \langle \vec{u} \rangle$. The position vector at which the velocity is taken into consideration is given by the vector $\vec{x}$. Since we employ a discretized grid structure in our study to calculate the average velocity, the position vector in those cases refers to the position

vector of the cell whose average velocity we are determining. When we talk about the velocity correlations later in this section, we will go into more detail about this. Any primed quantity used in the paper will be used to indicate the turbulent component of the specific field. When studying turbulence, we statistically average the velocity to determine the laminar flow. In comparison to studying velocity using the Navier-Stokes equations, this provides a more deterministic solution. To determine average velocity, two different statistical averages can be used. For the first case, the space average is derived considering velocities at a specified time and averaging them over the entire volume V that the system occupies,

$$\langle \vec{u} \rangle = \lim_{\Delta x \to 0} \int_V \frac{\vec{u} d^3 x}{V} \tag{3.3}$$

And the other is the time average, which averages across time while maintaining a fixed point in space.

$$\langle \vec{u} \rangle = \lim_{\Delta T \to \infty} \int_0^T \frac{\vec{u} dt}{T} \tag{3.4}$$

In the current study, we want to examine if the turbulence spectrum of the collision reflects the anisotropy in the initial geometry of the relativistic heavy ion collisions. We do this by using the velocity correlation tensor for the turbulent velocity component, which is given by,

$$R_{ij}(\vec{r}) = \left\langle u_i'(\vec{x}) u_j'(\vec{x} + \vec{r}) \right\rangle \tag{3.5}$$

In this case, u_i' stands for the fluctuating component of velocity. The $\langle\rangle$ signifies the average over space. This demonstrates the connection between the fluctuating velocities at the two locations indicated by the variables $\vec{x}$ and $\vec{x}+\vec{r}$. The energy spectrum tensor $E_{ij}(\vec{K})$ and the R_{ij} are related by,

$$E_{ij}(\vec{K}) = \frac{1}{(2\pi)^3} \int\int\int e^{-i\vec{K}.\vec{r}} R_{ij}(\vec{r}) d\vec{r}. \tag{3.6}$$

If isotropic turbulence is assumed, the final expression of the Fourier transform to the wave vector $\vec{K}$ space is $E(k)$,

$$E(k) = \frac{1}{(2\pi)^3} \int\int\int e^{-i\vec{K}.\vec{r}} R_{ij}(r) dx dy dz. \tag{3.7}$$

where k is the magnitude of $\vec{K}$ and the volume element across which the integration is performed is $dxdydz$.

The conventional approach is to select a chosen axis and identify the constantly evolving velocity components parallel to this axis for a lower-dimensional energy spectrum.

This represents a profile of the entire spectrum. We call this the longitudinal spectra. The velocity correlation tensor for the velocity fluctuations orthogonal to this axis for the transverse spectra is obtained. It can be demonstrated that in isotropic turbulence, the longitudinal and transverse spectra possess the same coefficient in both planes. We define the beam axis, i.e., the z axis, as the preferred axis for relativistic heavy ion collisions. Therefore, in order to find the longitudinal spectrum, one must identify the velocity correlation in the $x - z$ plane, which is parallel to the z axis, and one must identify the velocity correlation perpendicular to the z axis for the transverse spectra.

The energy spectrum essentially depicts the distribution of kinetic energy among the various eddy sizes. We address the critical length scales involved in this particular system before moving on to analyze the turbulent spectra in depth because the length scales in the system specify the eddy sizes.

In a turbulent flow, the rotating structures can be of various sizes. As a result, our problem involves many length scales. The distance over which the characteristic gradients of several variables are present determines the length scale of a system. Thus, the largest eddy that forms in the system may have the largest length scale. These large eddies extract kinetic energy from the mean flow to generate angular momentum. The bulk of the energy in relativistic heavy ion collisions transforms into angular momentum before dissipating in the smaller eddies. This is referred to as the energy cascade. The Reynolds number can characterize this energy cascade. The ratio of inertial force to viscous force is referred to as the Reynolds number [44];

$$Re = \frac{F_i}{F_v} = \frac{\rho u l}{\mu_d} \tag{3.8}$$

Here, the inertial force and the viscous force are given as, $F_i = \rho l^3 \frac{u^2}{l}$ and $F_v = \mu_d \frac{u}{l} l^2$ respectively. The density and length scale are represented by ρ and l, while the fluid's dynamic viscosity is represented by μ_d. As a result, the onset of turbulence depends on the fluid's density, viscosity, size of the medium, and fluid velocity. Large Reynolds numbers result in greater eddies because the fluid viscosity is less dominant than the fluid inertia. This is the Kolmogorov spectral regime [45]. In this case, the vortex interaction explains the mediation of a spectral energy flow which is scale invariant. The energy is moved from the mean flow to the large eddies, where it is then transferred through the smaller eddies, as indicated in refs. [46–48]. As RHIC systems usually have high Reynolds numbers, we anticipate a Kolmogorov-type energy spectrum in this scenario. As mentioned, the system size determines the largest length-scale in the system. We used the cell size of 0.3 fm and 48 cells in each direction for the simulations. Thus, the size of our system is $l = 14.4$ fm in both directions. Additionally, the Au nuclei's

diameter is about 12 fm. As a result, this eddy size shall be the largest in the system , and this gives us the minimum wave number limit k_{min},

$$k_{min} = \frac{2\pi}{l} = 0.524\ fm^{-1} \tag{3.9}$$

Impact parameters are chosen in the $0 - 15$ fm range for minimum bias $Au - Au$ events. In such case, k_{min} approximately equals $0.42\ fm^{-1}$.

The Kolmogorov length scale is defined as the length scale of the smallest eddy [44]. This is obtained by making the Reynolds number very small in Eq.3.8.

$$\zeta = \left(\frac{\mu_k^3}{\epsilon_d}\right)^{1/4} \tag{3.10}$$

Here, μ_k represents the kinematic viscosity, while ϵ_d denotes the rate of energy dissipation. The relationship between the kinematic and dynamic viscosities is $\mu_k = \frac{\mu_d}{\rho}$. We will have the dimension of length scale if we insert the dimensions of μ_k and ϵ_d in Eq. 3.10 [44]. The Reynolds number is correlated to the smallest length scale by,

$$\zeta = lRe^{-3/4} \tag{3.11}$$

The kinematic viscosity for a QGP system estimated in reference [49] which is,

$$\mu_k \approx 10^{-7}\frac{m^2}{s} \approx 1.69\ GeV^{-1} \tag{3.12}$$

The energy density in the heavy-ion collision must be greater than the nucleonic density in order to produce a QGP state. If we use the energy density bound about 2 GeV/fm^3, the Kolmogorov length scale will be 1.24 fm (ref. Eq. 3.10). Since this is the lowest eddy scale, we may estimate the wave number corresponding to it using an equation analogous to Eq. 3.9. In this case, k_{max} is roughly 5. According to ref. [50], the Reynolds number for the system produced by RHIC energies is $Re \geqq 8.52$. In that case, k_{max} has a minimum value of 3, and $\zeta \approx 2.4\ fm$, which is derived using Eq. 3.11. Depending on the choice of planes, the minimum length scale may change. Smaller eddies can also form for lower Reynolds numbers. To account for every probable length scale of the $Au - Au$ collisions at RHIC energies, we include the entire energy spectrum from $k = 0.5$ to $k = 20$ in the simulations.

3.3 Results and Discussions

3.3.1 Longitudinal plane spectra

We start by talking about the scenario of the longitudinal plane. This plane contains the z-axis. This indicates that we are taking the longitudinal velocity correlation between two positions on the $x - z$ plane that are separated by $\vec{d}$.

$$R_{ij} =< u_i'(\vec{r}, t), u_j'(\vec{r} + \vec{d}, t) > \tag{3.13}$$

Here, the position of the grid cell with turbulent velocity u_i' is represented by $\vec{r}$, while the grid cell with velocity u_j' is represented by $\vec{r} + \vec{d}$. We take into account equal-time correlators and exclude the "t" from subsequent equations. This is similar to Eq. 3.5. The primary reason for explicitly writing out this equation is that when we compute the velocity correlation in the longitudinal plane, we must account for the Lorentz boost effect because the particles are colliding with relativistic velocities along the z axis. Therefore, the z axis is boosted as well as the $\vec{d}$. This indicates that in order to account for the Lorentz boost, the correlation function must be modified. We utilized the formula from a recently published research [51] to determine the energy spectrum in our context. This involves the transfer of $u(x)$ to the new reference frame $u(x+\Delta x)$ which is obtained using the boost $\Lambda(\Delta x)$,

$$\Lambda(\Delta x)u(x + \Delta x) = u(x) \tag{3.14}$$

In our scenario, we only require to boost the velocities along the boost direction to get the equal time correlator.

$$R_{ij} = \Lambda(d/2)\Lambda(-d/2) < u_i'(r - d/2), u_j'(r + d/2) > \tag{3.15}$$

Here, the correlator is boosted to the local reference frame at the midpoint between the two points. The vector $\vec{d}$ is now the line connecting the two positions specified in Eq. 3.13. We used the boost given in ref. [51] as

$$[\Lambda(d/2)u]_\mu = u_\mu - u_\mu(\Delta u.u) + \Delta u_\mu(u.u) \tag{3.16}$$

where $\Delta u = u(x + d/2) - u(x)$. Our outcomes will now be unaffected by the reference frames we choose. However, this is challenging to accomplish in the grid structure we are currently using. We put it into practice by presuming that it is an infinitesimal boost. This is also discussed in detail in ref.[51]. For an infinitesimal boost, we derive the $\Lambda(d/2)$ matrices, and then we calculate R_{ij} for each pair of velocities in the $x - z$

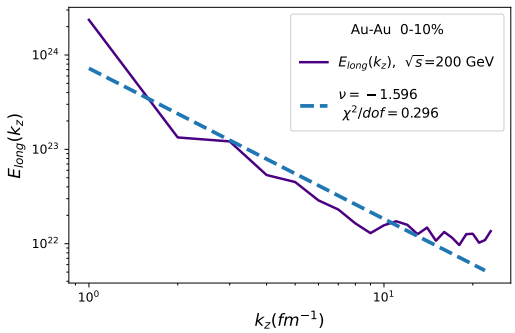

FIGURE 3.1: Turbulence velocity spectra on the longitudinal plane at $\sqrt{s_{NN}} = 200$ GeV. The range of centrality is $0 - 10\%$. ν= -1.596

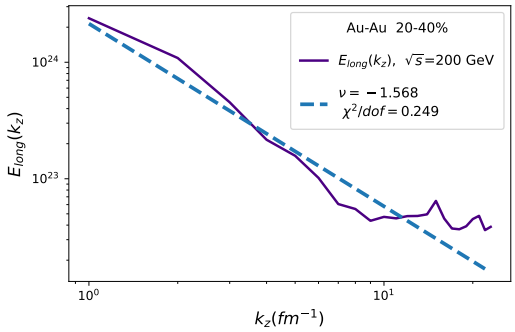

FIGURE 3.2: Turbulence velocity spectra on the longitudinal plane at $\sqrt{s_{NN}} = 200$ GeV. The range of centrality is $20 - 40\%$. ν= -1.568

plane. The two-dimensional scalar kinetic energy spectrum $E(k)$ is calculated after we have R_{ij}, which is specified in Equation 3.7. To perform the integration, we use the minimum and maximum length scales of two dimensions. The integration is performed for the location $r + \frac{d}{2}$ rather than the position r as we have applied the boost. For our computations, we consider the real component of the exponential.

As previously noted, there is typically a specified axis, and planes are picked parallel and perpendicular to the chosen axis for evaluating a profile of the entire three-dimensional spectrum. Thus, the three-dimensional energy spectrum $E(k)$ will be transformed to the parallel plane energy spectrum, which we represent by $E_{long}(k_z)$, and the perpendicular plane transverse energy spectrum, which we designate by $E_{tr}(k_{tr})$. After fitting the graphs for $E_{long}(k_z)$ for various values of k_z, the exponent ν of k_z is derived

The turbulence spectra of the velocity field for collision energy ($\sqrt{s_{NN}}$) of 200 GeV for $0 - 10\%$ centrality, $20 - 40\%$ centrality, and $40 - 80\%$ centrality are shown in Fig. 3.1, Fig. 3.2 and Fig. 3.3. These figures are plotted in log-log scale and are constructed in the longitudinal plane. The dashed line on it is the one that fits best in the range

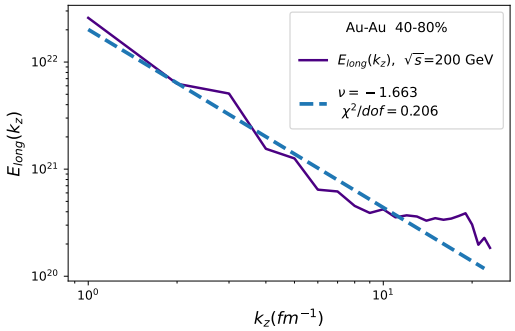

FIGURE 3.3: Turbulence velocity spectra on the longitudinal plane at $\sqrt{s_{NN}} = 200$ GeV. The range of centrality is $40 - 80\%$. ν= -1.663

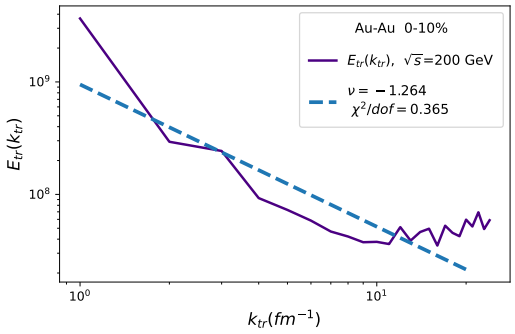

FIGURE 3.4: Turbulence velocity spectra on the transverse plane at $\sqrt{s_{NN}} = 200$ GeV. The range of centrality is $0 - 10\%$. ν=-1.264

of k_z considered for our simulation. We determine the exponent ν by computing the slope of the fitted straight line. On every occasion, the exponent is around -1.6 for the longitudinal plane spectra. This is roughly equivalent to $-5/3$, which is close to the Kolmogorov limit. As a result, the spectra in this plane portray the Kolmogorov spectrum. In this case, the inertial force exceeds the dissipative force.

3.3.2 Transverse plane spectra

We now provide the outcomes for the transverse plane spectrum. Our chosen axis, the z axis, is perpendicular to the transverse plane. The velocity components perpendicular to the z-axis remain unchanged because the system is only boosted along one axis. Therefore, in order to obtain the velocity correlation tensor on the transverse plane, we do not need to transform the velocities. For each pair of points, we determine the velocity correlation tensor and record the various values of R_{ij}. We obtain the spectrum $E_{tr}(k_{tr})$ using these R_{ij}.

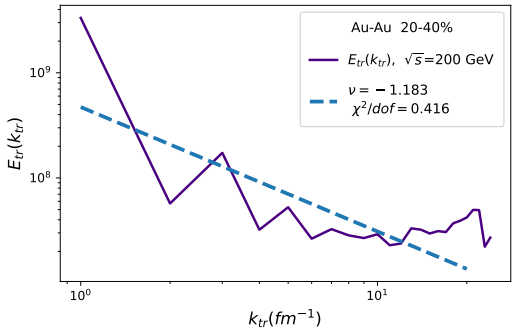

FIGURE 3.5: Turbulence velocity spectra on the transverse plane at $\sqrt{s_{NN}} = 200$ GeV. The range of centrality is $20 - 40\%$. ν=-1.183

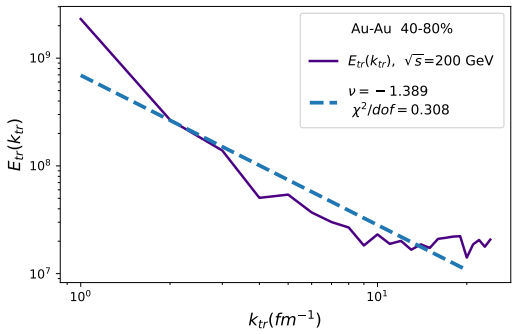

FIGURE 3.6: Turbulence velocity spectra on the transverse plane at $\sqrt{s_{NN}} = 200$ GeV. The range of centrality is $40 - 80\%$. ν= -1.389

The transverse plane turbulence spectrum of the velocity field for $0 - 10\%$ centrality and $20 - 40\%$ centrality at the collision energy of 200 GeV is depicted in Fig. 3.4 and Fig. 3.5. Once again, the fitted graphs are used to determine the power-law exponent ν. A power law exponent of -1.26 is found in Fig. 3.4, although a smaller exponent (-1.18) is observed in Fig. 3.5. The spectrum for the $40 - 80\%$ centrality region is shown in Fig. 3.6, and the exponent obtained is higher than that of $0 - 10\%$ centrality but lower than the exponent of the Kolmogorov spectrum. It is interesting to note that in none of these instances, the power law exponent remains constant. In the presence of significant dissipative forces, a power law exponent of $-4/3$ is attained. These numbers seem to be closer to $-4/3$ than the Kolmogorov limit. The exponent for collision energies of 19.6 GeV, 62.4 GeV, 100 GeV, and 130 GeV have also been determined. In all of the planes, the exponents have the same characteristics. It is always closer to $-5/3$ for the longitudinal plane and $-4/3$ for the transverse plane. This appears to suggest that, at this point, our outcomes are independent of the collision energy.

As a consequence, the coefficients for the longitudinal and transverse spectra are different. We realize that the initial distribution is not spherical. Even if the difference

may not be substantial, they will result in different Schmidt numbers. The Schmidt number is defined as the ratio of the kinematic viscosity to the interparticle diffusion rate [52]. In comparison to the longitudinal spectra, the transverse spectrum leads to a larger Schmidt number. The entropy density can be thought of as a measure of the inter-particle distance in heavy-ion collisions. It is widely known that the shear viscosity is a measure of the mean free path of a system. For heavy-ion collision, the shear viscosity to entropy density ratio $\frac{\eta}{s} < 1$. This implies that the QGP's spectrum should approximate a Kolmogorov spectrum. This occurs only in the longitudinal plane but not in the transverse plane.

The QGP appears "lumpy" in the transverse plane [53] due to the geometry of the collision. The overlap region in the $x - y$ plane exhibits a significant anisotropic pressure gradient and a very high energy density. Therefore, the particle distribution on this plane is not uniform. This indicates that on this plane, neither the mean free path nor the interparticle distance is uniform. This results in different coefficients in the turbulence spectra. The distinctive power law coefficient in the two planes indicates that turbulence is not isotropic in the fireball. The spatial anisotropy of the overlap zone in the two separate planes can be linked to this anisotropy. The discrepancy in the power law coefficient is caused by the different ratios of the viscous diffusion rate to the interparticle diffusion rate of the two planes.

We have also observed that for each plot in the transverse plane, the Schmidt number will have a distinct value depending on how these coefficients differ. Since the Schmidt number is higher, momentum diffusion is more prevalent in the transverse plane. It has already been documented in ref. [54] that the collision centrality affects the viscous effects that lower the elliptic flow's magnitude. The power law exponent varies at various centralities, which is represented in our spectrum.

3.4 Power spectrum of temperature fluctuations

The shear stress or Reynolds stress in a turbulent flow can be calculated using the equation of motion. The tangential stress is determined by the fluid viscosity and the change in velocity perpendicular to the flow direction.

$$\Pi = -\rho(\gamma + \epsilon_m)\frac{\partial \bar{v_x}}{\partial y} \tag{3.17}$$

where ρ is the density, ϵ_m is the turbulent viscosity coefficient, γ is the thermal diffusivity coefficient, and $\bar{v_x}$ is the average velocity along the x axis. This equation originates from the conservation of momentum. Similar to this, the conservation of energy can be used to determine the total heat flow.

$$Q = -\rho c_p(\alpha + \epsilon_p)\frac{\partial \bar{T}}{\partial y} \tag{3.18}$$

Here, c_p stands for the specific heat at constant pressure, ϵ_p for the coefficient of eddy diffusivity for heat, α for the thermal conductivity coefficient, and $\bar{T}$ for the average temperature. The temperature gradient in the direction perpendicular to the direction of flow causes the heat flow to develop. The nature of the above two equations is similar. The laminar component is in the first term in both equations, and the turbulent contribution, which is made up of two fluctuating components, is in the second term. The velocity part we have covered in the earlier sections, whereas this part involves the temperature. We will now continue our analysis of temperature fluctuations.

In many different conditions, temperature fluctuations in heavy-ion collisions have previously been described in ref. [3, 17, 55]. Once we are aware of the particle distribution, we segment the system into smaller cells. These cells each contain a sufficient number of particles to justify the assumption of local thermal equilibrium. The Gibbs-Boltzmann formula, which links energy density to temperature, can then be used to determine each of these cell's temperatures. We found that the temperature distribution that was thus obtained have high fluctuations.

One can define the power spectrum of temperature fluctuations for the condition of isotropic turbulence starting with the heat transfer equation [43],

$$\frac{\partial T}{\partial t} + v_k\frac{\partial T}{\partial x_k} = \gamma\frac{\partial^2 T}{\partial x_j \partial x_j} \tag{3.19}$$

Here, we have made the assumption that any two points, P and P', will have temperatures T and T'. The temperature correlation between the two specified points is therefore defined as $m(r) =< TT' >$. If we assume that the temperature variation is a random function of space, we can represent it as a stochastic Fourier integral.

$$T(x) = \int_\lambda e^{ix_p k_p} dh(k) \tag{3.20}$$

here h(k) is a random function of k_1, k_2, k_3. Here two points in wave-number space are represented by $\mathbf{k}$ and $\mathbf{k}'$. At the same point, the product of their increments is very

small but not zero. It is described as,

$$< dh^*(\mathbf{k})dh(\mathbf{k}) >= \Phi(\mathbf{k})d\mathbf{k} \tag{3.21}$$

The complex conjugate is denoted by the asterisk in this case. $\Phi(\mathbf{k})$ in this case only depends on k, as temperature is a scalar fluctuation. After that, the correlation function can be obtained by,

$$m(r) =< TT' >= 4\pi \int_0^\infty k^2\Phi(k)\frac{Sinkr}{kr}dr \tag{3.22}$$

Thus, we can obtain the power spectrum as

$$G(k) = 4\pi k^2\Phi(k) \tag{3.23}$$

The connection between the temperature correlation and the power spectrum is represented by,

$$G(k) = \frac{2}{\pi}\int_0^\infty m(r)krSinkrdr \tag{3.24}$$

As long as we are aware of the temperature at various points, we can derive the power spectrum of temperature fluctuations. However, unlike the energy fluctuation, it was not possible to extract the power spectrum of the temperature fluctuations in the two separate planes. Therefore, we begin by assuming that the temperature fluctuations are isotropic. But, we will see from the results that the fluctuation spectrum does not end up being Gaussian contrary to what is predicted for the isotropic case [43]. We deduce that the temperature fluctuations cannot be isotropic after observing that a Gaussian cannot fit the fluctuation. Hence, the temperature fluctuation is also anisotropic.

We obtain the energy of the system at various length scales in order to obtain the power spectrum. The temperature can then be obtained using,

$$\epsilon(x, y) = 12(4 + 3N_f)(\frac{T^4}{\pi^2}) \tag{3.25}$$

Here, the number of quark flavors is $N_f = 3$. The temperature is that of the pre-equilibrium stage since the energy is estimated from the partons after they have undergone scattering. At two distinct times, we plot the power spectrum of the temperature fluctuations at $\sqrt{s} = 200$ GeV.

The power spectrum of temperature fluctuations at $\tau = 1$ fm/c is shown in Fig. 3.7. This includes all parton scatterings up to $\tau = 1$ fm/c. We show that it can be roughly fitted to a Gaussian distribution. We can see that the fit is less adequate at higher k

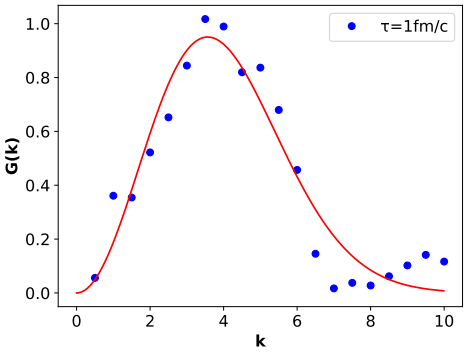

FIGURE 3.7: The power spectrum of the temperature fluctuations for 200 GeV Au-Au central collision events at $\tau = 1fm/c$. The units of k is in fm^{-1}. It is fitted with a Gaussian function.

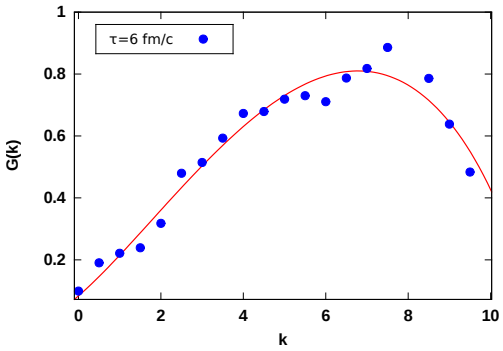

FIGURE 3.8: The power spectrum of the temperature fluctuations for 200 GeV Au-Au central collision events at $\tau = 6fm/c$. The units of k is in fm^{-1}. At later times the peak of the power spectrum shifts to higher values of k, it is fitted with an asymmetric Poissonian q -Gaussian distribution.

values, which suggests shorter length scales. We observe that as time progresses, the peak of the Gaussian shifts to smaller length scales and higher k values. The power spectrum of temperature fluctuations at $\tau = 6$ fm/c is shown in Fig. 3.8. Again, this indicates that in order to determine the spectrum of temperature fluctuation, we have taken into account all parton scatterings up to $\tau = 6$ fm/c. It is interesting to note that this nature is still there at all of the collision energies we have examined. As time progresses, it appears that energy is shifted to smaller eddies, as indicated by the shift of the peak to shorter length scales. It is also possible to estimate the scale of the temperature fluctuations using the following equation,

$$\lambda_{sc} = \frac{1}{< T^2 >_{avg}} \int_0^\infty m(r) dr \tag{3.26}$$

At $\tau = 6$ fm/c, the scale of the temperature fluctuation is calculated to be 1.16 fm. The length scale determined for the smallest eddies in the previous section is comparable to

this one.

Although a Gaussian distribution can roughly fit the power spectrum even at later times, the q-Gaussian distribution provides a better fit. The q-Gaussian distribution is a generalization of the standard normal probability density. We employ the asymmetric Poissonian q-Gaussian distribution [58] to fit the spectra because it becomes asymmetric later in time. Fig. 3.8 displays the fit to the distribution using an asymmetric q-Gaussian distribution. The distribution is given by,

$$P(k) = \frac{c}{N_{\beta\beta'}}(1-k^2)^{((\beta+\beta')/2)-1}\left(\frac{1+k}{1-k}\right)^{(\beta-\beta')/2} \tag{3.27}$$

Here we have,

$$q = 1 - \left(\frac{(\beta+\beta')}{2} - 1\right)^{-1} \tag{3.28}$$

and the asymmetry parameter is given by,

$$a = \frac{(\beta-\beta')}{2} \tag{3.29}$$

Here $N_{\beta\beta'}$ is a constant given by,

$$N_{\beta\beta'} = 2^{\beta+\beta'-1}\Gamma(\beta)\Gamma(\beta')/\Gamma(\beta+\beta'). \tag{3.30}$$

In our case, we use c, β, and β' in the distribution as open parameters to fit with our temperature spectrum.

Though it appears that the temperature fluctuations can be somewhat fitted by a Gaussian, the anisotropy seems to grow over time. Although it was impossible to examine individual planes for temperature fluctuations, the spectra of temperature fluctuation shows an overall anisotropy in the temperature spectra as well.

3.5 Summary

To summarise, we have studied the partonic system in the initial and pre-equilibrium phases of the heavy-ion collision. The energy spectrum for the turbulent flow velocities has been computed. For the specific system, the wave number range and hence the eddy sizes are first determined. Then, under various initial conditions, we were able to find the turbulence spectra both on the heavy-ion collision's longitudinal plane and transverse plane. The spectra coefficients, ν, for the two separate planes have been determined. We

showed that the ν value for longitudinal spectra is $-5/3$, which is larger than the value for transverse plane spectra. The ν value for the transverse plane spectrum is around $-4/3$. As a result, the longitudinal plane's ν value is nearer to the Kolmogorov spectra. The energy dissipation is greater for the transverse spectra. We also observed that the power law coefficient is only affected by the collision's centrality for the transverse plane. The anisotropic pressure gradients produced in this plane result in spatial anisotropy in particle distribution. This may cause asymmetric energy dissipation. Further, the collective flow in the transverse plane is suppressed by the viscous nature of the fluid. We observe in chapter II how shear viscosity has an effect on the elliptic flow. Therefore, the viscosity has a centrality dependence that is represented in the spectrum's Schmidt number. This also affects the energy dissipation in the transverse plane for different centralities, which can be seen in our plots.

In the heavy-ion collision, the energy spectrum analysis showed that energy is transferred from the flow to the large eddies, which is then dissipated through the smaller eddies. This is also evident from our temperature spectra, where we have seen the peak shift to the smaller length scales at later times. Even though the turbulent system might be overall isotropic, if we divide it into different planes, the power law coefficients will differ on each plane. We illustrate this difference between the transverse and longitudinal planes in our plots. The turbulence in relativistic heavy-ion systems is assumed to be isotropic, but if the geometry of the collision is taken into consideration, the turbulence under study is invariably anisotropic. In our analysis, this is firmly shown.

Further, we analyze the temperature spectrum of the turbulent quark-gluon plasma in the early stages of equilibrium. Although temperature correlations and velocity correlations may be related to one another, they need not always be the same in a given system. This is why it is significant to study the temperature spectrum. The thermal length scales in the underlying condition are explored via the temperature spectrum. We believe that an understanding of these thermal length-scales is crucial in a high-temperature plasma. Though the thermal spectrum first looks to be Gaussian, we have observed that a q-Gaussian distribution fits it better over time. This shows that although the turbulence seen in relativistic collisions is generally isotropic and homogeneous, it would be more useful to slice it into planes and examine each plane independently. This will enable us to comprehend the anisotropies produced in the turbulent plasma on various planes and different length scales.

Bibliography

[1] K. Paech and A. Dumitru, Phys. Lett. B **623**, 200-207 (2005).

[2] T. Abe, K. Niu, J. Phys. Soc. Jpn. **49**, 717 (1980)

[3] P. Romatschke, M. Strickland, Phys. Rev. D **68**, 036004 (2003).

[4] S. Mrowczynski, Phys. Lett. B **214**, 587 (1988).

[5] M. Asakawa, S.A. Bass, B. Müller, Phys. Rev. Lett. **96**, 252301 (2006)

[6] M. Asakawa, S.A. Bass, B. Müller, Prog. Theor. Phys. **116**, 725 (2007)

[7] S. Floerchinger and U. A. Wiedemann, JHEP **11**, 100 (2011).

[8] F. Becattini et al., Eur. Phys. J. C **75**, 406 (2015).

[9] B. Schenke, S. Jeon, C. Gale, Phys. Rev. Lett. **106**, 042301 (2011).

[10] P. Bozek, Phys. Rev. C **85**, 034901 (2012).

[11] U. Heinz, R. Snellings, Ann. Rev. Nucl. Part. Sci. **63**, 123 (2013).

[12] C. Gale, S. Jeon, B. Schenke, Int. J. Mod. Phys. A **28**, 1340011 (2013).

[13] H. Song, U.W. Heinz, Phys. Rev. C **81**, 024905 (2010).

[14] M. Luzum, Phys. Rev. C **83**, 044911 (2011).

[15] P. Huovinen, P. F. Kolb, U. W. Heinz, P. V. Ruuskanen and S. A. Voloshin, Phys. Lett. B **503**, 58 (2001).

[16] P. F. Kolb, U. W. Heinz, P. Huovinen, K. J. Eskola and K. Tuominen, Nucl. Phys. A **696**, 197 (2001).

[17] T. Hirano and K. Tsuda, Phys. Rev. C **66**, 054905, (2002).

[18] P. F. Kolb and R. Rapp, Phys. Rev. C **67**, 044903 (2003).

[19] P. Romatschke and U. Romatschke, Phys. Rev. Lett. **99**, 172301 (2007).

[20] H. Song and U. W. Heinz, Phys. Letts. B. **658**, Issue 5, 279-283 (2008).

[21] Z. W. Lin, S. Pal, C. M. Ko, B. A. Li, and B. Zhang, Phys. Rev.C **64**, 011902(R) (2001).

[22] B. Zhang, C. M. Ko, and M. Gyulassy, Phys. Lett. B **455**, 45 (1999).

[23] Wei Li, Nucl. Phys. A **967**, 59-66 (2017).

[24] Y. Jiang, Zi-Wei Lin, and J. Liao, Phys. Rev.C **94**, 044910 (2016).

[25] A. Saha, S. Sanyal, Int. J. Mod. Phys. E **29**, No 01.2050001 (2020).

[26] X. Deng, X. Huang , Y. Ma , S. Zhang, Phys. Rev.C **101**, 064908 (2020).

[27] L.P. Csernai, V.K. Magas, D.J. Wang, Phys. Rev. C **87**, 034906 (2013).

[28] R. Micha and I. Tkachev, Phys. Rev. D **70**, 043538 (2003).

[29] J. Berges, A. Rothkopf and J. Schmidt, Phys. Rev. Lett. **101**, 041603 (2008).

[30] J. Berges, G. Hoffmeister, Nucl. Phys. B **813**, 383 (2009).

[31] J. Berges and D. Sexty, Phys. Rev. D **83**, 085004 (2011).

[32] A. H. Mueller, A. I. Shoshi and S. M. H. Wong, Nucl. Phys. B **760**, 145 (2007)

[33] P. Arnold and G. D. Moore, Phys. Rev. D 73, 025006 (2006); Phys. Rev. D **73**, 025013 (2006).

[34] J. Berges, S. Scheffler and D. Sexty, Phys. Lett. B **681**, 362 (2009).

[35] M. J. Tannenbaum, Rept. Prog. Phys. **69**, 2005 (2006).

[36] E. Calzetta, Physical Review D **103**, 056018 (2021).

[37] I, Fouxon and Y. Oz, Phys. Lett. B **694**, Issue 3, 261 (2010).

[38] G. L. Eyink and T. D. Drivas, Physical Review X **8**, 011023 (2018).

[39] A. N. Kolmogorov, C. R. Acad. Sci. URSS **30**, 301–305 (1941); C. H. Gibson, Proc. Roy. Soc. Lond. A **434**, 149-164 (1991).

[40] K. Fukushima, Phys. Rev. C **89**, 024907 (2014).

[41] K. Fukushima, F. Gelis, Nucl. Phys. A **874**, 108 (2012).

[42] M. E. Carrington, A. Rebhan, Eur. Phys. J. C **71**, 1787 (2011).

[43] S. Corrsin, J. Applied. Phys. **22**, 469 (1951); Y. Ogura, Journal of Meteorology, 539 (1958).

[44] Fluid Mechanics, Pijush K. Kundu, Ira M. Cohen and David R. Dowling, Elsevier Inc, 2012 ISBN 978-0-12-382100-3; Trinh Khanh Tuoc, arXiv:0910.2072 (2009).

[45] A. K. Kolmogorov, Dokl. Akad. Nauk SSSR 31, 538 (1941).

[46] V. Zakharov, V. L'vov, and G. Falkovich, Kolmogorov Spectra of Turbulence, Wave Turbulence Springer-Verlag, Berlin, (1992) ISSN 0940-2535.

[47] V. L'vov, Wave Turbulence under Parametric Exitation Springer-Verlag, Berlin, (1994), ISSN 0940-2535.

[48] U. Frisch, Turbulence Cambridge University Press, Cambridge, England, (1995), ISBN: 9781139170666.

[49] Matteo Baggioli, Vadim Brazhkin, Kostya Trachenko, SciPost Phys. **10**, 118 (2021).

[50] Brett McInnes, Nuclear Physics B **921**, 39-58 (2017).

[51] Xin An, Gökçe Başar, Mikhail Stephanov, and Ho-Ung Yee, Phys. Rev. C **100**, 024910 (2019).

[52] P. K. Kundu, I. M. Cohen, and D. R. Dowling, Fluid Mechanics, 5th ed.; Elsevier Academic Press: San Diego, CA, USA, (2012).

[53] W. Busza, K. Rajagopal and W. van der Schee, Ann. Rev. Nucl. Part. Sci. **68**, 1-49 (2018).

[54] U. Heinz, Annual Rev. of Nuclear and Particle Science. vol **63**, 123-151, (2013).

[55] A. Saha and S. Sanyal, Modern Physics Letters A **36**, No. 22, 2150152 (2021).

[56] Ágnes Mócsy and Paul Sorensen, Nucl. Phys. A **855(1)** 241-244 (2011).

[57] Sumit Basu et al. Phys. Rev. C **94**, 044901 (2016).

[58] Adrián A. Budini, Phys. Rev. E **91**, 052113 (2015).

Chapter 4

Temperature fluctuations and Tsallis statistics in Relativistic Heavy Ion collisions

4.1 Introduction

The understanding of temperature fluctuations in a system is crucial as it provides knowledge of the thermodynamic characteristics of the underlying system. The study of fluctuations can also lead us to the phase transition dynamics. In this chapter, we analyze temperature fluctuations that occur during the initial phases of relativistic heavy ion collision experiments (RHICE). We talk about the non-equilibrium limits of the system by analyzing temperature fluctuations. We focus on the plasma right after a collision, before it has a chance to equilibrate. We employ the non-extensive Tsallis statistics to determine the entropic index in the partonic stages of the RHICE . Previously, the hadronic phase is taken into consideration when calculating the entropic index using experimental data fitting of the transverse momenta (p_T). In this chapter, we will illustrate how the behavior of the entropic index during the initial non-equilibrium stage is remarkably similar to that of the entropic index during the hadronic stage.

In HIC, the conditions are such that the fluid immediately following a collision forms a non-equilibrium system [1]. Fluctuations in the initial distribution result in specific features in the final hadronic spectra. The majority of these are number density fluctuations [2]. Although hotspots and coldspots are known to form in spinning fluids [3], it is challenging to measure something like temperature fluctuations in actual experiments.

Due to this, the majority of attempts made to analyze the system's fluid dynamics have been focused solely on density variations.

There are attempts to perceive the thermodynamic characteristics of strongly interacting systems using a variety of methods in RHIC and CERN [4, 5]. Recently, some studies have reported temperature hotspots, and fluctuations in these systems [6]. The temporal evolution of these temperature fluctuations has been explored in smaller subsystems resembling canonical ensembles of varying temperatures [7]. The integrated observables and some of the differential observables have not been proven to be affected by the size of the hotspots. However, there are certain differential observables that might be responsive to these variations, such as sub-leading principal components [8]. In this study, we use a different approach when examining temperature fluctuations. We analyze the temperature instabilities during the early stages of the heavy ion collisions using a multiphase transport (AMPT) model. Despite being studied in the context of transport models, temperature fluctuations have primarily been discussed in the Gibbs-Boltzmann statistics. In this analysis, the temperature fluctuations in the partonic stages of HIC are investigated using the non-equilibrium Tsallis statistics. The extended thermodynamics of Tsallis has been applied previously to non-equilibrium systems [9]. The Tsallis statistics is a generalized form of the Boltzmann-Gibbs thermodynamics to non-equilibrium systems [10]. The entropic index, q, is used to define the thermodynamic quantities in this statistics. The Tsallis statistics reduce to the Boltzmann-Gibbs statistics for $q = 1$. The entropic index value serves as a measure of how much the system deviates from the equilibrium statistics. The fluctuation in the temperature distribution can be used to calculate the entropic index value. In recent years, the relativistic heavy ion collision experiments have been one of many non-equilibrium systems that have been modeled using the Tsallis entropy [11]. In all these cases, the entropic index was determined by fitting the transverse momentum data [12, 13].

The system requires a finite amount of time to reach equilibrium in the HIC system [14]. In order to examine the system before it achieves an equilibrium state, we have applied the non-equilibrium Tsallis statistics. We do this to comprehend the thermodynamics of the earliest phases of the collisions. We have used the standard definition of temperature and applied the Tsallis statistics instead of the BG statistics. The temperature calculations are thus only relevant within the bounds of local thermal equilibrium. We employ the AMPT model to determine the particle positions and velocities at $\tau = 1$ fm/c. The local thermal equilibrium is typically reached after 1 fm/c. We observe that the temperature fluctuations measured throughout the evolution are significantly large. We implement Tsallis statistics to get the entropic index from the temperature fluctuations.

For the partonic stage, we determine the value of the entropic index for various rapidities, centralities, and collision energies. The entropic index values obtained are higher than the values obtained by fitting the transverse momentum data. This is because the experimental analysis uses the Tsallis statistics in the hadronic phase [12]. They are typically in the order of $q \sim 1.12$ while the values of the entropic index we get generally are more than 1.2. We observe that the overall nature of the change in the entropic index with various system parameters is consistent with the entropic index obtained by fitting the Tsallis distribution to the transverse momentum data in the hadronic phase [12]. Therefore, we draw the inference that the entropic index behaves similarly in the partonic and hadronic phases as a function of the system parameters.

In section II, we look at the temperature hotspots observed using AMPT simulations during the early stages of HIC. The application of Tsallis entropy to temperature profiles derived from energy density and the computation of the entropic index based on our simulations are covered in Section III. We quickly describe the Tsallis entropic index calculation using experimental data and demonstrate that it is rather similar to the entropic index we found in section IV. In section V, we present a summary and conclusion of the findings of this chapter.

4.2 Temperature hotspots in the initial stages

The positions and velocities of the particles at the early stages of the collision are obtained using the AMPT model. We build a grid-based simulation in the x-y plane with cell sizes that allow us to fit a considerable number of particles into each cell. This will help us establish the local equilibrium condition as we are interested in analyzing the temperature fluctuations in the system. From the momentum and energy of every particle in the cell, we compute the average energy in each cell. It is believed that the system is not in equilibrium as a whole. We have effectively broken down our entire system into smaller subsystems, and we will assume local thermodynamic equilibrium in these smaller subsystems. Given that this is a statistical model, we create many events using the same parameters and initial conditions, and we then take the average of all the events to get the end results. So, the energy density distribution can be obtained from the particle distribution as follows [15],

$$\epsilon(x,y) = \sum N_i exp[-\frac{(x-x_i)^2 + (y-y_i)^2}{2\sigma^2}] \tag{4.1}$$

We choose a Gaussian having a width of $\sigma = 0.5$ fm. Additionally, we have $N_i = \frac{N}{2\pi}(\frac{1}{\sigma^2\tau})E_i$, where N is the normalization factor. The position coordinates are (x_i, y_i, z_i) ,

and $E_i = \sqrt{\boldsymbol{p}_i^2 + m_i^2}$ is the energy value of the i-th parton. The sum in equation 4.1 includes all of the particles involved in an event. We have used the rapidity window $-3 < \eta < 3$, where $\eta = \frac{1}{2} ln \frac{t+z}{t-z}$ is the space-time rapidity and $\tau = \sqrt{t^2 - z^2}$. The energy density is obtained using all four components of the energy-momentum tensor.

As previously noted, the entire system has been split into smaller subsystems with grid sizes of $dx = dy = 0.3$ fm. We also varied the size of the grid cells and tested the simulation with values of cell sizes ranging from 0.1 fm to 0.5 fm. Our results are independent of the grid cell size as long as it falls within this range. In order to determine the temperature in each of these grid cells, we have assumed local thermal equilibrium and employed the ideal gas Gibbs- Boltzmann statistics.

$$\epsilon(x, y) = 12(4 + 3N_f)(\frac{T^4}{\pi^2}) \tag{4.2}$$

Here N_f is the number of quark flavors; we have taken $N_f = 3$.

We based our temperature calculation on equilibrium statistical mechanics since there is still a lack of understanding of the temperature in non-equilibrium systems. This is because the second and zeroth laws of thermodynamics are difficult to extrapolate to non-equilibrium systems. In equilibrium thermodynamics, a system at equilibrium can be broken down into smaller ones, and each subsystem will measure the same temperature as the main system. However, all of the subsystems might not measure the same temperature in an out-of-equilibrium scenario. In an out-of-equilibrium state, it is therefore challenging to specify a single temperature [16]. The Tsallis statistics that we will use later to interpret the departure from equilibrium for this system solely depend on two parameters, the temperature, and the entropic index. If the system's entropic index is known, the temperature parameter can be associated with the Gibbs-Boltzmann temperature. The temperature parameter in the Tsallis distribution cannot be computed because the entropic index of the HIC is unknown a priori. Since the Tsallis statistics approximate the Gibbs-Boltzmann statistics when the entropic index is equal to one, the Tsallis parametric temperature will be roughly equal to the equilibrium Gibbs-Boltzmann temperature for entropic index values close to one. We may therefore draw the conclusion that the temperature considered in the Tsallis entropy calculation will be roughly equal to the system's equilibrium temperature. We determine the equilibrium temperature in each of the previously specified small grid cells. These temperatures will vary and represent the system's temperature fluctuations because the system as a whole is a non-equilibrium system. We obtained the temperature fluctuation in the $x - y$ plane. Both event-by-event plots and event-averaged plots have been observed. We begin by analyzing the event-by-event plots, which display the initial variations at

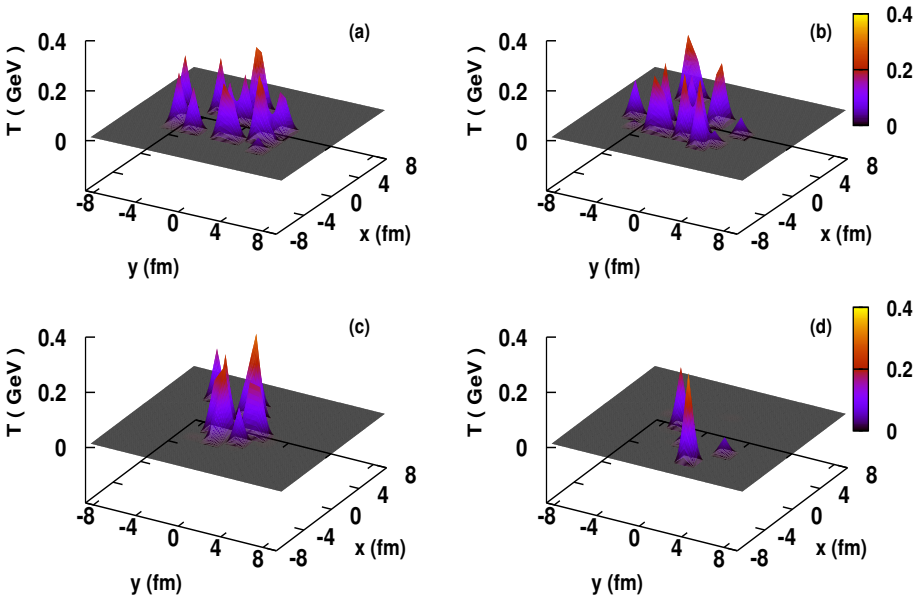

FIGURE 4.1: Temperature fluctuations at times a) 1 fm/c b) 2 fm/c c) 3 fm/c d) 5 fm/c at $\sqrt{s_{NN}} = 200$ GeV and $-1 < \eta < 1$ for Au + Au collisions

various collision energy and times.

The temperature distribution is shown in Figure 4.1 at various times. We observe that the temperature fluctuations are larger initially but become less over time. The temperature fluctuations for various collision energies are shown in Figure 4.2. As can be seen, regardless of $\sqrt{s_{NN}}$, the general pattern of the fluctuations do not change. At increasing $\sqrt{s_{NN}}$, the amplitude is the only thing that grows. Such temperature instabilities have been documented in earlier research [3, 17]. In the first study, temperature fluctuations are addressed in a manner similar to how CMBR (Cosmic Microwave Background Radiation) temperature variations are investigated for the early universe. The second study focused on determining the system's specific heat from temperature fluctuations. While the temperature hotspots appear to be comparable at different times, we treat the fluid as a non-equilibrium system and would like to analyze them further to understand the differences at various collision energies.

4.3 Tsallis entropy and the entropic index

As was previously stated, the Tsallis statistics is distinguished by the non-extensivity parameter q, with $|q-1|$ being a direct measure of the temperature fluctuations [18].

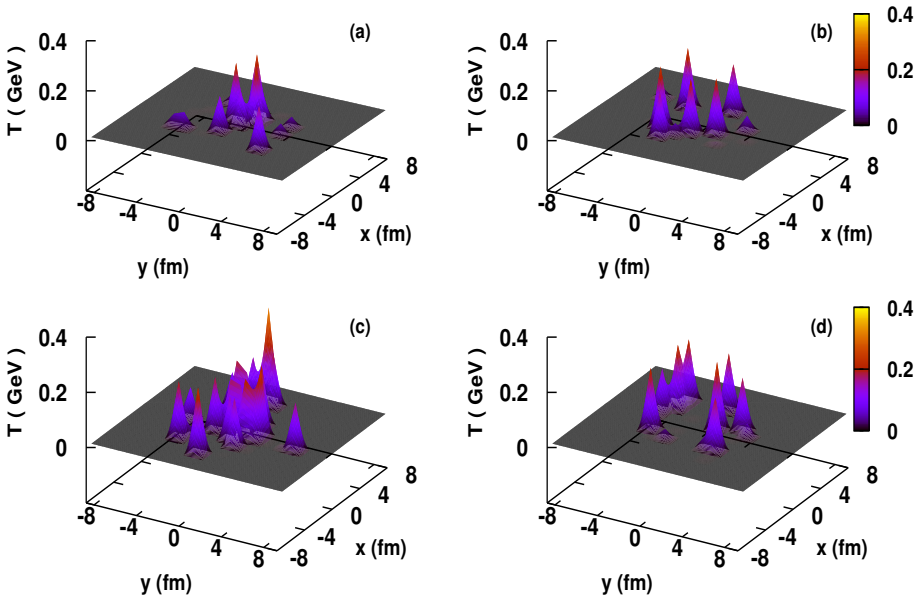

FIGURE 4.2: Temperature fluctuations at different $\sqrt{s}$ values a) $\sqrt{s_{NN}} = 19.6$ GeV b) $\sqrt{s_{NN}} = 62.4$ GeV c) $\sqrt{s_{NN}} = 100$ GeV d) $\sqrt{s_{NN}} = 200$ GeV at time $\tau = 1$ fm/c and $-1 < \eta < 1$ for Au + Au collisions

Although it was initially utilized to fit the hadron p_T spectra at various collision energies [19, 20], afterwards, it was employed in other scenarios of the relativistic heavy ion collisions [21]. As described in reference [21], in addition to hadrons, quark matter has also been studied using Tsallis statistics [22]. Both the hadronic and the quark-gluon plasma scenarios have been theoretically explored in ref. [23]. The thermodynamics of the system has also been studied in each of these cases. The partition function of an ideal gas is typically used to obtain these thermodynamic parameters. The analysis of the phase diagram reveals that the critical temperature obtained using Tsallis statistics is generally lower than that obtained using the equivalent Boltzmann-Gibbs statistics [21]. This is possible because the temperature determined by the equilibrium definition will always be higher than the temperature determined by any other approach [16].

The Tsallis statistics have also been used to extend the MIT bag model in ref.[22]. In this case, the Equation of State (EoS) has been established for various bag parameters and entropic index values. Despite the fact that the shape of the phase diagram is similar for both approaches, the critical temperature is found to fall with increasing values of the entropic index in this case. In ref.[24], the Tsallis entropy formula was also developed in a thermodynamic system comprised of a reservoir and a subsystem. The temperature is obtained, and the relation between the heat capacity and entropic index is also established. We recognize these specific references because we are interested in the connection

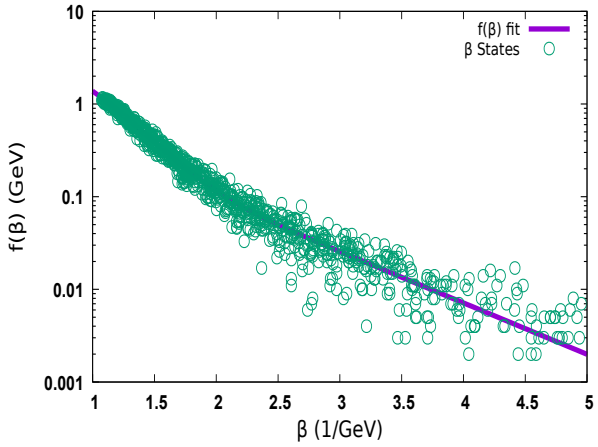

FIGURE 4.3: The plot of $f(\beta)$ for the temperature fluctuations at a collision energy of $\sqrt{s} = 200$ GeV (Au - Au collision, $|\eta| < 3$). The green circles are the fluctuating states. The value of q is obtained by fitting a χ^2 distribution to the plot. Purple line shows the fitted curve. The final values of the two parameters q and β_0 are $q = 1.51158$ and $\beta_0 = 0.968718 GeV^{-1}$, with the asymptomatic standard error for q being 3.5% and for β_0 being 0.33%.

between temperature and entropic index during the early phases of a heavy ion collision.

The relationship between the Tsallis entropy and the entropic index q in a system with varying temperatures has already been studied in the literature [25]. The quantity employed in this context is β, which is the inverse of temperature. The generalized distribution function of non-extensive Tsallis statistics is a result of integrating over all conceivable fluctuating β's provided that the β is χ^2 distributed [25, 26]. This is only true if a non-equilibrium system is formally characterized by a fluctuating β.

Given that our system also experiences temperature fluctuations, we used a χ^2 distribution to fit the probability distribution of β (i.e., the temperature inverse). It is demonstrated in ref. [25] that for any system with fluctuating temperatures, the following distribution can be used to determine the relationship between the entropic index and temperature:

$$f(\beta) = \frac{1}{\Gamma(\frac{1}{q-1})} \left(\frac{1}{(q-1)\beta_0}\right)^{(\frac{1}{q-1})} \beta^{\frac{1}{q-1}-1} exp\left(\frac{-\beta}{(q-1)\beta_0}\right) \tag{4.3}$$

Here the entropic index q is dimensionless, whereas the function has the temperature dimension (β^{-1}).

In Fig. 4.3, we plot the β distribution we obtained from our simulations after fitting it with the χ^2 distribution. We get a good fit for our temperature fluctuations, and these fits can be used to calculate the entropic index. The average of the fluctuating

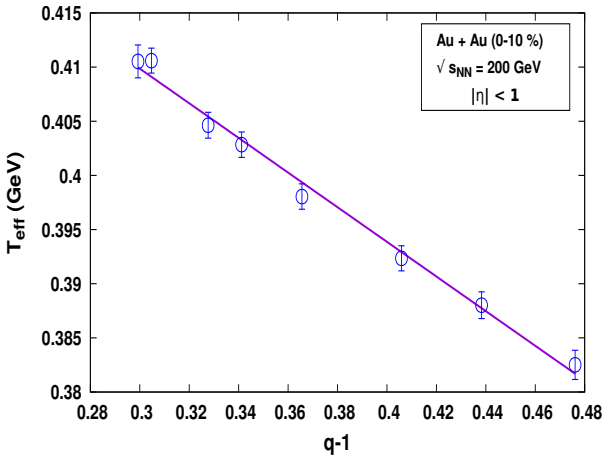

FIGURE 4.4: The plot shows the dependence of the effective temperature T_{eff} in GeV on the values of q (dimensionless) at a collision energy of $\sqrt{s_{NN}} = 200$ GeV for the Au+Au system, $(0 - 10\%)$ centrality with $|\eta| < 1$.

β is the constant β_0. The values of q and β_0 are found to be $q = 1.51158$ and $\beta_0 = 0.968718 GeV^{-1}$, respectively, with an asymptomatic standard error of 3.5% for q and 0.33% for β_0.

The entropic index has been observed to have some dependence on system parameters in the majority of physical systems. For instance, it has been found that the value of q is affected by the spatial scale. In the next section, we study how the entropic index or q value changes with various parameters of the system.

4.4 Results and Discussions

Our first observation is the correlation between temperature and entropic index. We observe that the temperature and entropic index have a linear relationship that fits nicely with a straight line shown in Fig. 4.4. In recent times, there have been efforts to extract the $(q - 1)$ values from experimental data [12]. The T_{eff} is defined differently in that method. For negative pions and antiprotons, the dependency of the effective temperature T_{eff} on the parameter q has been examined for different processes [18]. In that case, the slope of the fitted straight lines depends on the selected particles and reactions. This is seen in reference [27], where the authors analyze data from the $p + p$, $Au + Au$, and $D + Au$ collisions. They obtained entropic index values for positive pions in the range of 1.12, whereas we obtained entropic index values larger than 1.28. We are working with the early stages of the heavy ion collisions, which is the fundamental distinction between our study and the earlier research. We show that a linear dependence on the q values can be established even in our scenario. A straight line can be used to fit the

simulation's data. However, the slope we find is lower than the hadronic particle slope. The experimental results have already shown that the T_{eff} vs. q dependency may not be constant across all systems [28]. In ref. [28], it is demonstrated that the $p-p$ collision at high collision energies has a different slope, whereas the slope we found for $Au+Au$ collisions is similar to ref. [18]. They have found a different slope for the $Pb-Pb$ collision. Even though we obtain a linear dependency between T_{eff} and $(q-1)$, the slope of the straight line relies on the individual system being examined as well as the collision energy.

The calculation also relies heavily on the definition of temperature. According to ref.[18], the effective temperature is the temperature that results from both temperature fluctuations and the transfer of energy between the source and its surroundings. As a result, the system's effective temperature is different from its thermodynamic temperature. Our system has been split into smaller subsystems, and we have presumed that local thermal equilibrium exists in each of these smaller areas. Due to its out-of-equilibrium state, the system as a whole does not have a constant temperature throughout. This is also due to the non-uniform energy density distribution in the collision region. The values of the entropic index are larger in our case as compared to the values of the entropic index obtained from prior studies. This could be because the system at this stage is more out of equilibrium than the system in the hadronic phase [27]. As mentioned earlier, the Tsallis thermodynamics is incorporated in the MIT bag model in ref.[21], and the connection between temperature and energy density in that case is,

$$\epsilon = [\frac{7}{4}g_Q + g_G]\frac{\pi^2}{30}T^4 + \frac{8\pi^2}{30}g_Q g_G \frac{\pi^2}{90}(q-1)VT^7. \tag{4.4}$$

The quark and gluon degrees of freedom are represented here by g_Q and g_G. Consequently, there is a term that is proportionate to T^7 and has the entropic index in addition to the T^4 term. The temperature determined by this equation would differ from the temperature determined by the equilibrium relation $\epsilon = [\frac{7}{4}g_Q + g_G]\frac{\pi^2}{30}T^4$. As a result, the entropic index corresponding to various temperatures will differ. Therefore, the definition of the temperature used in the calculation of the entropic index will determine the precise value of the entropic index. The entropic index can also be determined directly from temperature variations,

$$q = 1 + \frac{Var(T)}{< T >^2} \tag{4.5}$$

Here, $Var(T)$ stands for the temperature variance. It can be seen here that the entropic index is dimensionless. This definition has been used by Wilk et al. in ref. [18], and they have achieved a similar result to that shown in figure 4.4.

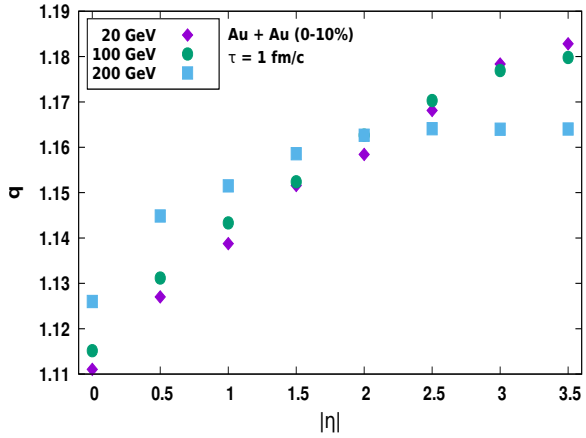

FIGURE 4.5: The plot shows the variation of q for different space time rapidity (η) values at different collision energies ($\sqrt{s}$)for Au + Au collision in the (0-10%) centrality range at $\tau = 1$ fm/c.

The change in the q value for various system parameters was then closely examined. Fig. 4.5 illustrates how q varies with space-time rapidity (η) and collision energy. Here we observe that our q value increases with increasing values of η, plateauing for higher collision energy. The scale of the system grows as the space-time rapidity increases. A bigger system size will result in a more significant divergence from equilibrium, which will enhance the entropic index value. We know from previous studies how significantly the entropic index depends on the type of system that is colliding. The Tsallis distribution appears to be challenging to use because the outcomes rely on the created particles and the colliding particles. In recent research, [29], a thorough analysis was conducted for a wide range of collision energies, a wide variety of particles, and a wide range of systems. In addition, the q values appear to be proportional to $\sqrt{s}/m$, and the q value also depends on the particle multiplicity.

Our values are different from those found in the hadronic spectrum for two main reasons. The first was also addressed earlier. It is the temperature definition that we have employed. The temperature values and also entropic index values would be affected if a different Equation of State (EoS) was applied. We are assessing the partonic system, which is an additional factor. It is also feasible that the system is more likely to be in a substantially non-equilibrium condition in the early phases before the phase transition. As the system develops, equilibrium is reached. The disturbances are reduced after hadronization, and the system continues its path toward equilibrium. As a result, the q values, representing the system's departure from the equilibrium state, will be different in the partonic state than in the hadronic state.

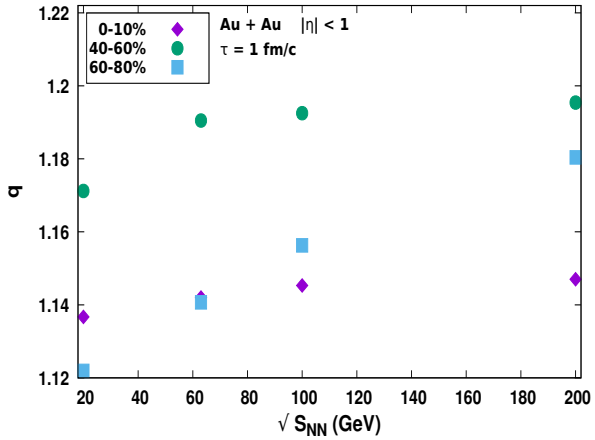

FIGURE 4.6: This plot shows the variation of q for different $\sqrt{s_{NN}}$ values at different centralities for Au + Au collisions. Here $|\eta| < 1$ and $\tau = 1 fm/c$.

It is also found that the q values depend on the beam energy [30]. Fig. 4.6 displays the change in q for various $\sqrt{s_{NN}}$ values at various centralities. According to Figs. 4.5 and 4.6, the entropic index is lower at lower $\sqrt{s_{NN}}$. But the relationship depends on how central the collisions are. The q values for most peripheral collisions (60-80%) are less than the q values for most central collisions (0-10%) below 100 GeV, as can be shown in Fig. 4.6. The opposite is true above 100 GeV. In a recent study (ref. [31]), the same outcome was also attained using experimental data. The authors have fitted the experimental data from the Au + Au collision at RHIC energies [32, 33] as well as data from the PHENIX collaboration [34]. They have also recognized how the q parameter is affected by collision energy and centrality. Also, the total change in the q value for most central and mid-central collisions is significantly less than the overall change in peripheral collisions. This suggests that the entropic index is not only determined by the multiplicity alone.

Fig. 4.7 illustrates how q varies with proper time (τ) and various collision energies. However, this only represents the calculation of the entropic index at various intervals and not a change of the system over time. The plot shows that the q value appears to peak at roughly 3 fm/c and then declines as τ increases. Different values of $\sqrt{s_{NN}}$ have little effect on the fundamental nature. A decreasing value of q indicates that the system is getting close to equilibrium. However, given that we are employing the AMPT model, the rise and fall in the q value may be attributed to changes in the particle's energy density. The energy density of the particles generated by the AMPT model typically grows up to $3 - 4$ fm/c and then steadily declines after that [35]. The entropic index exhibits comparable behavior because it is derived from the energy density.

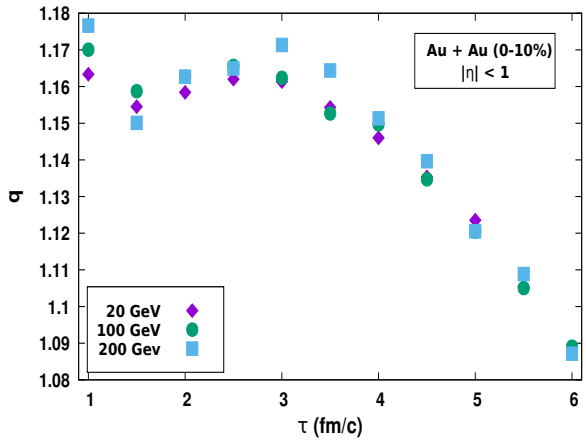

FIGURE 4.7: This plot shows the variation of (q) with proper time (τ) at different collision energies ($\sqrt{s_{NN}}$) for Au + Au collisions at $|\eta| < 1$ and for (0-10%) centrality.

4.5 Summary and Conclusions

In this chapter, we show that it is possible to examine the partonic stages of relativistic heavy ion collisions by combining a non-extensive formalism with a transport model. We have demonstrated the partonic phase's temperature fluctuations. Once the system has been partitioned into smaller grid cells, the ideal gas energy density - temperature relation is used to determine the temperature in these smaller subsystems. All the temperatures in these smaller subsystems should have been the same for an ideal gas in equilibrium. However, we discover that the system's overall temperature is not the same in the smaller grid cells. This suggests that the system is out of equilibrium. We determine the temperature fluctuations between various grid cells and plot the temperature fluctuations of the system during its early phases. For a system with fluctuating temperature, if the inverse of the temperature β can be fitted with a χ^2 distribution, the Tsallis statistics can be used to study the temperature fluctuations of an out-of-equilibrium system. The entropic index q is calculated using the β acquired from our simulations after it has been fitted with a χ^2 distribution.

In line with earlier studies, we find a linear relationship between the entropic index q and the system's effective temperature T_{eff}. However, the type of particles used to determine the system's temperature affects the slope of the line. Although this correlation has been demonstrated in the past, it was in the hadronic phase. We demonstrate that the partonic phase also exhibits an analogous relationship. The slope is different in the two cases as the underlying systems are different.

We have analyzed the connection between the entropic index and space-time rapidity, collision energy, and collision centrality. We observe that as space-time rapidity increases, the entropic index rises as well. This may be related to particle multiplicity, as a larger particle multiplicity produces a lower q value. But multiplicity alone cannot account for the variance of the entropic index, as we have seen by considering the other factors. The entropic index depends on collision energy and centrality. For different centrality ranges, the relationship is convoluted with the collision energy. For most central and mid-central collisions, the range of q is nearly constant between 20 - 200 GeV. However, for peripheral collisions, the range of q increases in the same collision energy range. Furthermore, the q values for central and peripheral collisions are almost identical in the $40 - 80$ GeV range. Below this range, the central collision's q values are greater than the peripheral collision's q value. The q value for central collisions is smaller than the q value for peripheral collisions beyond 80 GeV. These results are in line with more recent transverse momentum data analysis that used Tsallis statistics for the hadronic stage. We also study how the temperature fluctuates at different times. In this case, the change in entropic index corresponds to the variations in energy density from the AMPT model for relativistic heavy ion collisions.

Finally, we have shown how the entropic index show similar behavior with system parameters in both the partonic and the hadronic phase. However, it is not easy to obtain the thermodynamic variables such as temperature for an out-of-equilibrium system. The assumption of local thermal equilibrium and the correct choice of the equation of state can make this process more effective in finding the system's equilibrium limits.

Bibliography

[1] Kurkela A, Mazeliauskas A, Paquet JF, Schlichting S, Teaney D. , Phys. Rev. Lett. **122**, 122302 (2019).

[2] K. Paech and A. Dumitru, Phys. Lett. B **623**, 200-207 (2005).

[3] Ágnes Mócsy and Paul Sorensen, Nucl. Phys. A **855(1)** 241-244 (2011).

[4] V. Chandra, V. Ravishankar, Eur. Phys. J. C **59**, 705-714 (2009).

[5] A. Bhattacharyya, P. Deb, S. K. Ghosh, R. Ray, and S. Sur, Phys. Rev. D **87**, 054009 (2013).

[6] Sumit Basu et. al. Phys. Rev C **94**, 044 901 (2016); Sumit Basu et al. AIP Conference Proceedings **1701**, 060004 (2016).

[7] Bhattacharyya, T., Garg, P., Sahoo, R. et al. Eur. Phys. J. A **52**, 283 (2016).

[8] Fernando G. Gardim, Frédérique Grassi, Pedro Ishida, Matthew Luzum, Pablo S. Magalhães, and Jacquelyn Noronha-Hostler, Phys. Rev. C **97**, 064919 (2018).

[9] Peter W. Egolf and Kolumban Hutter, Entropy **20(2)**, 109 (2018).

[10] Azmi, M.D., Cleymans, J. Eur. Phys. J. C **75**, 430 (2015).

[11] Zebo Tang, Yichun Xu, Lijuan Ruan, Gene van Buren, Fuqiang Wang, and Zhangbu Xu, Phys. Rev. C **79**, 051901 (2009)(R).

[12] Rui-Fang Si, Hui-Ling Li, Fu-Hu Liu, Advances in High Energy Physics, vol. **2018**, Article ID 7895967, 12 pages, (2018).

[13] H. Zheng and Lilin Zhu, Advances in High Energy Physics **2015**, Article ID 180491 (2015).

[14] S. M. H. Wong, Phys. Rev. C **54**, 2588-2599,(1996).

[15] Y. Zhang, J. Zhang, T. Chen, D. Liu, and Y. Chao, Phys. Rev. C **96**, 044914 (2017); Rajeev S. Bhalerao, A. Jaiswal, and S. Pal, Phys. Rev. C **92**, 014903 (2015).

[16] J. Casas-V´azquez and D. Jou, Rep. Prog. Phys. **66**, 1937–2023 (2003).

[17] Sumit Basu et al. J. Phys.: Conf. Ser. **668**, 012043 (2016).

[18] G. Wilk and Z. Wlodarczyk, Phys. Rev. C. **79**, 054903 (2009).

[19] J. Cleymans, G. Hamar, P.Levai and S. Wheaton, Journal of Physics G: Nuclear and Particle Physics, 36 (2009).

[20] A. Simon and G. Wolschin, Phys. Rev. C **97**, 044913 (2018).

[21] Carolina Barboza Mendoza and G. Herrera Corrala, Eur. Phys. J. A **55**, 146 (2019).

[22] E. Megías, D. P. Menezes, and A. Deppman, Physica A: Statistical Mechanics and its Applications 421, 15-24 (2015); P.H. Cardoso, T.N. da Silva, A. Deppman, and D.P. Menezes, Eur. Phys. J. A **53(10)**, 191 (2017).

[23] S. Mitra, Eur. Phys. J. C, **78**, 1, 66 (2018).

[24] T. S. Biró, G. G. Barnaföldi1, P. Ván, Eur.Phys. J. A **49**, 110 (2013).

[25] C. Beck, Europhys. Lett. **57** (3), 329-333 (2002).

[26] A.S. Parvan, Eur.Phys. J. A **53**, 53 (2017); A.S. Parvan and T. Bhattacharyya, Eur. Phys. J. A **56**, 72 (2020).

[27] B. De, S. Bhattacharyya, G. Sau and S. K. Biswas, Int. J. Mod. Phys. E **16**, 1687 (2007).

[28] K. Shen, G. G. Barnaföldi and T.S. Biró, Universe 2019, 5(5), 122; (2019).

[29] G. Bíró, G. G. Barnaföldi1, T. S. Biró and K. Urmossy, J. Phys. G: Nucl. Part. Phys. **47**, 105002 (2020).

[30] B. Abelev et al., (ALICE Collaboration), Phys. Lett. B **717**, 162 (2012).

[31] Rajendra Nath Patra, Bedangadas Mohanty, Tapan K. Nayak, Eur. Phys. J. Plus **136**, 702 (2021).

[32] L. Adamczyk et al., (STAR Collaboration), Phys. Rev. C **96**, 044904 (2017).

[33] J. Adam et al., (STAR Collaboration), Phys. Rev. C **101**, 024905 (2020).

[34] S. S. Adler et al., (PHENIX Collaboration), Phys. Rev. C **69**, 034909 (2004).

[35] J. Xu, C.M. Ko, Phys. Lett. B **772**, 290–293 (2017).

Chapter 5

Machine Learning model driven prediction of the initial geometry parameters

5.1 Introduction

In this chapter, we will give a detailed representation of the use of machine learning methods in predicting various geometry parameters of heavy ion collision experiments. By utilizing supervised Machine Learning (ML) techniques, we show excellent prediction accuracy of three crucial features that affect the initial geometry of the heavy-ion collision (HIC) studies. These variables are the impact parameter, the participant eccentricity, and the eccentricity. Using thorough parameter scans, we examine various machine learning (ML) algorithms, their error spectra, and sampling techniques to identify an effective algorithm and tuned training set that provides multi-fold improvements in accuracy for three different heavy-ion collision simulation models. The three models are a transport model, a hydrodynamic model, and a hybrid model. Three different HIC models were used to demonstrate that, even when a model is trained using a transport model, it can still produce reliable results for hydrodynamic and hybrid models. We show how the centrality of the collision affects the impact parameter prediction's accuracy. For central collisions, prediction accuracy using conventional ML training techniques is very low. We discuss how errors can be reduced, and accuracy can be greatly increased in all ranges of impact parameter and eccentricity predictions.

Different collision systems and other initial conditions create different initial parton distributions, which impact the final particle spectra and anisotropic flows [1]. The primary

outcomes of these experiments are the transverse momentum (p_T) spectra, rapidity (y) spectra, pseudorapidity (η) spectra, particle-antiparticle ratios, jet momentum distribution, and multiplicity fluctuations. Direct inferences about some phenomena, such as anisotropic flows, can be derived from these data. However, some parameters are challenging to determine directly from the experimental results. These include impact parameter and initial geometry parameters such as eccentricities, event plane angles, etc. The details about these parameters are described in Chapter I. The collision centrality is measured by the impact parameter. In experiments, the data is always analyzed with respect to the collision's centrality since different collisions with different collision centrality produce different spectra.

The collision centrality significantly influences the final particle spectra. It has been observed that the distribution of particle multiplicity depends on the centrality of the collision. The multiplicity fluctuations at various centralities are probed at RHIC energies in ref. [2, 3], and in ref. [4–6], the same phenomena are addressed at collision energies of 2.76 TeV, 5.02 TeV, and 5.44 TeV, respectively. Although the centrality cannot be determined from experiments independently, it can be computed using theoretical modeling such as the Glauber model (ref. [7]) or other similar models. Other initial state geometry parameters also suffer from the same issue. Because of this, there are different methods to establish these parameters. Neural networks have also been considered in addition to other simulations and methods to calculate the impact parameter from the experimental data [8].

The impact parameter in the Glauber model is related to the multiplicities of charged particles created during the heavy ion collision. Hard and soft collision processes contribute to the multiplicity of charged particles. These, in turn, depend on the total number of participants as well as the number of binary collisions. The charged particle multiplicity per unit pseudorapidity can be stated as,

$$\frac{dN_{ch}}{d\eta} = n_{pp}\left[(1-x)\frac{N_{part}}{2} + xN_{coll}\right] \tag{5.1}$$

Here, n_{pp} is the multiplicity per unit rapidity in pp collisions, x is the fraction of contribution from hard processes, and n_{coll} is the total number of binary NN collisions. The impact parameter can be used to specify the number of participant nuclei N_{part} [7, 9]. If $T_A(s)$ is the thickness function of nucleus A, i.e., the probability density function of finding nucleons in A, then the number of participants in A at the transverse position s can be found out by multiplying with the probability of binary nuclei-nuclei collision with the nucleons of the nucleus B at the same position $(b-s)$ where b is the impact

parameter. So, the total number of participants can be expressed as,

$$N_{part}(b) = \int T_A(s)(1 - exp[-\sigma_{inel}^{NN} T_B(b-s)])ds + \int T_B(b-s)(1 - exp[-\sigma_{inel}^{NN} T_A(b)])ds \quad (5.2)$$

Here, the contribution from nuclei A and B is combined to determine the total number of participating nuclei. The impact parameter and corresponding centrality can be calculated by fitting the multiplicity spectra using Eq.5.1 and Eq.5.2. For each event, multiplicity fitting must be performed in order to determine its centrality in this method. Utilizing machine learning models can be a more straightforward method of obtaining centrality. In several papers [10–12], machine learning has been used to extract the impact parameter from the experimental data. We can automate the entire procedure and determine the impact parameter effectively by using machine learning. Machine learning (ML) has the advantage of requiring less computational time and power. Thus, the process becomes more efficient. Most of the research in this field uses deep neural network techniques. Predictions for the impact parameter have also been made using the convolutional neural network (CNN) [13]. The first research to show the impact of neural network analysis on enhancing the impact parameter's accuracy is ref. [14]. However, these networks need to be tuned for hundreds of different parameters. This increases the cost of the process in terms of computation. On the other hand, several non-neuronal ML models, such as SVM, RandomForest, kNN, etc., need fewer parameters to give results as accurately as the ANN or CNN models. So, various standard machine learning techniques are also implemented to get the impact parameter in several studies.

In this chapter, we have analyzed various machine learning (ML) algorithms and conducted a thorough comparison of the accuracy and efficiency of these algorithms. This has been done by using well-defined machine learning methods and to indicate a significant gap in their prediction accuracy for central collisions. We evaluate the prediction accuracies and talk about the factors that contributed to them. We find that for the low-impact parameters, accuracy is lower. This is a well-known issue in computing the impact parameter using ML methods. We offer a unique sampling technique that significantly outperforms the standard sample techniques employed by the ML community.

Our study would concentrate on predicting the impact parameter and the eccentricity. Eccentricity is one of the anisotropy parameters that provide us with the initial geometrical distribution of the collision region. This also impacts the elliptic flow, one of the key observables used to analyze the collective behavior of the produced particles in

heavy-ion collisions. The effects of eccentricity fluctuation on the elliptic flow are addressed in ref. [15] at $\sqrt{s_{NN}} = 200$ GeV for Au-Au and Cu-Cu collisions. In ref. [16], the effect of various initial anisotropy components on the flow harmonics is studied using the AMPT model. The initial state anisotropy can be expressed as[9],

$$\epsilon_n(b) = \frac{< r^n cos(n\phi - n\psi) >}{r^n} \tag{5.3}$$

here $r = \sqrt{x^2 + y^2}$, $n = 2$ represents the eccentricity, and $n = 3$ represents the triangularity. The aforementioned eccentricities are observed with respect to the reaction plane. Additionally, we have trained the algorithm to predict participant plane eccentricity [15],

$$\epsilon_{part} = \frac{\sqrt{\sigma_y^2 - \sigma_x^2 + 4\sigma_{xy}^2}}{\sigma_y^2 + \sigma_x^2} \tag{5.4}$$

here σ's are the variances of the positions of the particles, $\sigma_x^2 =< x^2 > - < x >^2$, $\sigma_y^2 =< y^2 > - < y >^2$ and $\sigma_{xy} =< xy > - < x >< y >$. Here $< .. >$ is the average over the transverse plane.

In this work, the transverse momentum spectra are used as features, and the target variables that the model must predict are the impact parameter, eccentricity, and the participant eccentricity. The p_T spectra of Au-Au collision events at 200 GeV collision energy are generated using the AMPT model. In our study, the ML models utilized the learnings and experiences from impact parameter prediction to estimate eccentricity. We have also examined how the impact parameter's inclusion as a feature improves the eccentricity prediction accuracy.

AMPT is a transport model which has been widely utilized to model the various stages of the HIC. But it has its shortcomings, just like every model. In addition, some hydrodynamics-based models produce accurate results that are in good agreement with the data. In this study, we used a particular HIC model for training and two different HIC models' data for making predictions. This shows that predictions obtained using the ML model for the impact parameter for a set of well-defined training data are model-independent. The two other HIC models that we use in this study are VISH2+1(Viscous Israel Stewart Hydrodynamics (2+1) dimension) [17] and a hybrid model comprised of a hydro evolution model, and a hadronic cascade model [18]. The details of these models are given in Chapter I. The AMPT model, used to train ML algorithms, is very distinct from these two models. Because of this, the ML models are trained using the p_T spectrum and impact parameter data from AMPT events, and they predict impact parameters using test p_T spectra data from the VISH2+1 and the hybrid model. We

set up various models with different initial conditions to produce the p_T spectra comparable to those obtained in the actual experiments. Therefore, the model independence only applies to models that produce p_T spectra similar to the experimental p_T spectrum.

We discuss the ML models utilized in this chapter in section II. We also go over the criteria used to evaluate the accuracy of various ML models. This section also provides information on the setting of the hyperparameters as well as the learning process of various algorithms. To increase the precision of the predictions, we have also employed rebalancing procedures. This section goes through these balance methods. The results and forecasts from the ML models of the participant eccentricity and eccentricity are discussed in Section III. It also talks about the eccentricity ranges where the best accuracy has been seen. This section discusses the effectiveness of impact parameter prediction utilizing experimental data and unknown data from several HIC models. Finally, we show how rebalancing the dataset can enhance the accuracy of the predictions. We then summarize the study in section IV.

5.2 Machine Learning Methods

5.2.1 ML Algorithms and Tuning of Hyperparameters

As stated in the introduction, we tested several machine learning (ML) methods for this study, including k-Nearest Neighbors, Gradient Boosting Regression, and Decision Trees. Reference [19] provides further information on these ML algorithms. Standard metrics such as R-square, the Root Mean Square Error (RMSE), the Mean Squared Error (MSE), and the Mean Absolute Error have been used to test the efficiency of these models (MAE). After testing multiple ML models, we found that while all of them provide excellent predictions for the impact parameter, only three of them are effective at predicting the eccentricity. Therefore, we solely focus on these three algorithms. They are the Random Forest Regressor (RF), ExtraTrees Regressor (ET), and k-Nearest Neighbors (kNN) models. In the kNN model, the target variable is predicted by performing a local interpolation between the target and its k nearest neighbors in the training dataset [20]. The other two models are based on ensemble techniques. In RF, decision trees are created during training, and an ensemble mean is computed [21]. In ET, randomized decision trees constructed from sub-samples of the training dataset are taken into consideration [22]. To get a reliable estimate of the parameters, we performed a 10-fold cross-validation (CV) [23]. Additionally, it provides a bias-variance trade-off.

As we utilized these ML techniques to analyze the data from three different HIC models, we standardized the data before processing it. The charged particle p_T spectra are used as features in the dataset for this study. The p_T spectra are obtained for a rapidity window of -0.5 to 0.5. The range of values in each of the p_T bins varies. The difference is more noticeable when we compare a lower p_T bin with a higher p_T bin. Therefore, it is crucial to standardize them. This allows the model to work with new data from a different HIC model. In this study, two different scaling methods are employed, i)the Standard Scaler or Z-score normalization and ii) the Min-Max Scaler [24]. The data is scaled in the standard scaler or Z-score normalization approach so that every feature has a mean of 0 and a standard deviation of 1. It is done by using Eq. 5.5,

$$x_{standard} = \frac{x - mean(x)}{standard\,deviation(x)} \tag{5.5}$$

In this case, the original data is x, and the scaled data is $x_{standard}$. When using Min-Max Scaling, each feature's distribution is rescaled between 0 and 1.

$$x_{normalized} = \frac{x - min(x)}{max(x) - min(x)} \tag{5.6}$$

We have used Python sklearn.preprocessing package to implement both of these scaling methods [25]. In most of the examples presented in this study, we find that the Z-score method gives us an accuracy of $4-6\%$ better than that of min-max scaling. Therefore, we have always applied the Z-score normalization.

Only the p_T spectra are used as feature variables when the impact parameter is given as the target variable. For the other targets, the predicted impact parameter is included in the dataset as a feature variable, as all the other targets depend on the impact parameter. Thus, the p_T spectra can be used as the primary input to measure the dependent variables. The data is separated in the training and test set to evaluate the model.

It is crucial to have a sufficient number of events in order to attain the best accuracy without using too much computing costs. The learning curve indicates how well the model is performing. We represent the learning of ML models as a function of events. The learning curves of a kNN (green circles), ET (orange triangles), and RF (blue stars) model are given in Fig. 5.1, where the number of event iterations is used to reflect changes in the CV accuracy. Only the kNN model's training score curve (sky color circles) is displayed; it illustrates the model's accuracy in fitting the training set data. In the training case, the accuracy reaches saturation around 3000 events relatively quickly. In contrast, the test data accuracy saturates at 6000 to 8000 events shown by other

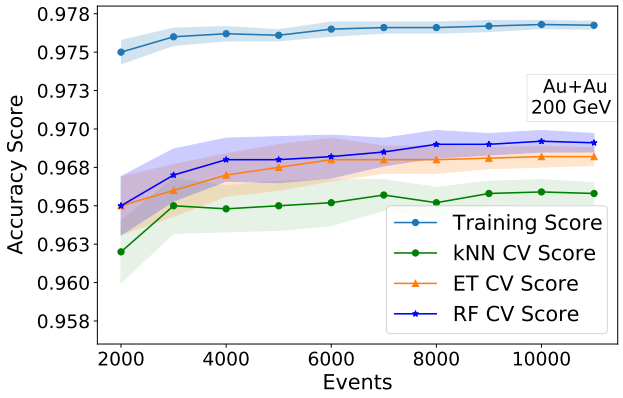

FIGURE 5.1: The learning curve of kNN(green dots), ET (orange triangles), and RF (blue stars) model. The shaded region is the standard deviations

curves. So, the learning process in this study is obtained over 10000 events.

Model	R^2	**MAE**	**RMSE**
Gradient Boosting Regressor [27]	0.9709	0.3834	0.4819
Light Gradient Boosting Machine [28]	0.9702	0.3878	0.4876
Random Forest Regressor [21]	0.9689	0.3972	0.4984
Extra Trees Regressor [22]	0.968	0.4024	0.5048
AdaBoost Regressor [29]	0.9676	0.4049	0.5079
K Neighbors Regressor [20]	0.9649	0.4226	0.5295
Linear Regression [26]	0.9642	0.422	0.5341
Ridge Regression [30]	0.9642	0.422	0.5341
Least Angle Regression [31]	0.9642	0.422	0.5341
Huber Regressor [32]	0.9642	0.4216	0.5346
Bayesian Ridge [33]	0.9642	0.422	0.5341
Orthogonal Matching Pursuit [34]	0.9635	0.4272	0.5398
Decision Tree Regressor [35]	0.9405	0.5503	0.6888
Passive Aggressive Regressor [36]	0.8849	0.7482	0.9058
Lasso Regression [37]	0.7461	1.1484	1.4246
Elastic Net [38]	0.6253	1.4093	1.7305

TABLE 5.1: 10-Fold cross-validation accuracy of ML models for b predictions of min. bias Au-Au events at $\sqrt{s} = 200$ GeV

We show the efficiency of the standard ML models for impact parameter prediction in Table—5.1. The accuracy plots for impact parameter predictions using the kNN(a), ET(b), RF(c), and Linear Regression(LR)(d) models are given in Fig.5.2. The charged particle p_T spectra from the AMPT-SM model are used to train the machine learning models. The linear regression algorithm determines how a dependent variable and one or more independent variables are linearly related [26]. A test dataset with p_T spectra from more than 4000 minimum bias Au+Au collision events at 200 GeV is used to make the prediction. Here, the red line represents the line of optimum accuracy, and the

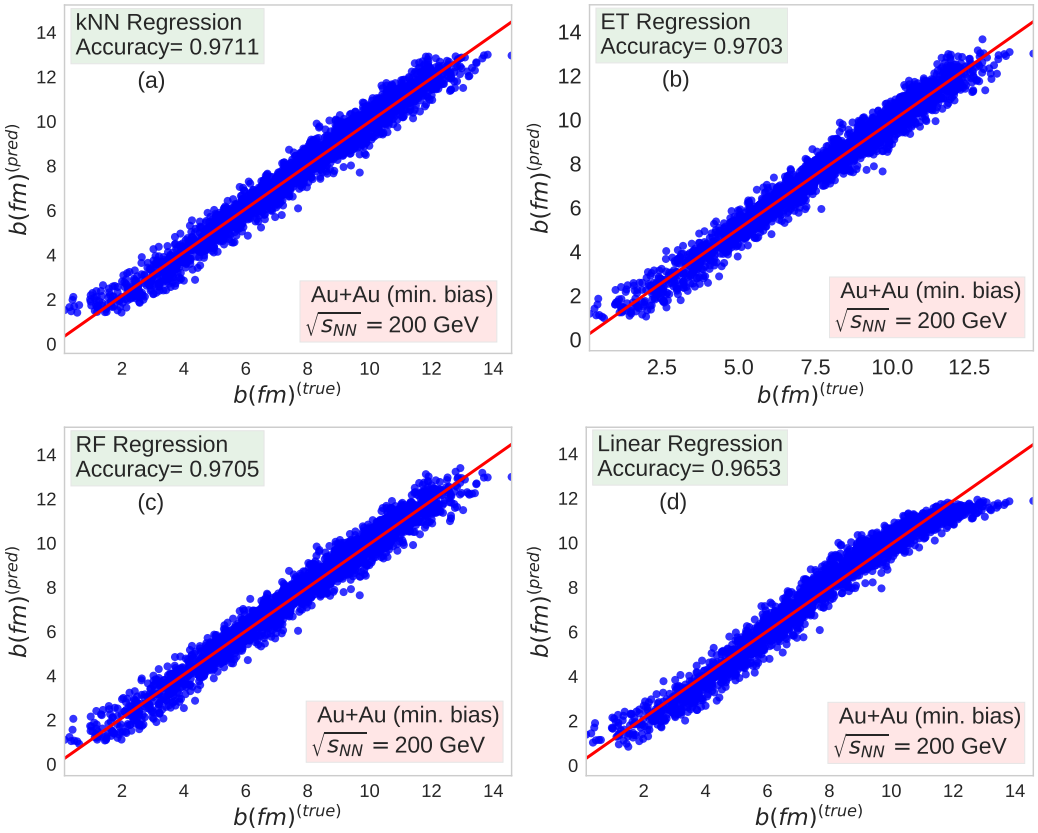

FIGURE 5.2: Impact parameter prediction using kNN(a), ET(b), RF(c) and LR(d) model with their accuracy score 97.11%, 97.03%, 97.05% and 96.53% for events of Au+Au system at collision energy 200 GeV. These plots are obtained for a random train and test set split of input events.

blue points represent the model's predictions. For kNN, ET, RF, and LR, the accuracy values are 97.11%, 97.03%, 97.05%, and 96.53%, respectively. For a random train-test dataset split, all of these accuracy results are observed, and the 10-fold cross-validation scores for these models are 97.04%, 97%, 97.01%, and 96.56% respectively. When the ML models are trained using the default AMPT model data, we get an accuracy of more than 95% for the kNN, ET, and RF models. With the exception of some critical impact parameter regimes, the majority of machine learning methods provide a reasonable level of accuracy for impact parameter prediction without tuning any of the hyperparameters.

It is well known that hyperparameter choices can impact an ML model's accuracy. We do hyperparameter tuning to adjust the parameters with the least amount of error on the validation set. The variation in a kNN model's accuracy is represented as a function of the number of nearest neighbors hyperparameter in Fig. 5.3(a). The impact parameter is used as the target variable, and the model is trained using 12,000 minimum bias Au+Au collision events for each configuration. The model's accuracy is at its maximum

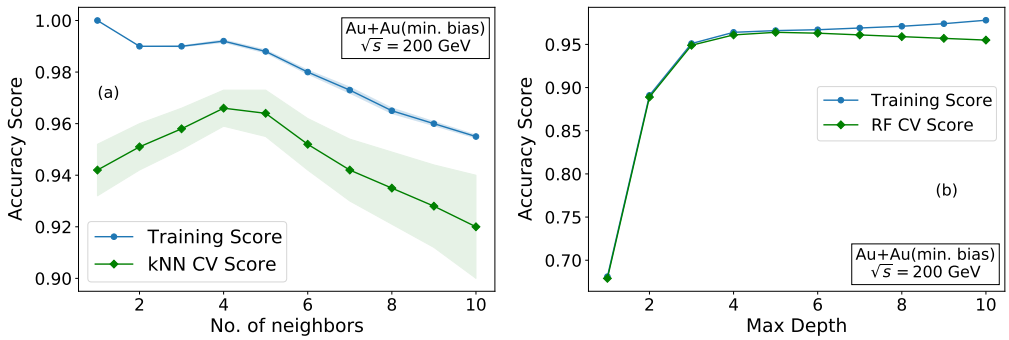

FIGURE 5.3: Change in accuracy as a function of hyperparameters. a) kNN model with the number of nearest neighbors hyperparameter, b)Random Forest with max depth hyperparameter

when there are $4-5$ nearest neighbors. The green curve displays the 10-fold cross-validation score, and the shaded area represents the standard deviation. When the number of nearest neighbors is 1, the training score shown by the blue line has a score of 1.00. Overfitting occurs in this situation. For the RF model, the maximum number of levels of the trees is the key hyperparameter (see Fig. 5.3(b)). We observe that for the hyperparameter value of $4-5$, the accuracy saturates. Similar to the RF model, when the max-depth hyperparameter is $4-5$, we obtain the highest CV score for the ET model. Although the aforementioned parameters are the ones that affect accuracy the most, we adjust the other hyperparameters by using the RandomSearchCV function of the sklearn library and evaluating accuracy for various combinations of hyperparameters.

As previously mentioned, Fig. 5.4 shows how the impact parameter's inclusion as a feature increases the efficiency of eccentricity prediction. As has been found in previous studies, eccentricity is dependent on the collision's centrality. We have shown that adding the impact parameter as a feature improved accuracy across all the centrality ranges.

By identifying the strongly correlated features in the training data, the errors in the ML model predictions can be minimized. According to ref. [39], the Principal Component Analysis (PCA) is the most often used method for reducing the number of features in a large dataset. In this study, we attempted to eliminate colinearity using the PCA approach and the "SelectFromFeature" function from the Sklearn package. We compared the results to the accuracy that had already been attained utilizing all the features. We displayed the PCA method's results here. The accuracy score of a kNN model is shown in Fig. 5.5(a), and the accuracy score of an ET model is shown in Fig. 5.5(b) with respect to the number of principal components employed. Here, the accuracy of b predictions is evaluated using a dataset of 12000 minimal bias Au-Au collision events at $\sqrt{s_{NN}} = 200$ GeV. For the usage of 7 or more principal components, the accuracy

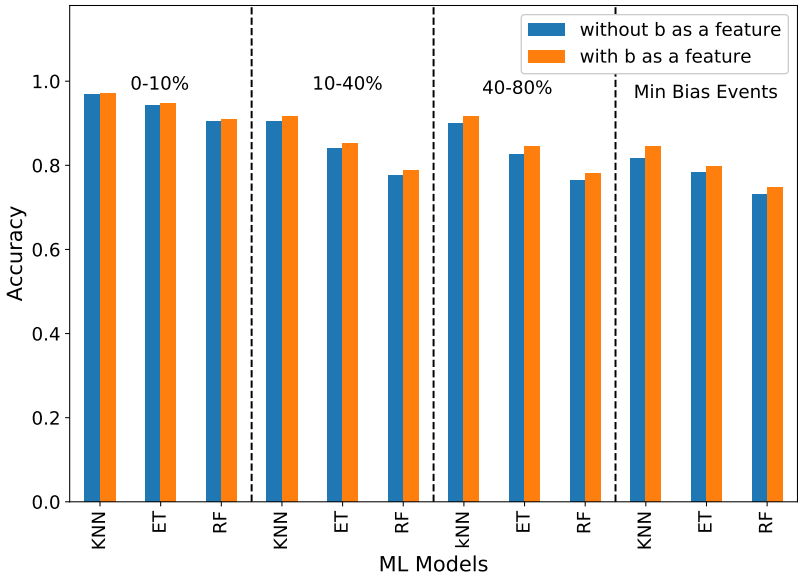

FIGURE 5.4: Effect on the eccentricity prediction accuracy by the inclusion of impact parameter as a feature for different centrality(%), a) 0-10%, b) 10-40%, c) 40-80%, d) Min. bias events. The orange bar represents accuracy with impact parameter as a feature and blue bars represent accuracy without impact parameter as a feature.

score reaches saturation in both cases. For impact parameter predictions, a variance coverage of 95% can be attained with only 7 components. Therefore, it is safe to employ $7-8$ principal components to acquire a good amount of precision without compromising any significant information. The impact parameter was determined using $7-8$ principal components. We also observed that in order to get an appropriate result for the eccentricity and participant eccentricity prediction, at least 10 features or 10 principal components are required. Given that we are using transverse momentum data, this is to be expected. We require fewer features to achieve a high degree of prediction accuracy for the impact parameter than for the eccentricity because the impact parameter is known to be associated with the transverse momentum data [40]. We will utilize the PCA function to convert the features in all eccentricity estimations.

5.2.2 Custom resampling for unbalanced training set

The p_T spectra datasets that we have employed as a feature for ML model training are unbalanced. There are fewer events for lower impact parameter values since we have taken into account the p_T spectra of minimal bias events. This results in a left-skewed event distribution of p_T spectra. The eccentricity and impact parameter prediction accuracy in the lower b region ($b \leq 1\ fm$) are both impacted by the data imbalance.

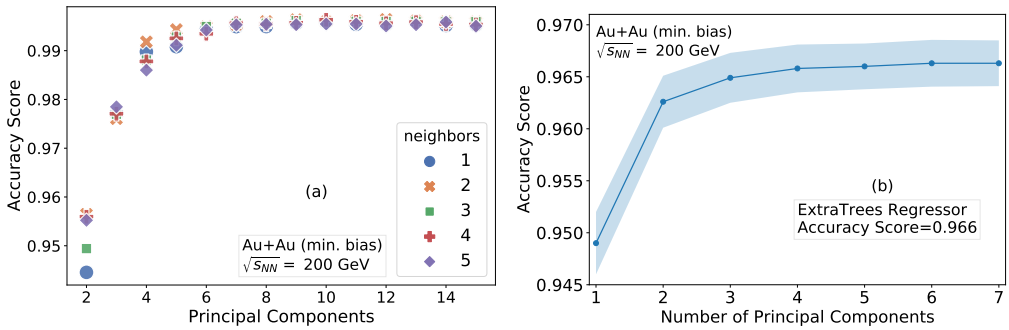

FIGURE 5.5: a) Accuracy of a a) kNN model and b) an ET model as a function of the number of principal components used

The impact parameter is not immediately accessible to the experiments. However, most experimental observables depend on the impact parameter, in ref. [41], Bass et al. have observed that the various methods of impact parameter estimation are often optimized for the wider impact parameter range. Because of this, the experimental results for head-on collisions corresponding to the lower impact parameter range will have higher inaccuracies. We aim to improve the prediction accuracy of the impact parameter in the lower impact parameter range. This is crucial because there are a lot of experimental findings from head-on collisions that can be more effectively analyzed with better impact parameter predictions in the lower b range. Our objective is to balance the data set suitably in order to increase the prediction accuracy in the lower b range.

A few sampling techniques are used in machine learning to rebalance a dataset, such as SmoteR, ADASYN, etc. [42, 43]. The minority and majority data classes are increased (over-sampled) or decreased (under-sampled), respectively, using the nearby data points in the training dataset. With every feasible set of hyperparameters, we tested both methods. The results are reported in the following section (Section IV C). We find that the improvement in accuracy is not adequate. After that, we use a technique called class weights to rebalance the data set, where different classes represent various impact parameter regimes. A thorough grid search was conducted to analyze the various weight and distribution region combinations. The events with an impact parameter of $<= 1.0$ fm were chosen to be in category 1 and the others to be in category 2 based on the test set minimal error. The weights given to the two classes are $4 : 1$. This technique has further helped us reduce errors. The results are presented in the following section (subsection C).

5.3 Results and Discussions

5.3.1 Impact parameter and eccentricity prediction

As was previously mentioned, eccentricity is one of the crucial factors in heavy-ion collisions that describes the initial state geometry. However, it is challenging to determine eccentricity directly from the experiment, just like the impact parameter. The methods employed in this work for impact parameter prediction are also applied to predict eccentricity. The three ML algorithms that perform the best in eccentricity prediction are ET, kNN, and RF.

Similar to Table- 5.1, a comparison of performances of different models for eccentricity prediction is shown in Table-5.2. The other remaining models, which are present in Table- 5.1 but not in Table- 5.2, have R^2 score less than 60%. The models are again tuned for the best possible outcome. Most of the hyperparameters remain unchanged and whatever changes occurred are very near to the previously tuned hyperparameter value.

Model	R^2	**MAE**	**RMSE**	**MSE**
K Neighbors Regressor	0.9746	0.0021	0.0028	0
Extra Trees Regressor	0.9503	0.0029	0.0039	0
Random Forest Regressor	0.9143	0.0038	0.0051	0
Light Gradient Boosting Machine	0.8647	0.005	0.0064	0
Decision Tree Regressor	0.7353	0.0052	0.009	0.0001
Gradient Boosting Regressor	0.5855	0.0089	0.0112	0.0001

TABLE 5.2: 10-Fold cross validation accuracy of ML models for eccentricity prediction of min. bias Au-Au events at $\sqrt{s}$=200 GeV

The prediction plots of eccentricity using the kNN, ET, and RF model are shown in Fig. 5.6 (a), (b), and (c). The accuracy percentages are 97.84%, 95.47% and 91.95%, respectively. This is seen in a train-test dataset of min. bias Au+Au events that were randomly split. The models are tested over 2000 events displayed in Fig. 5.6 and trained using 12000 randomly chosen events. The 10-fold cross-validation scores are 97.52% for the kNN model and 95.18% for the ET model. These are also closer to the accuracies obtained using the random train-test split dataset. The 10-fold CV score of the RF model is 91.95%. When the ML algorithms are trained using the default AMPT model data, we achieve an accuracy of between 87% and 93% for kNN and ET models.

The prediction plots of eccentricity using the kNN, ET, and RF model are shown in Fig. 5.7 (a), (b), and (c). The accuracy percentages are 98.16%, 96.21% and 93.32%, respectively. One can observe a similar pattern between Fig. 5.6 and Fig. 5.7. The points spread away from the red line as the accuracy decreases from kNN to ET to

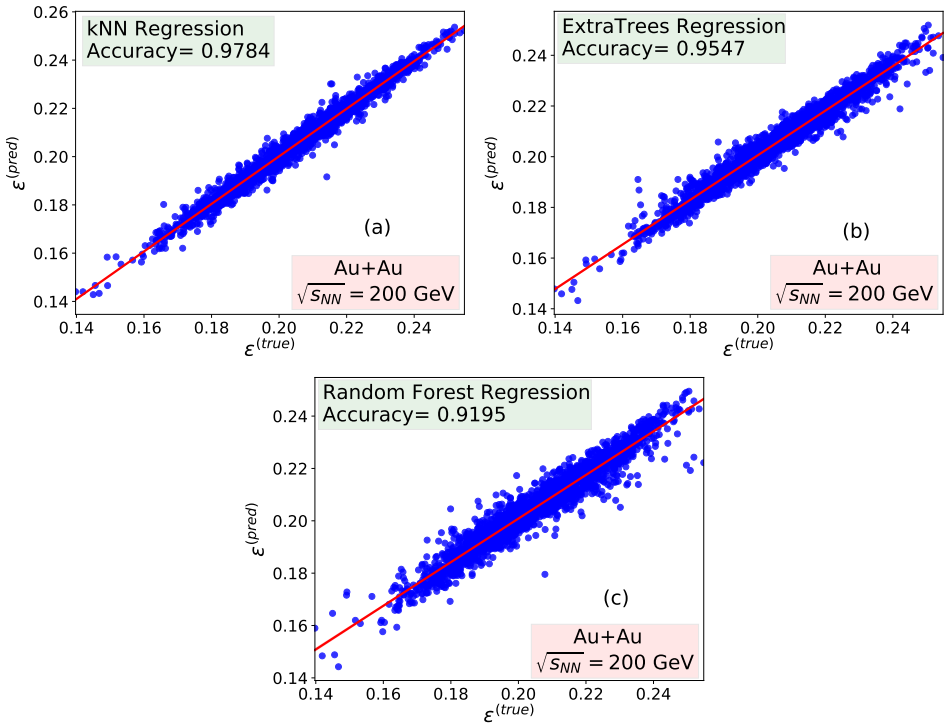

FIGURE 5.6: Eccentricity prediction using kNN(a), and ET(b) model with their accuracy score 97.84%, and 95.47% for events of Au+Au system at a collision energy 200 GeV. These plots are obtained for a random train and test set split of input events.

RF regression. In this case, the 10-fold CV scores are 97.58% and 95.25% for the kNN and ET model, respectively, and 93.78% for the RF model. A model comparison is also given in Table- 5.3 for participant eccentricity predictions using different machine learning models. The first four models have an accuracy of more than or equal to 90% among the eight given. The other remaining models which are present in Table-5.1 but not in Table-5.3, have R^2 score less than 50%.

Model	R^2	**MAE**	**RMSE**	**MSE**
K Neighbors Regressor	0.9791	0.0017	0.0023	0
Extra Trees Regressor	0.9571	0.0024	0.0033	0
Random Forest Regressor	0.9293	0.0031	0.0042	0
Light Gradient Boosting Machine	0.8931	0.004	0.0051	0
Decision Tree Regressor	0.7929	0.0043	0.0071	0.0001
Gradient Boosting Regressor	0.6682	0.0073	0.0091	0.0001
AdaBoost Regressor	0.5285	0.009	0.0108	0.0001
Least Angle Regression	0.4907	0.0092	0.0112	0.0001
Linear Regression	0.4906	0.0092	0.0112	0.0001

TABLE 5.3: 10-Fold cross validation accuracy of ML models for participant eccentricity prediction of min. bias Au-Au events at $\sqrt{s}$=200 GeV

An accuracy comparison for ϵ_3 (triangularity) prediction by ML models is presented in

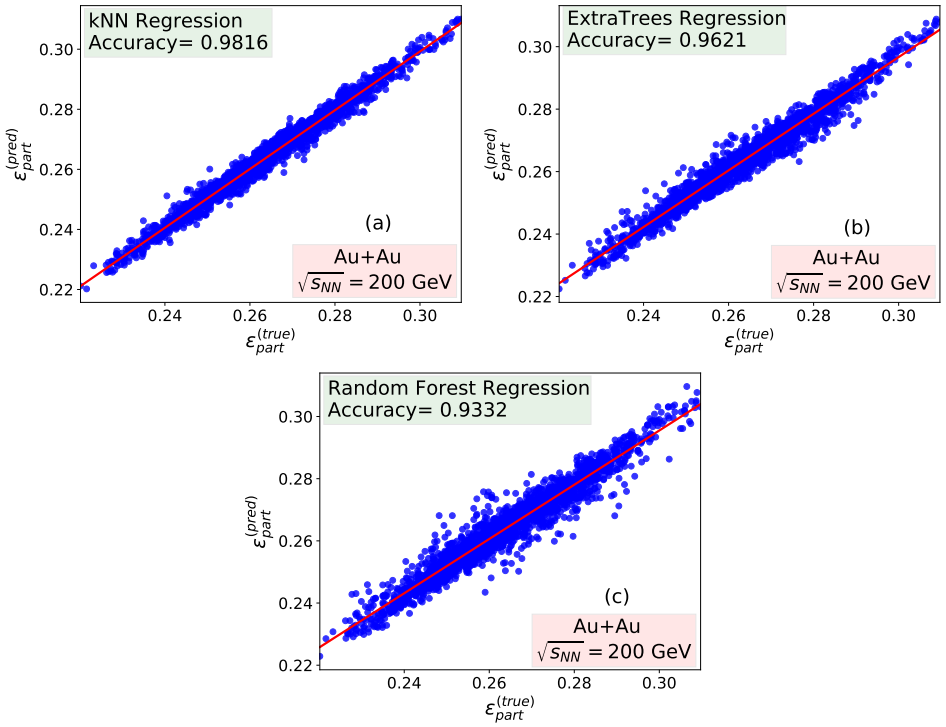

FIGURE 5.7: Participant eccentricity prediction using kNN(a), and ET(b) model with their accuracy score 98.16%, and 96.21% for events of Au+Au system at collision energy 200 GeV. These plots are obtained for a random train and test set split of input events.

Table- 5.4. We have computed ϵ_3 by using the Eq. 5.3. kNN, ET, and RF models outperform the other ML models in this instance as well. All three of them are more than 90% accurate. After 10-fold cross-validation, the LGBM (Light Gradient Boosting Machine) model also shows an accuracy of over 88%. This machine learning model is tree-based and grows vertically (leaf-wise) [28].

Model	R^2	**MAE**	**RMSE**
K Neighbors Regressor	0.9762	0.001	0.0013
Extra Trees Regressor	0.9574	0.0013	0.0017
Random Forest Regressor	0.9216	0.0017	0.0023
Light Gradient Boosting Machine	0.8807	0.0022	0.0029
Decision Tree Regressor	0.7581	0.0024	0.0041
Gradient Boosting Regressor	0.6309	0.004	0.005

TABLE 5.4: 10-Fold cross-validation accuracy of ML models for ϵ_3 predictions of min. bias Au-Au events at $\sqrt{s} = 200$ GeV

A narrow range of eccentricity $(0.22 - 0.32)$ is used for the model fitting and predictions in the eccentricity prediction figures (ref Fig. 5.7). This region is specifically where all of the models get their highest estimation accuracy. This is because the eccentricity distribution over the events is not isotropic. The ϵ_{part} distribution is given in Fig. 5.8(a).

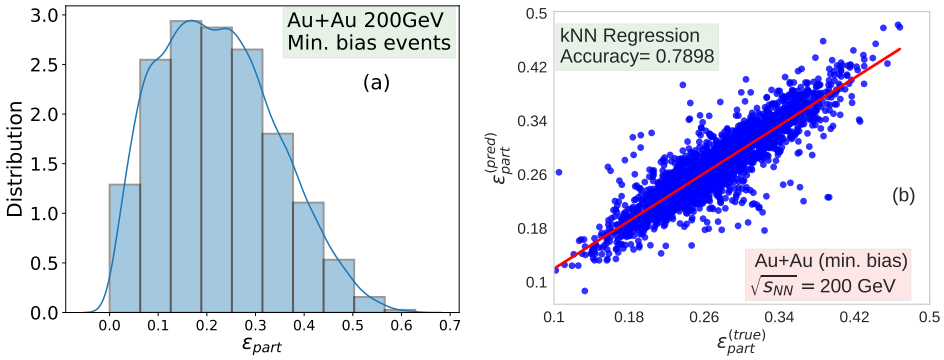

FIGURE 5.8: a) Histogram plot of participant eccentricity distribution and b) Prediction plot of ϵ_{part} for higher ϵ_{part} range using kNN model of minimum bias Au-Au collision events at $\sqrt{s} = 200$ GeV given by the AMPT model

Here, the x-axis indicates the eccentricity range, and the y-axis denotes the normalized number of events. Eccentricities between 0.15 and 0.25 are observed to have the highest peak in the distribution. As a result, the distribution is skewed, which makes our dataset unbalanced. Therefore, the eccentricity of most events falls within a specific range. Since there are more fitting points, the model fits well in this range of eccentricity. The graph shows that the eccentricity range can be expanded further from 0.1 to 0.5. An estimation plot of ϵ_{part} using the kNN model is provided for a wider range in Fig. 5.8(b). Here, events with ϵ_{part} between 0.1 and 0.5 are taken into consideration. As a result, the range is now three times wider than in the earlier situations. In comparison to the points in Fig. 5.7 (a), we see that the points are broader away from the center and the optimum accuracy line. Additionally, we observe some points that are far and isolated from the distribution. The accuracy has decreased from its previous value of 98.16% to 78.98%. The 10-fold CV score, in this case, is 76%, which is also a reasonable level of accuracy but significantly less than the maximum accuracy. This implies that the accuracy range can be adjusted to fit the needs of the task. To cover a greater eccentricity range, We have to compensate with accuracy.

Additionally, we have used various ML methods to get the accuracy of the impact parameter, eccentricity, and participant eccentricity predictions at collision energies ranging from 20 GeV to 200 GeV. Compared to higher collision energy, the number of events needed to train an ML model is higher for lower collision energies. This is due to the fact that events with a high multiplicity are produced at higher collision energy. As a result, the averages over events become stable.

In Fig. 5.9, we display the impact parameter prediction error as a function of the impact parameter and the ϵ_{part} distribution. Here we computed the relative error (RE), and it is defined as: $RE = \left|\frac{b_{pred}-b_{org}}{b_{org}}\right|$, where b_{pred} and b_{org} are the predicted and original

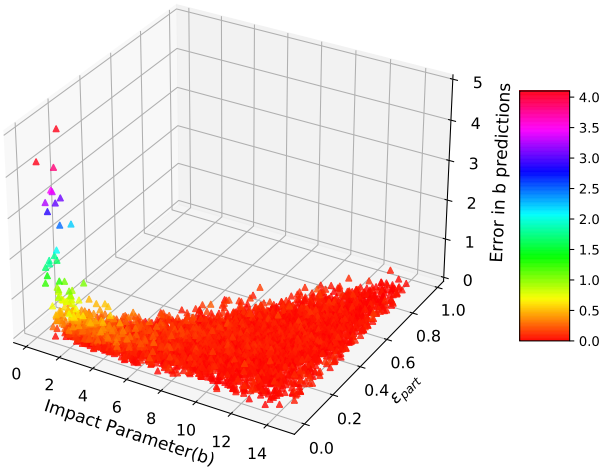

FIGURE 5.9: Error in the prediction of impact parameter as a function of impact parameter and eccentricity distribution. This is for 200 GeV Au-Au collisions and the prediction is obtained using a kNN model

values of b. Except for the region where $b < 2$ fm, we see that the error is small for all eccentricity and impact parameter ranges. The majority of the errors in the distribution are less than 0.5 (shown by the red points) and occasionally less than 1. However, the difference becomes noticeably higher for the lower range of impact parameters ($b < 2$ fm). This is also a result of the data imbalance that has been mentioned earlier. For MC-Glauber model predictions with low-impact parameters, the errors are comparably significant. Large deviations are also obtained when fitting the MC-Glauber model data with the data from the UrQMD and AMPT events, as reported in ref. [44]. Large discrepancies are also found for the fitting of Glauber model data to the ALICE data in ref. [45]. Our observations are consistent with recent findings from machine learning utilizing other models, such as UrQMD, where it was found that the models are capable of efficiently determining the impact parameters in all regions, with the exception of the most central and the very peripheral regions [46]. This is closely represented in Fig. ref. 5.9, which shows that there is a significant amount of error in the most central region.

5.3.2 Results from the different HIC models

To examine the model dependency, we used data from various HIC models, and predictions were obtained for the impact parameter. The AMPT model data were used to train an ML model, and predictions were performed using data from other heavy-ion collision models. The other HIC models employed in this work are the VISH2+1 model [17], which is a hydrodynamic evolution code, and a hybrid model formed of

the VISH2+1 and UrQMD models. The UrQMD model is used for final hadronic rescatterings in the hybrid model [18]. We employ various models because we want the test set and training set to be generated by multiple models that produce the same p_T spectra. This would imply that the ML models won't be able to identify which model generated the test data. The p_T spectra of the AMPT model were employed as features and the impact parameters of the associated AMPT events as targets for training the ML models. We use the minimum bias Au-Au events with collision energies of 200 GeV. At the same collision energy and at various centralities, the p_T spectra of the VISH2+1 and hybrid models are produced, with impact parameters ranging from 0.1 fm to 14 fm. The parameter values of the VISH2+1 model used in this study are identical to those used in ref. [47]. We have used the Glauber model for initial distribution, $\eta/s = 0.16$, and decoupling temperature $T_{dec} = 160$ MeV. The box plot is given for the s95p-PCE equation of state. We set the η/s for the hybrid model to 0.08 and used the s95p-PCE equation of state with $T_{dec} = 165$ MeV. For each of the impact parameter ranges, we obtained 5000 events from each of these models, and we fitted the average p_T spectra with the experimentally observed p_T spectra [48, 49]. The range of p_T considered in order to fit the experimental spectra is 0.15 to 1.4 GeV/c to train ML models. The experimental results and VISH2+1 data are well-matched in this range. By doing this, we are also broadly evaluating how well machine learning models can perform when experimental data are used as test data for predictions. Different HIC models were employed to construct the p_T spectra since we needed event-by-event experimental data at various centralities. In this way, the error distribution of the predictions made by the ML model for a large number of events at different centralities can then be obtained.

All of the ML models used in this analysis, such as kNN, RF, ET, and LR, perform really well when it comes to impact parameter prediction using test data from an undisclosed HIC model. Figures 5.10(a) and 5.10(b) present the error plots of impact parameter predictions by the kNN model for the VISH2+1 and hybrid UrQMD models, respectively. The box portrays the distribution of relative errors. The median error is shown by the middle line inside the box, which is located in the center of the box. The top and bottom lines show the 25th and 75th percentiles of the error distribution. The green point represents the mean error. The errors show a normal distribution in all boxes or across all centralities. This indicates that the ML model made an accurate prediction. The outliers are shown by the end circles, which are fewer in number. In both plots, we observe that errors decrease for events with higher impact parameters. The errors are almost negligible above the impact parameter of 2 fm. The errors remained minimal above $b = 10$ fm, reflecting the prior trend. The three lines in Fig. 5.10(a) indicate the mean prediction errors of impact parameters for different Equations of State (EoS). The

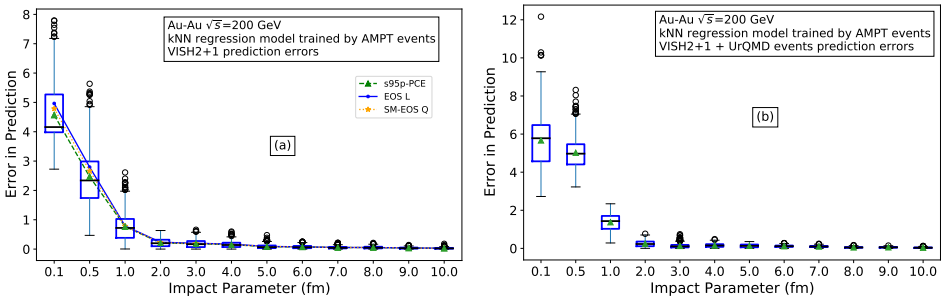

FIGURE 5.10: Error plot of impact parameter predictions by kNN model of different centrality events of a) VISH2+1 and b) UrQMD simulations. The 3 lines in (a) show the mean errors in impact parameter prediction for different EoS

mean errors for the s95p-PCE, EOS L, and SM-EOS Q equations of state are represented by the green (dashed), blue (solid), and yellow (dotted) lines, respectively. The pattern of the error distribution is the same for all EoS. However, in Fig. 5.10(a) and (b), the relative prediction errors for 0.1 and 0.5 fm impact parameter events are more than three and five times, respectively, than the original impact parameters. We have taken the impact parameter range of 0 to 3.31 fm for $0-5\%$ central Au-Au collision events [9]. As was mentioned, the Glauber model is used to determine the centrality in the case of experiments. As a result, it might be challenging to determine a precise impact parameter value, especially for the most central events. While using the AMPT events, we saw the same type of error distribution in Fig. 5.9. We used AMPT events for both the ML model's training and testing, which itself is an unbalanced dataset. Even though the nature of the error distribution is similar in all scenarios, we employed the Glauber initial conditions for the hydro model input. Different p_T spectra can result from the Color Glass Condensate model's initial condition. In that case, the parameters of the hydro model should be changed so that the produced p_T spectra match the experimental p_T spectra in order to test the effectiveness of the ML models.

5.3.3 Results from rebalancing the data set

Due to the imbalance in the impact parameter distribution in the training set, a significant error is seen in the prediction in the lower impact parameter region in Fig. 5.9 and Fig. 5.10. We circumvent this using the unique sample weighing technique described in Section III (B). As previously mentioned in Section III B, we initially employed standard python packages to rebalance the data. The outcomes are displayed in Fig. 5.11 for smoteR (a) and ADASYN(b) method. Despite the fact that the error is less in the region of low-impact parameters compared to the errors found in Fig. 5.9, we still obtain enough errors to produce an inaccurate estimate for the low-impact parameter events.

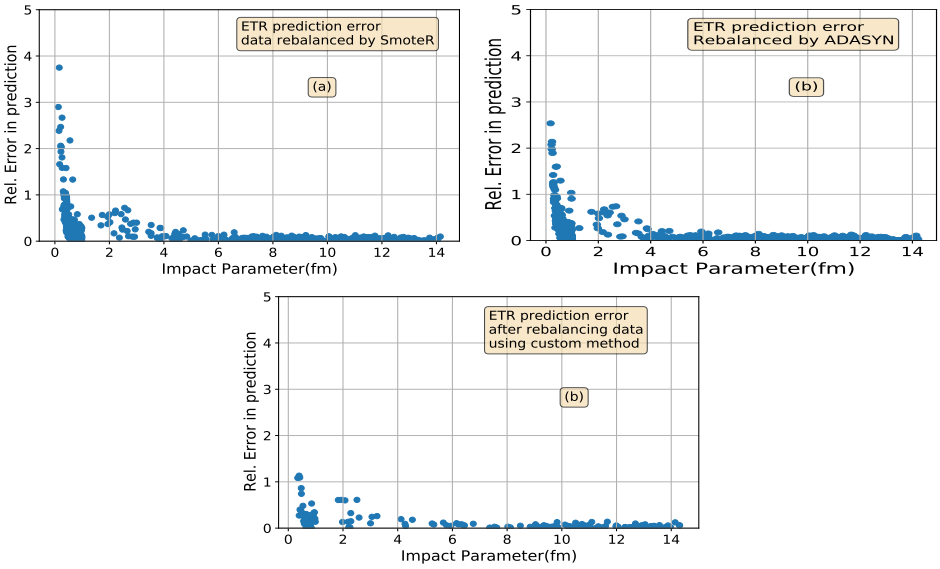

FIGURE 5.11: Error distribution of ET model of impact parameter predictions of Au-Au collisions at $\sqrt{s} = 200$ GeV. The training set is re-balanced using a) SmoteR method, and b) a custom method of giving weights to the input data

In Section III B, we provided a detailed description of our custom rebalancing approach, and the result is shown in Fig. 5.11 (c). As illustrated in Fig. 5.11 (c), we were able to reduce the error to less than 1 using our custom balancing technique. Since the prediction performed in this range will always fall in the most central collision category $(0-5\%)$ for the Au-Au collisions, this much uncertainty in error is acceptable for this range of impact parameters.

It is also compelling to observe how the AMPT-trained models estimate eccentricity when supplied with data from other HIC model simulations. The distribution of eccentricity of 200 GeV AMPT collision events with respect to the impact parameter is shown in Fig. 5.12(a). The color plot shows that the average eccentricity and impact parameters of collision events are linearly related. We can see that with lower impact parameter values, the eccentricity range is smaller. The range of eccentricity increases as we pursue higher impact parameter events. A prior study also shows a similar observation [50]. We present the distribution of eccentricity predictions for two centrality ranges for VISH2+1 events in Fig. 5.12(b). The ML model is trained using minimum bias AMPT events. The orange dots represent event predictions of $40-80\%$ centrality, whereas the blue dots represent event predictions of $0-10\%$ centrality. We obtain an eccentricity distribution in the $0-0.15$ range for the $0-10\%$ centrality range, which is also within the range of the original distribution presented in Fig. 5.12 (a). In the higher impact parameter range, we obtain a wider range of eccentricity values, shown by orange

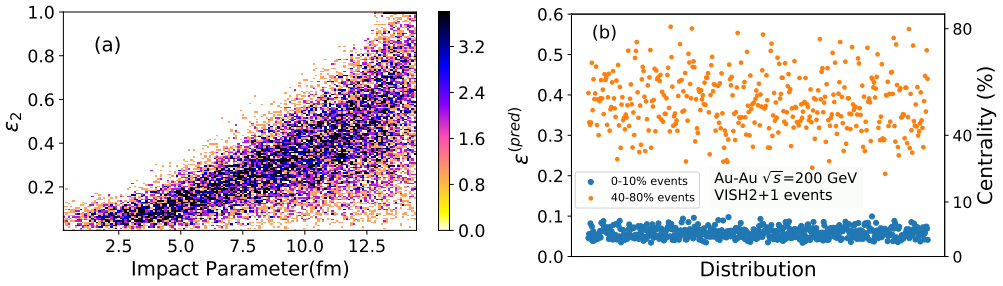

FIGURE 5.12: a) Distribution of eccentricity with impact parameter of min. bias Au-Au collision events at $\sqrt{s} = 200$ GeV, b) Distribution of eccentricity predictions by kNN model of $0-10\%$ and $40-80\%$ centrality events of Au-Au collisions at $\sqrt{s} = 200$ GeV from the VISH2+1 model.

dots. Although this demonstrates how ML model performance is model-independent, only the Glauber initial conditions of the VISH2+1 model are analyzed. We have not included the Color Glass Condensate initial conditions since it is known that they produce a larger anisotropy. It would be interesting to examine how the model would perform in such a scenario.

In Fig. 5.8(a), we have demonstrated an imbalance in the ϵ_{part} distribution. Due to this unbalanced distribution, we can only estimate eccentricity with an accuracy of more than 95% when we take a narrow range into account. The CV accuracy was reduced to 76% for a wider range. If the data are rebalanced in an appropriate manner, excellent accuracy can also be obtained for distributions of eccentricities that span a wider range. We have tested with a rebalancing method similar in nature to that used for impact parameter prediction. We trained the model using the same amount of events for each distribution bin. Fig. 5.13 displays the ϵ_{part} prediction plot using the rebalanced data. If we compare the event points to Fig. 5.8(b), which also has the same range of eccentricity, we see that the event points are substantially nearer to the optimum accuracy line (red line). The cross-validation score here is 91%. Therefore, one can enhance the accuracy of these ML models for the estimation of the impact parameter as well as the eccentricity by applying these data rebalancing approaches.

5.4 Conclusions

In order to estimate various initial stage properties of a heavy-ion collision system, we have trained multiple machine learning models using the AMPT model data. We trained and tested the ML model's performance using the p_T spectrum as it is one of the direct outcomes of heavy-ion collision experiments. We examined how the ML models learned

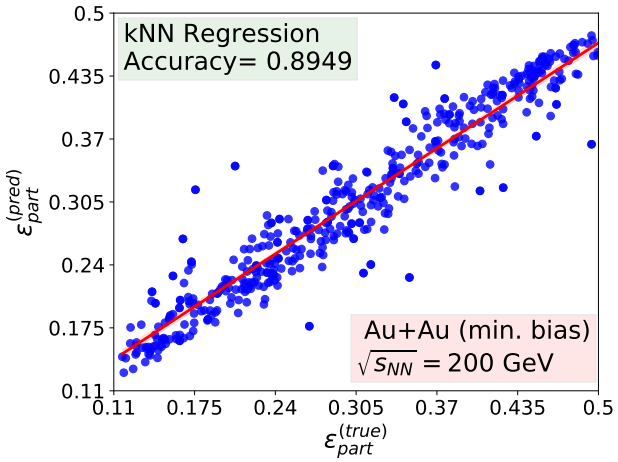

FIGURE 5.13: Participant eccentricity predictions of Au-Au collision events at $\sqrt{s}$ = 200 GeV after rebalancing the data using the custom method

and made adjustments to the hyperparameters to achieve the best prediction accuracy. Four models—kNN, RF, ET, and LR—have been selected from the many tested models to predict the impact parameter. Most models have exhibited higher than 90% accuracy in predicting the impact parameter. Three models, the kNN, ET, and RF performed remarkably well and provided a CV score of more than 90% in the case of the eccentricity and the participant eccentricity prediction. The eccentricity predictions have the highest accuracy in the $0.2 - 0.32$ range of eccentricity. Additionally, a wider range of eccentricity $(0.1 - 0.5)$ has also been considered. Due to the imbalance in the training data distribution, we observe that the selection of the eccentricity range has an impact on the ML model performance.

Additionally, we performed a study of how the model might do in terms of predicting the centrality classes generated by a different simulation model. We have used two other heavy-ion collision models that are distinct from the AMPT model used to train the machine learning models: a viscous hydrodynamic model (VISH2+1) and a hybrid model (Hydro+UrQMD). For the events of the VISH2+1 model and the hybrid model, the impact parameter predictions of the ML models are produced. Although we have shown the results of the kNN model, all the ML models correctly predicted the centrality classes of these events. Despite the fact that we have found larger errors for 0.5 fm events in both instances, the errors for other b values are comparatively small. This can be a result of the unbalanced nature of the data set. When the data set is normalized, it is noticed that the distribution's peak is not exactly at the center. This suggests that the eccentricity and impact parameter distributions across events are not isotropic.

We have employed a variety of sampling techniques to reduce these errors. After using multiple common methods that facilitate rebalancing the data, we eventually find that the accuracy is increased in the lower impact parameter region if we assign various weights to the data for different ranges of impact parameters. The result is shown for the ET model, where we have used four times higher weights for the rarer events. As a result, accuracy in the lower impact parameter range has improved. For a broader range of eccentricity distribution, our rebalancing method produced a CV accuracy of more than 90%. This resulted in an overall improvement from an accuracy of 75% before to an accuracy of 90% afterward. So, according to our study, a rebalanced data set will be beneficial in making precise predictions for central collisions.

Bibliography

[1] L. X. Han, G. L. Ma, Y. G. Ma, X. Z. Cai, J. H. Chen, S. Zhang , and C. Zhong, Phys. Rev. C **84**, 064907 (2011).

[2] Prorok, D., Eur. Phys. J. A **26**, 277–284 (2005).

[3] K. Adcox et al. (PHENIX Collaboration) Phys. Rev. Lett. **86**, 3500 (2001).

[4] K. Aamodt et al. (ALICE Collaboration) Phys. Rev. Lett. **106**, 032301 (2011).

[5] J. Adam et al. (ALICE Collaboration) Phys. Rev. Lett. **116**, 222302 (2016).

[6] S.Acharya et al. (ALICE Collaboration), Phys. Lett. B **790**, 10, 35-48 (2019); ALICE Collaboration, Phys. Lett. B **788**, 166-179, (2019); R. Rath, S. Tripathy, R. Sahoo, S. De, and Md Younus, Phys. Rev. C **99**, 064903 (2019).

[7] M. L. Miller, K. Reygers, S. J. Sanders, P. Steinberg, Peter, Ann. Rev. Nucl. Part. Sci. **57**, 205-243 (2007).

[8] C. David, M. Freslier and J. Aichelin, Phys. Rev. C **51**, 1453 (1995).

[9] Constantin Loizides, Jason Kamin, and David d'Enterria, Phys. Rev. C **97**, 054910 (2018).

[10] Fupeng Li et. al., Phys. Rev. C **104**, 034608 (2021).

[11] J. De Sanctis, M. Masotti, M. Bruno et al.,J. Phys. G **36**, 015101 (2009).

[12] M. Omana Kuttan, J. Steinheimer, K. Zhou, A. Redelbach, and H. Stoecker, Phys. Lett. B **811**, 135872 (2020).

[13] Yige Huang, Long-Gang Pang, Xiaofeng Luo, Xin-Nian Wang, Phys. Lett. B **827**, 137001 (2022).

[14] S. A. Bass, A. Bischoff, C. Hartnack, J. A. Maruhn, J. Reinhardt, H. Stocker and W. Greiner, Journal of Physics G, Nuclear and Particle Physics **20**, L21 (1994).

[15] Tetsufumi Hirano and Yasushi Nara, Phys. Rev. C **79**, 064904(2009)

[16] Niseem Magdy 2022 J. Phys. G: Nucl. Part. Phys. **49**, 015105 (2021).

[17] H. Song and U. Heinz, Phys. Rev. C **77**, 064901 (2008).

[18] C. Shen et al., Computer Physics Communications **199**, (2016), 61-85.

[19] Sarker, I.H. SN COMPUT. SCI. **2**, 160 (2021)

[20] K. Taunk, S. De, S. Verma and A. Swetapadma, 2019 International Conference on Intelligent Computing and Control Systems (ICCS), **2019**, pp. 1255-1260

[21] Leo Breiman, machine learning **45**(1), 5-32, 2001.

[22] Geurts, P., Ernst, D. ,Wehenkel, L. , Machine Learning **63**, 3–42 (2006).

[23] M. Ojala and G. C. Garriga., Journal of Machine Learning Research **11**, 1833-1863 (2010).

[24] PATRO, S GOPAL & Sahu, Dr-Kishore Kumar, IARJSET. Vol. **2**, Issue 3, (2015).

[25] Scikit-learn: Machine Learning in Python, Pedregosa et al., JMLR **12**, pp. 2825-2830, 2011.

[26] T. Doan and J. Kalita, 2015 IEEE International Conference on Data Mining Workshop (ICDMW), **2015**, pp. 1498-1505 (2015)

[27] Jerome H. Friedman, Computational Statistics and Data Analysis **38**, 367-378(1999); B. P. Roe, H. J. Yang, J. Zhu, Y. Liu, I. Stancu, and G.McGregor, Nucl. Instrum. Methods Phys. Res., Sect. A **543**, 577 (2005).

[28] Ke, G., Meng, Q., Finley, T., Wang, T., Chen, W., Ma, W., Ye, Q., & Liu, T., LightGBM: A Highly Efficient Gradient Boosting Decision Tree. NIPS 2017.

[29] Peter L. Bartlett, Mikhail Traskin, Journal of Machine Learning Research **8** 2347-2368(2007); Yoav Freund, Robert E. Schapire, Journal of Japanese Society for Artificial Intelligence, **14**(5), 771-780, (1999).

[30] Hoerl, Arthur E.; Kennard, Robert W.; Hoerl, Roger W. (1985). Journal of the Royal Statistical Society, Series C. **34** (2), 114–120; Wessel N. van Wieringen, arXiv:1509.09169.

[31] B. Efron, T. Hastie, I. Johnstone, R. Tibshirani, Annals of Statistics 2004, Vol. **32**, No. 2, 407-451 (2004).

[32] Peter J. Huber, Ann. Statist. **1(5)**: 799-821 (1973).

[33] Fornalski, Krzysztof W., International Journal of Society Systems Science. **7 (4)**: 314–333 (2015).

[34] T. Tony Cai and Lie Wang, IEEE TRANSACTIONS ON INFORMATION THEORY, VOL. **57**, NO. 7, (2011).

[35] Loh, W.-Y. (2011), WIREs Data Mining and Knowledge Discovery Volume **1**, Issue 1 p. 14-23.

[36] Koby Crammer, Ofer Dekel, Joseph Keshet, Shai Shalev-Shwartz, Yoram Singer, Journal of Machine Learning Research **7** 551–585 (2006).

[37] Journal of the Royal Statisticla Society B **58**, No. 1, 267-288 (1996).

[38] Hui Zou and Trevor Hastie, J. R. Statist. Soc. B **67**, Part 2, pp. 301–320 (2005).

[39] Ian T. Jolliffe, Jorge Cadima, Phil. Trans. R. Soc. A **374**: 20150202.

[40] K. Grebieszkow, Phys. Rev. C **76**, 064908 (2007).

[41] S. A. Bass, A. Bischoff, J. A. Maruhn, H. Stocker, and W. Greiner, Phys. Rev. C **53**, 2358 (1996).

[42] Feng Hu and Hang Li, Mathematical Problems in Engineering **2013**(1), 694809 (2013).

[43] Haibo He, Yang Bai, E. A. Garcia and Shutao Li, 2008 IEEE International Joint Conference on Neural Networks, **2008**, pp. 1322-1328.

[44] Parfenov, P.; Idrisov, D.; Luong, V.B.; Taranenko, A.; Particles **4**, 275–287 (2021).

[45] B. Abelev et al. (ALICE Collaboration), Phys. Rev. C **88**, 044909 (2013).

[46] C.Y. Tsang et al. Phys. Rev. C **104**, 034608 (2021)

[47] C. Shen, U. Heinz, P. Huovinen, and H. Song, Phys. Rev. C **82**, 054904 (2010).

[48] I. Arsene et al. (BRAHMS Collaboration), Phys. Rev. C **72**, 014908 (2005).

[49] B. I. Abelev et al. (STAR Collaboration), Phys. Rev. Lett. **97**, 152301 (2006).

[50] Anya Wolterman, Macalester Journal of Physics and Astronomy Volume **8**, Article 17 (2020).

Chapter 6

Summary and Conclusions

We studied different stages of heavy ion collision systems using various simulation models and machine learning techniques. One of the primary motivations for conducting these experiments is to study the deconfined phase of matter, i.e., the quark-gluon plasma phase. Although the lifetime of the QGP is very short, we find several properties of the QGP system through various final state spectrum analyses. We also find their effects on the final outcomes of these experiments. The initial state distribution and fluctuations majorly impact the final state hadron spectra. In the past, multiple research has shown how the initial geometry parameters such as eccentricity ϵ_2, triangularity ϵ_3, etc., affect the collective flow components of finally produced particles. It is also observed that almost all the final outcomes of heavy ion collision experiments depend on the centrality of the collision events, which is also an initial geometry parameter. We know that the collision region's initial state energy distribution is not uniform. Because of this, and the spatial density distribution of the initial partonic system a large angular momentum develops. This causes vorticity-like phenomena in the plasma to arise, and we see its effect in terms of particle polarization. Along with this, the fields created by the spectator nucleons are responsible for generating a huge magnetic field which causes transport currents to develop in the plasma. That is why it becomes crucial to know the initial state characteristics of heavy ion collisions. In this thesis, we have studied several distribution and fluctuation-related phenomena and found their connections with the final state hadron production. This includes the study of vorticity at different stages of the system evolution in heavy ion collision experiments. This also includes the energy deposition at different length scales by generating turbulence spectra, and entropic index at different stages calculated from the temperature fluctuations. As the initial state parameters are difficult to obtain in the experimental setup, we used several machine learning techniques to estimate these parameters. We have also focused on carrying out a model-independent

study in this regard, as the training of the ML models is very sensitive to the input data.

In the second chapter, we have presented our study on vorticity distribution in the initial partonic stage and the final hadronic state. We use different definitions of vorticity to see if we can distinguish between the vorticity distributions obtained from different definitions. Different definitions help us obtain different types of vorticity, which are used to study various characteristics. For example, thermal vorticity is particularly of interest as it is used to parameterize the polarization effect found for several finally produced hadrons, which is one of the observable in heavy ion collision experiments. Although relativistic and thermal vorticity distributions have more significant fluctuations than the classical vorticity distribution, there is an overall global similarity. We found distinct vortex formation at larger collision energies, and as we go lower in collision energy, the vortices tend to diffuse more. This is observed throughout the collision energy range we have considered, which is 20 GeV to 200 GeV. We know that vorticity distribution can be affected by the viscosity of different layers in the medium. We obtained the specific shear viscosity η/s from the HRG model at different collision energies. We find that at lower collision energies, η/s is higher, and it starts to go down with increasing collision energy, and after $\sqrt{s_{NN}} = 80$ GeV, η/s becomes constant. We observed a similar pattern for various particles. We suspect that the larger angular momentum at high collision energy helps generate these distinct vortices. At the lower collision energies, the viscosity becomes more effective, and the energy gets diffused more and more at lower $\sqrt{s_{NN}}$, which causes the formation of elongated vortices. The scenario is different when we study the average weighted vorticity. We see the average vorticity first increases and then goes down with collision energy. The maximum vorticity we observed was at around 60 GeV in all the cases. This behavior is also observed in later studies where the maximum vorticity is observed at about 27 GeV collision energy. This behavior is entirely different from the angular momentum change with collision energy. One of the possible reasons behind this is that angular momentum in a system can be generated from various sources. The moment of inertia of the system is one of them that we have not considered in our study. We only focused on the angular momentum responsible for vorticity production.

The system created in the earlier stages of heavy ion collision experiments has an exceedingly high Reynolds number. Due to this, several aspects of viscous flow, including whether or not turbulence develops, are still unknown from the earlier study. As it is evident that there are fluctuations in the initial plasma, it can constitute turbulence flow. Hence, turbulence spectra can be obtained in this system. The turbulence spectra provide insights into the energy dissipation in the system at various length scales. To

study the spatial anisotropy in energy dissipation, we obtain the turbulence spectra for velocity fields at different planes of the system. We first found the possible length scales of the heavy ion collision system, specifically for Au-Au collisions at RHIC energies. Then we extract the turbulence velocity from the particle flow velocity and calculate the velocity correlation tensor. Using the velocity correlation tensor, we calculated the energy spectra. As we work with relativistic velocities, we use a boost matrix to account for the Lorentz boost effect. This is only done for longitudinal plane spectra as the boost is only in the z-axis. The isotropic turbulence spectra should resemble the Kolmogorov spectra, which have a power-law characteristic in the inertial sub-range. For Kolmogorov spectra, the energy in turbulent flows carried by eddies of diameter D is proportional to $D^{5/3}$. Hence, the slope of the Kolmogorov type of spectra is $-5/3$, which is represented by ν. So any turbulence spectra fitted with a power-law distribution having slope $-5/3$ will indicate the isotropic energy dissipation. We have found that the ν value for longitudinal spectra is $-5/3$, nearer to the Kolmogorov type of spectra. But the ν value for the transverse plane spectrum is around $-4/3$. We found that the slope stays closer to $-5/3$ for all the collision energies below 200 GeV and all the centralities for longitudinal spectra. But comparatively, the change in ν value is larger with collision centrality for transverse plane spectra. This indicates anisotropic energy dissipation. The anisotropic flows are produced in the transverse plane and suppressed due to the viscous nature of the fluid. This is also a possible reason for anisotropic energy dissipation in the transverse plane. Even though the turbulent system might be overall isotropic, if we divide it into different planes, we find that the power law coefficients will differ on each plane.

We also analyze the temperature spectrum of the turbulent system in the early stages and pre-equilibrium stages of QGP evolution. The spectrum is obtained by calculating the temperature correlation tensor. By studying the temperature spectrum, one can also understand the thermal length scales of the system. We expect the temperature spectra to be Gaussian in nature for an isotropic medium. Though the temperature spectrum first appears to be Gaussian, we have observed that a q-Gaussian distribution fits it better over time. This also indicates the system anisotropy. All these suggest that even though the turbulence observed in relativistic collisions is typically isotropic and uniform, it would be more effective to slice the system into planes and study the turbulence characteristics at each plane separately.

As discussed in Chapter III, there are significant temperature fluctuations in the system. We calculate the temperature of the initial partonic system assuming local thermalization. We showed the temperature distribution with respect to the time of plasma formation and collision energy for randomly selected events. With time, the fluctuations get diminished. With collision energy, there are no such changes, but the amplitudes

become higher for higher collision energies. To study the behavior of temperature fluctuations, we parameterize the temperature fluctuations using the Tsallis entropic index. This Tsallis distribution is a generalization of Boltzmann-Gibbs statistical distribution with the entropic index characterizing the degree of non-equilibrium. One can obtain the standard distribution from the Tsallis distribution for the equilibrium system, and in such case, the entropic index q tends to 1. In experiments, these q values are obtained by fitting the transverse momentum spectrum of finally produced hadrons with this Tsallis distribution. We obtained the entropic index for the partonic state using temperature fluctuations. When a system has temperature fluctuations, then the generalized distribution function of the system with an entropic index can be obtained by integrating all the fluctuating states provided that the fluctuations are chi-square distributed. We observe that the distribution of temperature fluctuations can be fitted with a Chi-square distribution. q serves as an open parameter in the distribution, and it is found out for appropriate fitting conditions. The q value obtained from the experimental p_T spectra are observed to be dependent on various system parameters. We are curious whether the q values obtained from temperature fluctuations follow a similar behavior with changing system parameters.

The change in q values is found to be linear with respect to the effective temperature, which is also true for the experimentally obtained q values. In this case, the only difference between the q value obtained from the temperature fluctuations and the final hadron spectra is the slope of the fitted straight line. In experiments also, it is observed that the slope is different for different collision systems. We also found the dependence of the q value with changing system parameters like pseudorapidity, collision energy, and formation time. We find that the q value increases for a larger pseudorapidity range, plateauing for higher collision energies. In this case, larger rapidity corresponds to a larger system volume. The behavior is similar to the experimentally obtained q values. With respect to collision energy, the q value increases; however, there is a centrality dependence. Below 100 GeV, the q values are lower for peripheral collision compared to central collision. But above 100 GeV, the trend is reversed. This behavior also matches with the experimentally obtained q-value with respect to the collision energy.

We also found that q increases with plasma formation time, peaks around 3 fm/c, and then decreases with increasing proper time. The increase and subsequent decrease of q values may be attributed to the increase and decrease in the energy density of the system. The temperature fluctuations also show similar behavior with increasing formation time. So from our study, it is evident that the q values obtained from temperature fluctuations behave similarly compared to the q values obtained by fitting the hadron spectra. Hence one can determine how far the system is from the equilibrium state in

terms of the entropic index for the partonic stage by studying the temperature fluctuations.

In chapter V, we show how machine learning models can be a more convenient way to estimate the initial geometry parameters of heavy ion collision experiments. We know that probing anything in the initial state is difficult as the lifetime of the QGP system is very small. Also, it is very difficult to calculate the initial state parameters from the final particle spectra. We use multiple standard ML techniques to predict some initial state geometry parameters such as impact parameter, eccentricity, triangularity, and participant eccentricity. We use charged particle transverse momentum spectra of finally produced hadrons as features to train the ML models. At the same time, the impact parameter and other initial state parameters are used as target variables for the training of the ML models. We found that almost all the models perform reasonably well in impact parameter prediction, but only three models give an accuracy of more than 90% for other geometry parameter predictions. The three ML models are K nearest neighbors, extra trees regression, and random forest regression. We also did a detailed hyperparameter scan through the randomized grid-based search method to maximize the performance of our data. Also, to prepare the training set, we applied multiple preprocessing techniques, such as principal component analysis, and standardized the data set. All these have been done to find a combination of optimized ML model and tuned training set to improve the performance of these ML models.

Although the overall accuracy was adequate, if you see the error distribution for the impact parameter predictions, we find that the errors are very high for most central collisions in the low-impact parameter region. This is because the training data is not balanced; the event distribution of the impact parameter is skewed, with fewer events for the low-impact parameter values. Also, we observed that the accuracy decreases drastically for eccentricity and participant eccentricity prediction when considering the whole range of eccentricity. This is also because the event distribution of eccentricity is not a uniform distribution. To overcome this situation, we use standard sampling techniques used by the ML community, such as SmoteR and ADASYN, to make a balanced dataset. We also used a custom sampling technique where we gave more weightage to the region where the training data has less number of sample points. We found that our custom sampling method performs much better than the standard sampling techniques. This is true for both impact parameter and eccentricity prediction.

We know that the training of the ML models is very sensitive to the training data. We also studied the performance of ML models in the impact parameter and eccentricity prediction in a model-independent manner. To do that, we have trained the ML models

using the transverse momentum spectra generated by the AMPT model, which is a transport model. We generated the test data from two other heavy ion collision models, e.g., a hydro model and a hybrid model. We found that the ML models could perform adequately when the test data came from different models. This is only true when the data matches well with the experimental data. We have used different conditions, such as multiple equations of states and different transport coefficients in the hydro and hybrid models, to check the error distribution of ML model predictions. We found that the errors are negligible for higher impact parameter values. We get higher errors for most central collisions. This is exactly similar to the error distribution when the training and testing are performed using the data of the AMPT model.

Finally, our study shows that only transverse momentum spectra are enough to train ML models so that they can predict the initial state geometry parameters efficiently. Also, the performance of the ML model can be improved by some preprocessing of the input data using sampling techniques.

To summarize, our study is important in the current context of heavy ion collision experiments. The polarization found in certain finally produced hadrons has already hinted at global vorticity in the system. It is also essential to know the local vorticity nature in an out-of-equilibrium system, especially when working with a partonic system. Our study has shown local vorticity formation in different conditions. It would also be interesting to see the distribution of local velocity vectors, which would directly show us the rotational characteristics of the system. In our study, we have discussed how the viscous effects influence the vorticity distribution. It would also be interesting to study how vorticity can affect the transport coefficients of the HIC system. This can also help us to determine the transition temperatures more accurately. Fluctuations and correlations play significant roles in determining the critical point in the QCD phase transition. We have studied velocity and temperature fluctuations in terms of power spectrum analysis and Tsallis statistics. It would be interesting to explore the power spectrum and the Tsallis entropic index for lower collision energies and small system collisions. This could lead us closer to the critical point if we found behavior changes in these parameters. In previous chapters, we have discussed how ML techniques are being used by the particle physics community in various searches. In our study, we have shown the uses of data sampling techniques to rebalance a dataset. This has lowered the errors found in the low-centrality predictions. The type of data that we have used in our study for training and testing the ML models is one of the primary observable in HIC experiments. Thus, this will be useful in the future while working with a similar type of dataset.

List of Publications

Thesis Publications

1. **"Flow and vorticity with varying chemical potential in relativistic heavy ion collisions"**, **Abhisek Saha**, and Soma Sanyal, Int. J. Mod. Phys. E **29**, 01, 2050001 (2020), [arXiv:1902.08368].

2. **"Temperature fluctuations and Tsallis statistics in relativistic heavy ion collisions"**, **Abhisek Saha**, and Soma Sanyal, Mod. Phys. Lett. A **36**, 22, 2150152 (2021), [arXiv:2004.03118].

3. **"Anisotropic turbulence in relativistic plasmas"**, **Abhisek Saha**, and Soma Sanyal, Eur. Phys. J. Plus **137**, 1074 (2022), [arXiv:2108.01847].

4. **"Machine Learning model driven prediction of the initial geometry in Heavy-Ion Collision experiments"**, **Abhisek Saha**, Debasis Dan, and Soma Sanyal, Phys. Rev. C **106**, 014901 (2022), [arXiv:2203.15433].

Other Publications

1. **"Diffusion of massive particles around an Abelian-Higgs string"**, **Abhisek Saha**, and Soma Sanyal, J. Cosmol. Astropart. Phys **03**, 022 (2018), [arXiv:1710.05556].

2. **"Decay of baryon inhomogeneities in an expanding universe"**, Pratik K. Das, Sovan Sau, **Abhisek Saha**, and Soma Sanyal, Eur. Phys. J. C **81**, 816 (2021), [arXiv:2101.01980].

Conference Proceedings

1. **"Shear viscosity and vorticity patterns in relativistic heavy ion collisions"**, **Abhisek Saha** and Soma Sanyal, Springer Proc. Phys. **248**, 48 (2019).

2. **"Vorticity with varying collision energy in relativistic heavy ion collisions"**, **Abhisek Saha** and Soma Sanyal, Proceedings of DAE Nuclear Physics **2019**, 728 (2019).

3. **"Temperature Fluctuations and Tsallis Statistics in Relativistic Heavy Ion Collisions"**, **Abhisek Saha** and Soma Sanyal, Springer Proc. Phys. 277, 299-303 (2022).
   (Proceedings of the XXIV DAE-BRNS High Energy Physics Symposium,)

4. **"Deviations from isotropic turbulence of heavy-ion collision plasma"**, **Abhisek Saha** and Soma Sanyal, Proceedings of Science **414**, 1072 (2022).

Exploring Flow Characteristics and Geometry of Heavy ion Collisions using Simulation Models and Machine Learning

by Abhisek Saha

Submission date: 09-Mar-2023 03:34PM (UTC+0530)
Submission ID: 2032892022
File name: Abhisek_Saha.pdf (19.8M)
Word count: 38420
Character count: 191936

Exploring Flow Characteristics and Geometry of Heavy ion Collisions using Simulation Models and Machine Learning

ORIGINALITY REPORT

32%	20%	30%	1%
SIMILARITY INDEX	INTERNET SOURCES	PUBLICATIONS	STUDENT PAPERS

PRIMARY SOURCES

1	arxiv.org Internet Source Preprint version of this work.	10%
2	Abhisek Saha, Soma Sanyal. "Flow and vorticity with varying chemical potential in relativistic heavy ion collisions", International Journal of Modern Physics E, 2020 Publication	5%
3	Abhisek Saha, Soma Sanyal. "Anisotropic turbulence in relativistic plasmas", The European Physical Journal Plus, 2022 Publication	5%
4	Abhisek Saha, Soma Sanyal. "Temperature fluctuations and Tsallis statistics in relativistic heavy ion collisions", Modern Physics Letters A, 2021 Publication	3%
5	Abhisek Saha, Debasis Dan, Soma Sanyal. "Machine-learning model-driven prediction of the initial geometry in heavy-ion collision experiments", Physical Review C, 2022	2%

Dr. SOMA SANYAL
Associate Professor
School of Physics
University of Hyderabad
Hyderabad-500046, India.

	Publication	
6	ebin.pub Internet Source	1 %
7	agenda.infn.it Internet Source	1 %
8	export.arxiv.org Internet Source	<1 %
9	indico.cern.ch Internet Source	<1 %
10	"Proceedings of the XXIV DAE-BRNS High Energy Physics Symposium, Jatni, India", Springer Science and Business Media LLC, 2022 Publication	<1 %
11	"Strongly Interacting Matter under Rotation", Springer Science and Business Media LLC, 2021 Publication	<1 %
12	iopscience.iop.org Internet Source	<1 %
13	Rajendra Nath Patra, Bedangadas Mohanty, Tapan K. Nayak. "Centrality, transverse momentum and collision energy dependence of the Tsallis parameters in relativistic heavy-ion collisions", The European Physical Journal Plus, 2021 Publication	<1 %

Dr. SOMA SANYAL
Associate Professor
School of Physics
University of Hyderabad
Hyderabad-500046, India.

14	Submitted to Indian Institute of Science, Bangalore Student Paper	<1 %
15	Liyue Wang, Cong Wang, Shuyue Wang, Gang Sun, Bo You. "Design and analysis of micro-nano scale nested-grooved surface structure for drag reduction based on 'Vortex-Driven Design'", European Journal of Mechanics - B/Fluids, 2020 Publication	<1 %
16	Larry McLerran. "RHIC physics: 3 lectures", Surveys in High Energy Physics, 2003 Publication	<1 %
17	Lecture Notes in Physics, 2011. Publication	<1 %
18	thescholarship.ecu.edu Internet Source	<1 %
19	Francois Gelis. "Some Aspects of the Theory of Heavy Ion Collisions", Reports on Progress in Physics, 2021 Publication	<1 %
20	www.science.gov Internet Source	<1 %
21	drupal.star.bnl.gov Internet Source	<1 %
	www.tib.eu	

22	Internet Source	<1%
23	tel.archives-ouvertes.fr Internet Source	<1%
24	www.niser.ac.in Internet Source	<1%
25	Lecture Notes in Physics, 2013. Publication	<1%
26	123dok.net Internet Source	<1%
27	miocene.anu.edu.au Internet Source	<1%
28	Takahiro Sasaki, Yuji Sakai, Hiroaki Kouno, Masanobu Yahiro. "QCD phase diagram at finite baryon and isospin chemical potentials", Physical Review D, 2010 Publication	<1%
29	www.star.bnl.gov Internet Source	<1%
30	Marcus Bleicher, Elena Bratkovskaya. "Modelling relativistic heavy-ion collisions with dynamical transport approaches", Progress in Particle and Nuclear Physics, 2022 Publication	<1%

31	Structure and Dynamics of Elementary Matter, 2004. Publication	<1 %
32	qm09.phys.utk.edu Internet Source	<1 %
33	epub.uni-regensburg.de Internet Source	<1 %
34	Lecture Notes in Physics, 2010. Publication	<1 %
35	Simon Hands. "The phase diagram of QCD", Contemporary Physics, 2001 Publication	<1 %
36	Submitted to The University of Manchester Student Paper	<1 %
37	Submitted to Higher Education Commission Pakistan Student Paper	<1 %
38	www.avcr.cz Internet Source	<1 %
39	Debe, M.K.. "Optical probes of organic thin films: Photons-in and photons-out", Progress in Surface Science, 1987 Publication	<1 %
40	J. Beringer, J. -F. Arguin, R. M. Barnett, K. Copic et al. "Review of Particle Physics", Physical	<1 %

Review D, 2012
Publication

41	Wei-Tian Deng, Xu-Guang Huang. "Vorticity in heavy-ion collisions", Physical Review C, 2016 Publication	<1 %
42	archivia.unict.it Internet Source	<1 %
43	hdl.handle.net Internet Source	<1 %
44	nbn-resolving.de Internet Source	<1 %
45	the PHENIX Collaboration. "PHENIX Measurement of Particle Yields at High p"T with Respect to Reaction Plane in Au+Au Collisions at s"N"N=200 GeV", Nuclear Physics, Section A, 20060807 Publication	<1 %
46	www.physics.sunysb.edu Internet Source	<1 %
47	www.site.uottawa.ca Internet Source	<1 %
48	Leonardo Barreto de Oliveira Campos. "Study of Jet Modification in Relativistic Heavy-Ion Collisions", Universidade de Sao Paulo, Agencia USP de Gestao da Informacao Academica (AGUIA), 2021 Publication	<1 %

49	studylib.net Internet Source	<1%
50	Bass, S.A.. "Last call for RHIC predictions", Nuclear Physics, Section A, 19991227 Publication	<1%
51	STAR Collaboration. "Experimental and theoretical challenges in the search for the quark-gluon plasma: The STAR Collaboration's critical assessment of the evidence from RHIC collisions", Nuclear Physics, Section A, 20050808 Publication	<1%
52	Submitted to Stockholms universitet Student Paper	<1%
53	www.sp.u-tokai.ac.jp Internet Source	<1%

Exclude quotes	On	Exclude matches	< 14 words
Exclude bibliography	On		

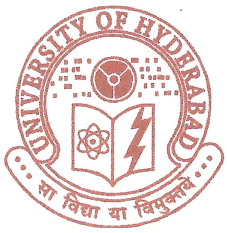

This is to certify that the thesis entitled "**Exploring Flow Characteristics and Geometry of Heavy ion Collisions using Simulation Models and Machine Learning**" has been screened by the Turnitin Software at the Indira Gandhi Memorial Library (IGML), University of Hyderabad. The software shows 32% similarity index out of which 15% came from the candidates published version of research articles related to this thesis. Part of the rest 10% came from the pre-print archive (arxiv.org) for physics where all the pre-print versions of his work has been uploaded and 2% came from the various Proceedings that were published as the candidate has given talks at various conferences. After excluding all these work which are by the candidate himself, the remaining effective similarity index is only 5% which is below the 10% stipulated by the University guidelines. These similarities come from sources or articles in which the software detected mostly generic terms, standard notations, standard equations, standard symbols and common terminologies frequently used in this field. Therefore this thesis is free from plagiarism.

Dr. Soma Sanyal 10/3/2023.
School of Physics
University of Hyderabad

Thesis Supervisor

Dr. SOMA SANYAL
Associate Professor
School of Physics
University of Hyderabad
Hyderabad-500046, India.